NANYANG TECHNOLOGICAL UNIVERSITY
SINGAPORE

HIGH-VOLTAGE IR-UWB PULSE GENERATOR MMIC DESIGN AND BEAMFORMING FOR INDOOR-RANGING AND RADAR APPLICATIONS

HUSSAIN ANSARI MD ARIF

SCHOOL OF ELECTRICAL AND ELECTRONIC ENGINEERING

2019

HIGH-VOLTAGE IR-UWB PULSE GENERATOR MMIC DESIGN AND BEAMFORMING FOR INDOOR-RANGING AND RADAR APPLICATIONS

HUSSAIN ANSARI MD ARIF

SCHOOL OF ELECTRICAL & ELECTRONIC ENGINEERING

A thesis submitted to the Nanyang Technological University
in partial fulfilment of the requirement for the degree of
Doctor of Philosophy

2019

Statement of Originality

I hereby certify that the work embodied in this thesis is the result of original research, is free of plagiarised materials, and has not been submitted for a higher degree to any other University or Institution.

15 December 2019

. . . . . .

Date

. . . . . .

Md Arif Hussain Ansari

Supervisor Declaration Statement

I have reviewed the content and presentation style of this thesis and declare it is free of plagiarism and of sufficient grammatical clarity to be examined. To the best of my knowledge, the research and writing are those of the candidate except as acknowledged in the Author Attribution Statement. I confirm that the investigations were conducted in accord with the ethics policies and integrity standards of Nanyang Technological University and that the research data are presented honestly and without prejudice.

16 December 2019

. . . . . .

Date

. . . . . .

Associate Professor Law Choi Look

Authorship Attribution Statement

This thesis contains material from eight papers published in the following peer-reviewed journals/conferences in which I am listed as the first author.

The content of Chapter-3 is published in the following peer-reviewed journals or presented in conferences.

1. M. Arif Hussain Ansari, and Choi Look Law. "Circuit Analysis and Optimization of High-Voltage High-Efficiency IR-UWB Pulse generator for Ranging and Radar Application" *IET Circuit Devices and System,* Vol. 14, No. 4, pp. 562 – 568, July 2020.
2. M. Arif Hussain Ansari, Manmohan Sharma, and Choi Look Law, "High Peak Power UWB-RFID Transmitter Tag for Long Range Applications." *Progress In Electromagnetic Research Symposium (PIERs) Singapore,* 19-22 Nov 2017. [*This paper won best conference paper award*]
3. M. Arif Hussain Ansari, Manmohan Sharma, and Choi Look Law. "High Peak Power IR-UWB Pulse Generator for Long Range Indoor Localization." *Progress In Electromagnetic Research Symposium (PIERs) Singapore,* 19-22 Nov 2017.
4. M. Arif Hussain Ansari, and Choi Look Law. "High Voltage High-efficiency UWB Pulse Generator for Precision Localization Wireless Sensor Network." *IEEE International Symposium on Integrated Circuits (ISIC) Singapore,* 12-14 Dec 2016.

The contributions of the co-authors are as follows:

- Assoc/Prof Choi Look Law provided the initial project direction and edited the manuscript drafts.
- I prepared the manuscript drafts. The manuscript was revised by Assoc/Prof Choi Look Law.
- I co-designed the study with Assoc/Prof Choi Look Law and performed all the laboratory work at the School of Electrical and Electronic Engineering. I analyzed the results,

simulated data, and derived related mathematical models under the supervision of Assoc/Prof Law Choi Look.

- Dr. Manmohan Sharma helped in the initial measurement setup. He also helped to edit the initial draft of the manuscript published as papers – 1 and 2 indicated above.

The content of Chapter-4 is published in the following peer-reviewed journals or presented in conferences.

1. M. Arif Hussain Ansari, and Choi Look Law. "Beam-Pattern Analysis of Multi-Beam High Peak Power IR-UWB Transmitter Tag for Indoor Positioning and Tracking System" *Progress In Electromagnetics Research B*, Vol. 86, 1-18, 2020.
2. M. Arif Hussain Ansari, and Choi Look Law. "Steerable Beamforming UWB-IR Transmitter Array for Directional Indoor Positioning Applications." *Progress In Electromagnetic Research Symposium (PIERs), Toyama, Japan,* 1-4 August 2018.
3. M. Arif Hussain Ansari, Choi Look Law, "Beamforming UWB-IR transmitter for NLOS Indoor Positioning and Tracking Application", *IEEE MTT-S International Wireless Symposium, Chengdu, China*. 6-10 May 2018. [*This paper won best conference paper award*]

The contributions of the co-authors are as follows:

- Assoc/Prof Choi Look Law provided the initial project direction and edited the manuscript drafts.
- I prepared the manuscript drafts. The manuscript was revised by Assoc/Prof Choi Look Law.
- I co-designed the study with Assoc/Prof Choi Look Law and performed all the laboratory work at the School of Electrical and Electronic Engineering. I analyzed the results, simulated data, and derived related mathematical models under the supervision of Assoc/Prof Law Choi Look.

The content of Chapter-5 is published in the following peer-reviewed journal.

1. M. Arif Hussain Ansari, and Choi Look Law. "Grating Lobe Suppression of Multi-cycle IR-UWB Collaborative Radar Sensor in Wireless Sensor Network System" *IEEE Sensors Letters*, Vol. 4, No. 1, pp. 1-4, Jan. 2020.

The contributions of the co-authors are as follows:

- Assoc/Prof Choi Look Law provided the initial project direction and edited the manuscript drafts.
- I prepared the manuscript drafts. The manuscript was revised by Assoc/Prof Choi Look Law.
- I co-designed the study with Assoc/Prof Choi Look Law and performed all the laboratory work at the School of Electrical and Electronic Engineering. I analyzed the results, simulated data, and derived related mathematical models under the supervision of Assoc/Prof Law Choi Look.

15 December 2019

. . . . . .

Date

. . . . . .

Md Arif Hussain Ansari

Abstract

In recent times, impulse-radio ultra-wideband (IR-UWB) systems have gained significant attention for indoor positioning and short-range radar applications due to many of their inherent properties like ultra-fine temporal resolution, non-line-of-sight detection, multipath immunity, low power consumption, low-cost, etc. The critical challenge for the IR-UWB based systems is to generate an IR-UWB pulse, which is shorter in time and higher in amplitude. In particular, for the indoor-ranging and radar applications, the limited peak power of an IR-UWB pulse restricts the line-of-sight (LOS) range, non-line-of-sight (NLOS) detection and degrades radar imaging. In this thesis, two levels of improvement are proposed and demonstrated. Firstly, an MMIC design is presented at the chip-level to achieve higher peak power directly from the chip. Secondly, novel beamforming techniques are proposed, which superimpose transmitted pulses spatially to produce strong radiating beams. Finally, the proposed beamforming networks are optimized and prototyped.

The generation of the IR-UWB pulse is carried out through two successive stages on the MMIC, called as the impulse generator and the pulse former. The impulse generator generates a $7V$ sub-nanosecond voltage pulse, which is being used as an input to the pulse former stage. The pulse former performs the signal scaling, time-shifting, amplitude-reversal, and signal-addition to produce the desired Gaussian-enveloped multi-cycle IR-UWB pulse. The systematic circuit analysis is performed, and the effect of coupling capacitors on the amplification factor as well as impedance profile at each stage of pulse former are discussed in detail. In addition to this, the effect of temperature-dependent parasitic on the transient behaviour of the proposed IR-UWB pulse generator is analyzed, and the required mathematical model is derived. The proposed circuit is optimized for the highest possible output peak-power in the 3-5 GHz UWB band. The presented design is fully utilizing the existing 2 μm GaAs HBT cascode pair configuration, which significantly increases the output voltage swing while

reducing the total power consumption. The measured output pulse has a peak-to-peak voltage of 10.2 V for a 50 Ω load. The proposed pulse generator MMIC has a total power consumption of 122 μW at 100 kHz pulse repetition frequency and power efficiency of 9.8% (18.4%).

In order to further improve the peak power level in desired directions, the beam-pattern analysis of an electronically steerable multi-beam IR-UWB transmitter tag suited for real-time positioning systems is presented and demonstrated. Two linear arrays of four elements with an inter-element spacing of 18 *cm* and 10.2 *cm* are proposed and optimized. The array with a spacing of 10.2 *cm* is intentionally configured to produce orthogonal beams, which eventually provides better geometric dilution of precision (GDOP). The beam steering-angle analysis and an intensity table for the Gaussian-modulated multi-cycle IR-UWB beamforming array are provided. The proposed beamforming transmitter arrays are observed to achieve the scanning range from –60º (–90º) to +60º (+90º) with a scanning resolution of 5º and 8º in the measurements.

In addition to this, a novel algorithm for the separation between distributed wireless sensor nodes of the virtual non-linear array is proposed for collaborative beamforming in the wireless sensor network system. The proposed algorithm can produce a single beam radiation pattern of the collaborative virtual radar array. The presented radiation pattern is proposed for Gaussian-shaped multi-cycle IR-UWB beamforming, which effectively reduces the grating lobes despite electrically large separation between the transmitting nodes. A random error of positioning for sensor nodes and random jitter for different IR-UWB pulse is incorporated in the analysis, and related simulation results are provided. A prototype for the time domain beam-pattern measurement is developed for proof-of-concept. The measurement results show better than 6dB suppression for side lobes radiation.

I would like to

dedicate my Ph.D. thesis to

My Family in India.

Expressly to my

Caring Mother, Supportive Father,

Beloved Wife

&

Lovely Daughter "Asma"

Acknowledgement

I would like to begin by expressing my deepest gratitude to my academic supervisor Prof Law Choi Look. His time to time guidance and insightful discussions significantly helped me to understand the core of the topic, which enabled critical thinking into me for the research of interest. His enthusiasm for scientific research will be an inspiration for me to achieve my goals in the future. I am beholden to him and sure that I cannot express my gratitude by means of any word. I would also like to express thanks to my Thesis Advisory Committee (Prof Ng Geok Ing and Prof Li King Ho Holden). Their premeditated comments on my performance and progress certainly helped me to improve the overall quality of research and enriched my approach towards the problem.

In my day to day work, I am blessed with a sociable and cheerful group of fellow lab mates. Thanks to everyone for their moral encouragement, especially to Dr. Manmohan Sharma, Mr. Ankush Vashistha, and Mr. Anojh Kumaran. I have had many insightful discussions with them that have upgraded my understanding of related topics. I feel deeply honoured to express my earnest thanks to Nanyang Technological University Singapore for providing me with the NTU Research Scholarship. I would also like to sincerely acknowledge the financial support of ST Engineering for this research project and providing all the necessary resources during my research.

I am extremely grateful to my mother Janabah Hazra Khatoon, Father Janaab Md Athar Hussain Ansari, wife Nashra Iftekhar, Brother Md Asif Hussain, and all other family members for their unconditional love, countless blessings, and long-standing moral support. They encouraged me every time and motivated me at every phase of my life. I am indebted to them for everything that brings me to achieve so far. I would like to express a pleasing thanks to all my friends at Nanyang Technological University Singapore for always being so nice and helpful during my Ph.D. study.

Above all, I am grateful to the almighty ALLAH for providing me with all the grace required, good health, forbearance, and wellbeing that were necessary to complete this thesis.

Md. Arif Hussain Ansari
Date: 15 December 2019

Table of Contents

List of Figures

List of Tables

Acronyms

BPSK	:	Binary Phase Shift Key
BW	:	Bandwidth
CAGR	:	Compound Annual Growth Rate
DAC	:	Digital-to-Analog Converter
DLL	:	Delay Locked Loop
EIRP	:	Effective Isotropic Radiated Power
FCC	:	Federal Communications Commission
FWHM	:	Full Width at Half Maxima
GPR	:	Ground Penetrating Radar
GPS	:	Global Positioning System
IEEE	:	Institute of Electrical and Electronics Engineers
LDC	:	Low Duty Cycle
LO	:	Local Oscillator
LOS	:	Line-of-sight
MMIC	:	Microwave Monolithic Integrated Circuit
NLOS	:	Non-line-of-sight
OPA	:	Obstructive Sleep Apnoea
PPM	:	Pulse Position Modulation
PRF	:	Pulse Repetition Frequency
PSD	:	Power Spectral Density
RTLS	:	Real Time Location System
SNR	:	Signal to Noise Ratio
UWB	:	Ultra-Wideband
UWB-MC	:	Ultra-Wideband – Multi Carrier
UWR-IR	:	Ultra-Wideband – Impulse Radio
WSN	:	Wireless Sensor Network

Notations

f_c	:	Fundamental frequency/ Center frequency
T	:	Time period of a fundamental frequency
τ_1	:	Delay of impulse between each stage pulse former
τ_2	:	Delay of impulse by short circuit stub
f_c	:	Center frequency
f_H	:	Higher -10 *dB* cut-off frequency
f_L	:	Lower -10 *dB* cut-off frequency
m	:	Metre
cm	:	Centimetre
ns	:	Nanosecond
ps	:	Picosecond
m	:	Meter
$V_{p\text{-}p}$	:	Peak-to-Peak Voltage
V_{imp}	:	Impulse Voltage
V_{Be}	:	Breakdown Voltage for Earlier design
V_{Bm}	:	Breakdown Voltage for Modified design
L_p	:	Inductance due to PCB track
L_w	:	Inductance due to gold wire bonding
C_{cn}	:	Coupling capacitance of n^{th} stage of pulse former
C_π	:	Input capacitance of HBT
C_{je}	:	Forward *B-E* junction capacitance
C_{b0}	:	Diffusion capacitance at room temperature
C_{bT}	:	Parasitic diffusion capacitance due to temperature
T_c	:	Chip temperature
$t_n^{IG}(T_c)$	:	Delay due to parasitic in impulse generator
$t_n^{PF}(T_c)$	:	Delay due to parasitic in pulse former
$V_{UWB}(t)$	:	UWB pulse
P_{DC}	:	Total DC consumption
f_{PRF}	:	Pulse repetition frequency
ΔT	:	Relative Steering delay
d	:	Separation between nodes of conventional array

θ_0	:	Steering angle
λ	:	Wavelength of the fundamental frequency
P	:	Primary transmitting beam
S_p	:	Secondary beam at positive angle side
S_n	:	Secondary beam at negative angle side
Tx_{T1}	:	Transmitter Tag 1
Tx_{T2}	:	Transmitter Tag 2
A_1	:	Anchor 1
A_2	:	Anchor 2
σ	:	Standard-deviation of range measurement error
σ_x	:	Standard-deviation of the *x*-axis component
σ_y	:	Standard-deviation of the *y*-axis component
$A_G(\theta)$	:	Angular gain of the antenna
$J_R(i)$	:	Random error in steering delay
$k_R(i)$	:	Random error in IR-UWB pulse amplitude

Chapter – 1

Introduction

In this chapter, the motivation for the research is explained in detail. The market size and demand for Impulse Radio Ultra-wideband (IR-UWB) technology is provided. The problems associated with Real Time Location Systems (RTLS) and IR-UWB Radar are highlighted. The limitations of current IR-UWB technology are explained. The necessity for improving the IR-UWB technology is identified and described. The overall objective and scope of the current research work are provided. The major contribution of the conducted research is provided and discussed. Lastly, the organization of the remaining thesis is provided.

1.1 Motivation

In recent times, the impulse radio ultra-wideband (IR-UWB) systems have been considered as a promising technology for short-range wireless applications. It has various inherent properties such as ultra-fine temporal resolution, low power consumption, low cost, through the wall non-line-of-sight (NLOS) detection, multipath immunity, pulse communication like radar, etc., [1]–[5]. These attractive features of the IR-UWB technology show its strong candidature for short-range wireless sensor network (WSN) applications [6]–[9]. In 2002, the Federal Communications Commission (FCC) authorized the use of UWB technology for commercial usage under an unlicensed spectrum [10]. Ever since the declaration of this unlicensed spectrum, IR-UWB technology has drawn the attention of researchers around the globe for a wide-range of promising applications such as indoor positioning and tracking, vital-sign detection, ultra-fine infant movement detection, real-time monitoring of highways, bridges, and other civil infrastructure [10]–[18]. These applications have consequently been helping in the growth of the UWB market. In order to sustain this market, the demand for better performing UWB devices is exponentially rising. The market needs for better performing UWB devices motivates to investigate the application requirements and extract out the essential performance parameters for improvement. The estimation of UWB market size and requirements of UWB device characteristics for indoor positioning and radar applications are provided in the consecutive subsection-1.1.1 and subsection-1.1.2, respectively.

1.1.1 Market Size

The research reports published by an agency named *"Research and Market,"* highlight the growth of UWB technology for the different applications in the future marketplace [19]–[21].

The report claims that the UWB market was valued at US$ 62.9 million in 2016 and is expected to reach US$ 85.4 million by 2022, at a compound annual growth rate (CAGR) of 5.2% between 2016 and 2022. The published report highlighted that the UWB technology is expected to witness a significant penetration in indoor positioning applications in smart homes and retail stores between 2016 and 2022, to become a mainstream technology for tracking and location-based services. With an increase in awareness regarding the advantages of automatic asset tracking and management, the market for UWB-based RTLS/wireless sensor network (WSN) technology is projected to grow at an above-average CAGR between 2016 and 2022. The healthcare vertical led the UWB market in 2015, and the trend is expected to continue until 2022. The high acceptance rate of UWB technology in healthcare to track and monitor assets, personnel, and patients as well as to maintain a hygienic environment is the dominant factor behind the largest market share of the healthcare end-user segment.

In addition to this, IR-UWB radar for contactless vital sign detection, ultra-fine infant movement detection, etc. will be one of the dominant features for the adoption of UWB in the health monitoring industry in future. The study shows that UWB technology in the healthcare industry has the potential to grow at CAGR over 6.2%. The report indicated that the residential and manufacturing segments are expected to grow at a high rate in the UWB market between 2016 and 2022 because of the broad application and use cases of UWB technology in these industries. The report explicates that the key features of the UWB technology, which drives it into the market are the precision-range and rising market competitiveness. The RTLS/WSN application segment of the UWB market is expected to grow at the highest CAGR between 2016 and 2022.

Another report published by *"Research and Market"* forecasted that the RTLS is expected to grow from US$ 3.19 billion in 2018 to reach US$ 8.79 billion by 2023 at a compound annual

growth of 22.5% during 2018 to 2023 [21]–[23]. According to a recent market research report released by "*Transparency Market Research*," the global RTLS market is estimated to leap at a CAGR of 35.50% during the forecasted period between 2014 and 2020. The report, titled ***"****Real-Time Location Systems Market - Global Industry Analysis, Size, Share, Growth, Trends and Forecast, 2014 - 2020****"***, projected that the global real-time location systems market to be worth US$ 3.86 billion by 2020. The overall market was valued at US$ 0.46 billion in 2013.

Initially, the market was limited to North America, which held the largest share of the UWB market in 2015 owing to the extensive presence of major UWB players in this region. Moreover, the presence and early adoption of UWB technology in various industries such as healthcare, retail, and manufacturing in North America have contributed to the market dominance of this region. The U.S. is a major contributor to the growth of the UWB market in North America. In contrast with this, the UWB market in Asia-Pacific is expected to grow at the highest rate among all other regional markets for UWB between 2018 and 2022. In Japan, healthcare will reach a market size of US$ 3.2 Million by 2022. As the world's second-largest economy and the new game-changer in global markets, China exhibits the potential to grow at 5% over the next couple of years and add approximately US$ 4.9 Million in terms of addressable opportunity for the picking by aspiring businesses and their astute leaders.

During the early commercialization period of UWB technology, several start-ups with UWB product portfolio for communication and consumer electronics have emerged. The first UWB chip was commercialized by Wisair Ltd. (Israel) in 2004. However, the UWB technology did not succeed as anticipated in the early stages in terms of overall revenue and regulatory standards. In the first 11 years of its commercialization period, the overall market size of the UWB technology was less than US$ 60 million in the year 2015. The lack of a universal

regulatory framework, along with the high cost of UWB technology led to its low adoption in the consumer electronics segment.

Furthermore, the superior cost versus the performance trade-off of counterpart wireless technologies such as ZigBee, Wi-Fi, and Bluetooth had led to the lower adoption of UWB technology in the consumer electronics segment. Nonetheless, the UWB players such as DecaWave Ltd. (Ireland) and BeSpoon SAS (France) are offering cost-effective products without compromising on performance. These products are expected to boost the UWB market during the forecast period. DecaWave Ltd. (Ireland) ships the UWB chips at affordable prices, which is expected to open the UWB market to new startups, who are working with the UWB technology for the first time in various new applications such as autonomous driving, patient monitoring, augmented reality, and body area networks. More importantly, UWB technology is expected to witness high growth in the indoor positioning system, through-wall imaging, and collaborative radar sensor network due to its high temporal resolution characteristics.

1.1.2 Application Requirements

The high temporal resolution makes UWB technology a desirable candidate for indoor positioning and radar applications as compared to ZigBee, Wi-Fi, Bluetooth, etc. However, there are some limitations of the existing UWB systems, which restricts their growth to encompass the projected market size. The major limitations associated with current state-of-the-art UWB technology for indoor ranging are; (a) limited output peak-power (limited ranging) and (b) high power consumptions (high cost) [24]–[27]. The limited output peak power restricts the range of positioning as well as it directly affects the signal-to-noise ratio (SNR) of the path in the channel impulse response. The lower SNR degrades the quality of the back-scattered

received signals at various delays, which introduces error in final outcomes. The SNR plays an important role in ultra-fine movement detection. In addition, power consumption is always an issue for the WSN systems. The higher power consumption drains out the battery source quickly, which needs higher maintenance cost and makes the system expensive. In the next paragraph onwards, the author will explain the necessity of an energy-efficient high output peak-power IR-UWB transmitter in the context of the real application scenario. This thesis is mainly targeted towards two types of system applications; (a) IR-UWB transmitter tag for indoor positioning and (b) IR-UWB technology for radar application.

The IR-UWB transmitter generates an ultra-short time pulse [28]–[30], which leads to precise and ultra-fine temporal resolution for the real-time location systems (RTLS). More importantly, higher dynamic resolution as compared to narrow band system. The ultra-short time pulse inherently segregates from multipath, which provides ease in estimating accurate channel impulse response for a dynamic system. This is the main reason researchers around the globe are interested in developing IR-UWB systems targeted for RTLS. The RTLS is an electronic system that can track and identify the location of moving objects, mobile people, and an itinerant asset in real-time. In RTLS, readers and tags are arranged in the targeted area of application, where the reader receives signals from the transmitting tag and collectively determines the exact positions of moving objects consisting of the tag [31], [32]. However, in a cluttered indoor environment, the existence of multipath is common due to the presence of the concrete walls, wooden blocks, humans etc. These mediums are not good for electromagnetic waves (such as UWB signals) propagation, which causes high attenuation in the signal power [25], [29], [33].

The attenuation due to different medium (common building materials) for varying thickness values is provided in Table 1.1. It can be observed that the building materials are not a suitable

medium for UWB signals. In the worst case, the attenuation reaches up to 28 *dB* for masonry blocks of 610 *mm* thickness. The major problem arises when these media come in between the line-of-sight (LOS) path of the receiver and transmitter tags. The receiver is not able to get the information of the transmitting tag because of the considerable attenuation of the IR-UWB pulse within these media. Sometimes, the system confuses between the LOS and NLOS signal due to the larger propagation delay within the medium and provides inaccurate range results. The sketch of a typical indoor positioning and tracking environment with possible propagation conditions is shown in Figure 1.1. The room to room indoor positioning system is explicitly shown in the sketch to emphasis the NLOS indoor positioning system. There are mainly three types of paths, which could be followed by the IR-UWB pulse before reaching the receiver. However, in the real-world scenario, a combination of these three ways may be the effective path of propagation. The possible situations are stated below:

Table 1.1. Attenuation due to common building construction materials for different thickness of medium [33]

Materials	Thickness	Attenuation @ 900 MHz
Glass	6 *mm*	0.8 *dB*
	13 *mm*	2.0 *dB*
Lumber	76 *mm*	2.8 *dB*
Brick	89 *mm*	3.5 *dB*
	267 *mm*	7.0 *dB*
Concrete	102 *mm*	12 *dB*
	203 *mm*	23 *dB*
Reinforced concrete	203 *mm*	27 *dB*
Masonry Block	203 *mm*	12 *dB*
	610 *mm*	28 *dB*

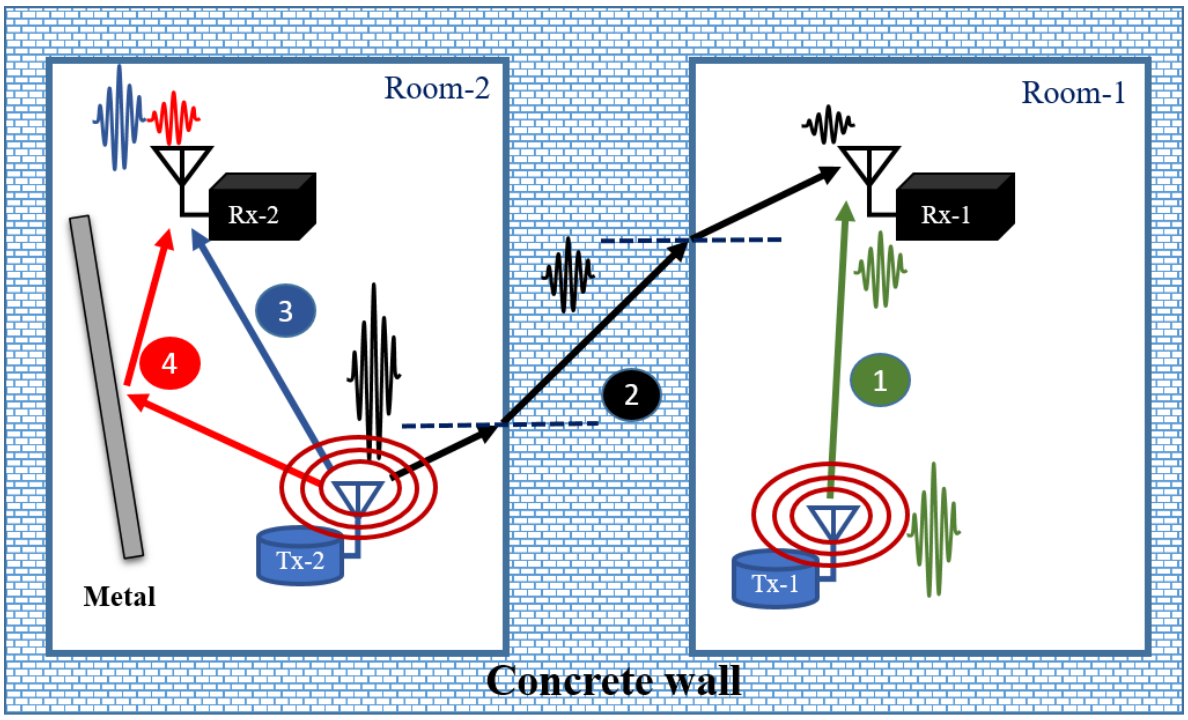

Figure 1.1. A typical illustration of propagation conditions in a dense cluttered indoor environment and respective attenuation in the IR-UWB Pulse.

- The IR-UWB pulse follows a direct path from the transmitter to the receiver without any obstacle in the direction of propagation; it is called line-of-sight (LOS), as shown in Figure 1.1 by ① and ③. The attenuation through these links is only caused due to free space (air) propagation. If the output peak power is small enough and the length of the links is large enough, then a high peak voltage pulse will be needed to cover the distance, such as nodes operating at airports, railway stations etc.
- The IR-UWB pulse follows the path from the transmitter to the receiver through an obstacle such as a concrete wall; it is called non-line-of-sight (NLOS), as shown in Figure 1.1 by ②. The attenuation inside the obstacle is non-trivial, which then requires a very high output peak power to see through it. The IR-UWB signal following the NLOS path is sometimes not able to reach the receiver, and often reaches the receiver with a power level below the reception threshold.

- The IR-UWB pulse follows the direct path as well as the reflected path, as shown in Figure 1.1 by ③ and ④. This situation leads to another issue called multipath. There are two or more pulses at the receiver, one following the direct path ③ and other following the reflected path ④. To distinguish between multiple arrived pulses and estimate the direct path peak, there must be enough time separation between the pulses. In other words, the transmitted IR-UWB pulses should be shorter in the time axis.

From the above discussion, it can be concluded that there are two main requirements of the IR-UWB system for indoor positioning and tracking applications within dense cluttered NLOS environment. i) The pulse width should be as short as possible, and ii) the output peak power should be as high as possible. Furthermore, for a robust system, the power consumption should also be as low as possible.

In addition to indoor positioning and tracking applications, the impulse radio UWB has great potential as a short-range radar due to one of its inherent properties of pulse communication. The basic principle of IR-UWB radar is same as regular radar operation, where the transmitter transmits an ultra-short pulse and receiver receives a back-scattered pulse or echo of the transmitted signal. The echo has the required information, which is extracted-out using appropriate reception techniques for further study.

In order to understand the IR-UWB radar working principle and requirements, a multilayer medium is modelled for a contactless imaging application. The electromagnetic properties of different modelled materials under test (MUT) is tabulated in Table 1.2 [34]. The impedance of different types of MUTs is shown in column 2 of Table 1.2, and the attenuation of the electromagnetic wave in corresponding layers is shown in column 3 of Table 1.2. The mechanism of the IR-UWB pulse radar for imaging is graphically illustrated in Figure 1.2 and

Figure 1.3 based on the modelled data tabulated in Table 1.2. The receiver can receive multiple echo signals from the different layers of the modelled medium. The reflections of the IR-UWB pulse principally depend on the impedance mismatch. As an example, the impedance of MUT-3 is in the order of 60 ohms, and impedance of MUT-2 is almost in the order of 50 ohms. Since IR-UWB radar works on electromagnetic waves, a reflection of 10% magnitude is expected at the MUT-3 and MUT-2 impedance mismatch boundary [34], [35]. The same rule could be applied to the other modelled layers interface.

Table 1.2. Electromagnetic properties of the different modelled MUTs [34].

	Impedance (Ω)	**Attenuation (m^{-1})**	**Speed (*m/sec*)**	**Thickness (*m*)**
Air	376.7	0.00 *dB*	2.998×10^{8}	1.00×10^{-2}
MUT-1	112.6	8.96 *dB*	8.958×10^{7}	0.96×10^{-2}
MUT-2	49.99	31.67 *dB*	3.978×10^{7}	1.35×10^{-2}
MUT-3	58.16	31.93 *dB*	4.628×10^{7}	1.16×10^{-2}
MUT-4	52.86	29.62 *dB*	4.206×10^{7}	5.78×10^{-2}
MUT-5	49.17	38.71 *dB*	3.912×10^{7}	---

The IR-UWB pulse and echo delay time for MUT-5 in the modelled multilayer medium are plotted in Figure 1.2. The IR-UWB pulse departed from the transmitter and propagated through the different layers of the medium to the MUT-5 and reflected back through the same medium towards the receiver. The propagation delay within the different layers is shown in Figure 1.2. Similarly, the attenuation of the IR-UWB pulse and its echo within the different layers of the medium from the transmitter to the receiver is shown in Figure 1.3. The attenuation is approximated as a linear within the layer, and multiple reflections are neglected for simplification.

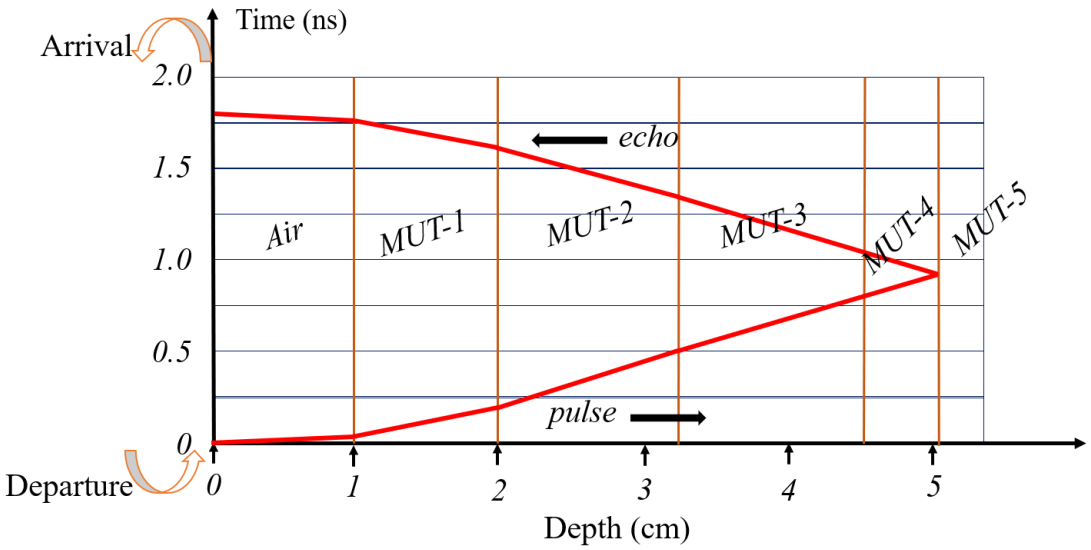

Figure 1.2. The predicted IR-UWB pulse-echo delays in the modelled multilayer medium [34]

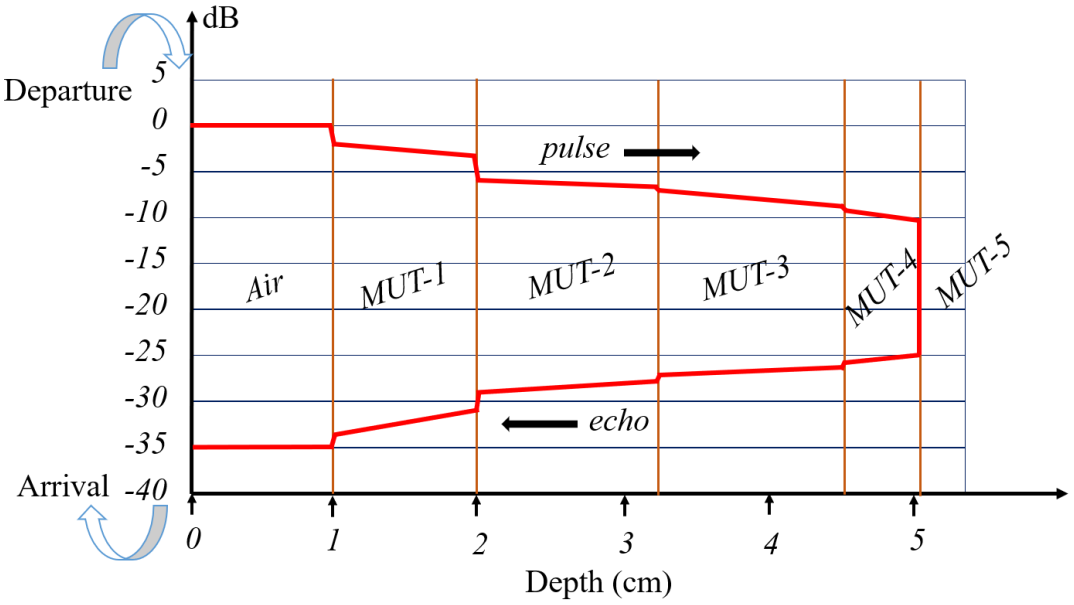

Figure 1.3. The predicted attenuation of the pulse-echo intensity traveling from the transmitter to receiver. The attenuation within the modelled multilayer medium is taken as linear for simplicity, and multiple reflections are ignored [34].

It can be noticed from Table 1.2, Figure 1.2, and Figure 1.3 that the impedance mismatch between different layers of the medium is small, which reflects less electromagnetic power. Furthermore, the attenuation in these mediums is high. Therefore, an IR-UWB pulse should have high peak-voltage to effectively penetrate through such a medium, and the reflected echo

should have significant peak-power to extract out the useful information. It is important to note that the high peak power pulse demonstrates better performance for lossy MUT layers. However, a high dynamic range receiver system is required to deploy for lossless or low loss MUT layers. Therefore, one has to choose the receiver system carefully and optimized as per the application requirements.

Another concern is to minimize the echoes from the surrounding environment for omnidirectional radar, which has a significant impact on the information extraction process. While it true that Omni-directional radar can perform empty room calibration for static clutter removal, but it cannot deal with dynamic clutter echoes. The echoes from the moving objects can be minimized by using the concept of a beamforming array. The beamforming can be applied at the receiver side as well as the transmitter side. The receiver beamformer's performance degrades because of noise due to scattering from other sides in case of Omni-directional transmitter. In addition, the low SNR from Omni-directional system arises difficulties for receiver beamformer to perform NLOS imaging. In contrast, the transmitter beamforming array can produce a focused narrow beam towards the observable object, which will have echo only from the object of interest and makes the system more reliable. Transmitter beamforming will not only produce a focused beam but will also help to further amplify the transmitted pulse. Furthermore, it enables the system to achieve less scattering and higher radiation efficiency. The application of transmitter beamforming radar is suitable for wall radar imaging, through-wall radar imaging, ground penetration radar, medical and health monitoring radar, etc.

From the above discussion on indoor positioning and radar application, the need for a high output peak-power IR-UWB transmitter is of utmost importance for effective practical applications. In the case of a cluttered indoor environment, an IR-UWB pulse with higher

output peak-power can penetrate concrete walls, wooden blocks, etc., and reach the receiver with desired minimum amplitude. It will also minimize the number of receiver modules required in the overall application area, which effectively reduces the overall cost.

In the case of IR-UWB radar, higher output peak-power is essential for effective NLOS imaging applications. The high amplitude IR-UWB pulse enables much stronger echoes, which gives more detailed information about the hidden objects such as behind the wall movements, objects assembled into the wall, objects underground etc. The achievable beam width and radiated power are limited by the size of the array as well as array increase the cost of the system. Therefore, one has to make a trade-off between beamwidth, radiated power, array size, and cost for a specific application and requirements. In conclusion, an energy-efficient IR-UWB pulse generator with highest possible peak-power is needed for the discussed applications to achieve precise positioning and fine imaging resolution. More importantly for a radar application, a narrow beam pointing towards the observable is needed to improve the imaging resolution as well as to minimize the effect of the dynamic surrounding environment on the feature's extraction process.

1.2 Objectives and Scope

As discussed in the last section, the main objective of this research work is to develop an energy-efficient IR-UWB pulse emitter node, which can generate highest possible output voltage pulse. In addition, the target here is to develop an electronically steerable beamforming transmitter arrays configuration, which can further amplify the transmitted pulse in the steered direction as well as help to reduce the scattering from the surrounding environment and improve radiation efficiency. The objective of achieving a high voltage pulse is for precise indoor positioning and tracking application as well as for better execution of a collaborative task in the wireless sensor network. It is important to note that both the applications principally need higher output peak power for better performance.

In order to achieve the anticipated objectives, the research is planned with multiple levels of breakthrough. Firstly, it has been decided to design and develop a distributed IR-UWB pulse generator circuit utilizing the previously used transistor technology to get the highest possible peak voltage pulse on-chip. Additionally, it has been anticipated to reduce power consumption and improve efficiency to at least up to the current reported range values. The projected research has been expected to provide an in-depth circuital analysis explaining the pulse formation process and effect of different circuit parameters on the IR-UWB pulse formation and generation.

The designed circuit of the IR-UWB pulse generator is now limited by the fabrication technology. Hence, the transistors would breakdown for higher output peak-power. Therefore, the design and development of beamforming arrays are projected for the second level of breakthrough. The beamforming transmitter array would further amplify the transmitted pulses by spatial superimposition. It has been projected to develop an array configuration with a viable practical length of 0.5 m. The projected array has been expected to produce steerable beams,

which would help to get precise positioning of mobile nodes by utilizing the GDOP techniques. Moreover, it has been projected to study the effect of different parameters of the array on beam-pattern synthesis.

The radiating beam of a 0.5 *m* length array could produce higher output peak-power based on the number of transmitting elements in the array. However, the beam-width of a 0.5 *m* array length would not be proper for long-range indoor positioning such as cluster-to-cluster positioning, more importantly for a radar imaging application. Therefore, the development of an algorithm for the formation of a virtual collaborative array with narrow beamwidth radiation pattern has been projected in the third level of breakthrough. The projected collaborative array has been expected to produce a steerable single narrow beam radiation pattern despite a separation of larger than one wavelength between the IR-UWB transmitting nodes. In addition to this, an in-depth analysis of the radiation pattern and the effect of error in nodes positioning and jitter in the synchronization clock has been projected. It is to note that the objective of the research had to develop an algorithm of virtual array formation as well as radiation pattern synthesis and analysis. A minimum viable prototype for the radiation pattern measurements and verification of the proposed algorithm has been also anticipated.

1.3 Major Contribution

The author begins with a top-down analysis of the state-of-the-art technology by looking at the fundamentals of the IR-UWB pulse generation and IR-UWB transmitter beamformer. After extensive study and several simulations, an energy-efficient high peak power IR-UWB transmitter MMIC is proposed and fabricated using 2 μm GaAs HBT process. The highest possible on-chip peak-power for an IR-UWB pulse generator is demonstrated to the best of authors' knowledge.

In alignment with the anticipated objectives, a multi-beam transmitter beamforming array configuration utilizing the GDOP technique is proposed. The proposed array can significantly improve the peak-power level of the transmitted signals. Besides peak-power level improvement, the proposed array comes with the additional capability of utilizing GDOP techniques to improve indoor positioning and tracking accuracy. The GDOP technique enabled multi-beam array ultimately helped to achieve the goal of precise indoor positioning and tracking. The proposed multi-beam transmitter array is prototyped, and the steerable multi-beam radiation pattern is demonstrated.

Furthermore, to achieve the projected objectives for the high-resolution NLOS imaging radar system, an algorithm for collaborative beamforming to produce a single beam radiation pattern despite a separation of larger than one wavelength is proposed. The required prototype for the measurement of the collaborative array's radiation pattern is developed and demonstrated. The detailed major contributions of the thesis are explicitly provided in bullet points as follows:

- An energy-efficient high peak power IR-UWB transmitter tag MMIC design and its optimization are presented. The improvement technique (using a cascode pair) to get a

significantly higher output voltage swing is demonstrated. An in-depth circuital analysis is performed and explained. The impulse voltage generation process is explained in detail. The analysis of the distributed pulse former circuit is performed to get the proper impedance match and precise amplitude control of impulse voltage at each stage of pulse former. The temperature-dependent parasitic effect is studied and the individual temperature dependent transient delay of each stage of the IR-UWB pulse generator is calculated. The effects of transient delay on IR-UWB pulse formation and beamforming are explained.

- The 2 μm GaAs HBT process is used for the fabrication of the proposed MMIC. The measured peak-to-peak voltage of the generated IR-UWB pulse is 10.2 V (24.15 dBm) for a 50 Ω load impedance, which is the highest reported amplitude to the best of the author's knowledge. The generated UWB pulse is centred at 4.45 GHz with a –10-dB bandwidth of 2 GHz. The total power consumption is 0.122 mW at a pulse repetition frequency of 100 kHz and a power efficiency of 9.18% (18.4%) is obtained.
- An attractive way of achieving better accuracy in the case of an autonomous robot deployed in the industrial environment is presented. A multi-beam IR-UWB transmitter array is proposed, implemented and related measurement results are provided. The beam steering-angle analysis is presented. The radiation intensity calculation is performed, and an intensity table is proposed. The intensity table helps to determine the intensity of the radiated pulse and quantify the broadening of the radiated pulse in terms of the number of carrier cycles.
- Eventually, two transmitter arrays with separation of 18 cm and 10.2 cm are optimized and demonstrated. The array with spacing of 10.2 cm is found to be better for the use case explained in the thesis. The optimized arrays are tuned to different steering angles and time-domain radiation patterns are plotted. Comparison between the simulated and measured radiation pattern is provided, which shows a great match. The true-time digital delay cell is

exploited, and the steering range from -60º (-90º) to +60º (+90º) with a scanning resolution of 5º and 8º is successfully achieved and demonstrated.

- The proposed algorithm for separation between the autonomous transmitting nodes is simulated and prototyped. The results of the different case for a collaborative virtual array are analyzed and optimized for better performance. The proposed algorithm is implemented to verify the radiation pattern of the transmitter array. An error analysis is performed to see the effect of positioning accuracy and jitter of the transmitting nodes.
- A prototype is developed using true-time delay cells, IR-UWB pulse generator and UWB antenna. Delay calibration of the true time delay cell is performed for beam steering. Two different transmitter arrays are scaled-down and optimized for the measurement. Minor lobe suppression of 6 *dB* is achieved for the array $N = 4$, $d = [10, 6, 10]$ *cm* steered at 0º. For the worst-case scenario, a suppression of 4.25 *dB* is achieved for the array $N = 4$, $d = [12.5, 7.5, 12.5]$ *cm* steered at 0º and 14º. The 4-element array achieves 13.5 *dBi* gain and 80% efficiency.

1.4 Organization of the Thesis

The thesis aims to provide a comprehensive understanding of the IR-UWB system specifications and requirements for indoor ranging and radar applications. A prospective method to achieve the requirements of high peak output power is discussed in detail. An approach to get the highest possible peak-power on-chip as well as beamforming array configurations to spatially amplify the transmitted pulse for precise indoor positioning and radar sensor networks is proposed and demonstrated. The thesis is organized into six chapters. An overview of the remaining chapters is summarized as follows.

In Chapter – 2, an introduction to ultra wideband technology, including a brief discussion of its history, definition, IR-UWB spectrum regulation and its inherent properties is provided. A review of IR-UWB pulse generation techniques, beamforming techniques, and collaborative virtual beamforming array is discussed. In addition, a comparative summary of the commercially available devices is provided.

In Chapter – 3, the proposed IR-UWB pulse generator design and its optimization are discussed in detail. The systematic circuital analysis of the pulse former is discussed, and related simulation is performed. The effect of temperature on the pulse generator is analyzed. The fabrication detail along with measurement results are provided and discussed.

In Chapter – 4, the proposed electronically steerable multi-beam IR-UWB transmitter array configuration is optimized and prototyped. The beam-steering angle analysis along with the intensity table is provided. The radiation pattern measurement results compared with simulation results are discussed.

In Chapter – 5, an algorithm for collaborative array formation is explained, and the corresponding mathematical model is derived. The beam pattern error analysis is performed

and discussed. A prototype for radiation pattern measurements of the collaborative array is developed. A comparison of the measurement results with simulations is provided.

In Chapter – 6, a summary of the conclusions is provided. The recommendation of future work is projected for further research and development.

Chapter – 2

Literature Review

In this chapter, introduction to the ultra-wideband technology, including a brief discussion of its history, definition, and its inherent properties is provided. In addition, the spectrum of ultra-wideband communication under the new FCC regulations is discussed. A literature review on the IR-UWB pulse generation architecture, beamforming transmitter array techniques and collaborative beamforming virtual array is provided. The literature is further organized in different categories under each topic. The basic working principle or architecture using a block diagram is explained. The pros and cons of each category are highlighted. A suitable architecture or method is adopted for further research on the topic based on the requirements. The reasoning behind the selection of techniques for the proposed work is explicitly highlighted. Finally, a brief study of the commercially available products is also provided in this chapter.

2.1 Introduction to UWB Technology

2.1.1 Brief Historical Evolution

The concept of Ultra-Wideband (UWB) technology was first formulated by Gerald F. Ross in the early 1960s while doing research in time-domain electromagnetics receiver design. He was awarded the first UWB communications patent for generating and receiving base-band impulse signals of sub-nanosecond duration without distortion in 1973. The short-pulse transmission and receiver system was developed during research at the Sperry Rand Corporation [36]. In 1974, a UWB radar system was designed by Morey for ground-penetrating radar (GPR) applications. The GPR became a commercial success at geophysical survey systems. Consequently, other developments were reported and patented by various research organizations [37]. By 1975, it was possible to build a UWB system using commercially available products from Tektronix. In 1978, G. Ross together with Bennett published a report on a complete study of the UWB system design. A reference schematic design of a UWB radar system was presented in the published report [38]. The paper discussed essential components of the basic reference design for a sub-nanosecond time-domain electromagnetic system.

After the 1970s, the emphasis steered in the direction of developing specific components of the known technology. Research groups started to understand the implications of transmitting transient pulses in a world dependent on non-interfering radio frequency communications and sensing. There remained no major obstacle to progress in perfecting such systems. After the 1970s, the only innovations in the UWB field could come from improvements and idealization of subsystems such as engineering trade-offs of time, bandwidth, signal-to-noise ratio, and electronic complexity. The essential components were known, e.g., pulse train generators, pulse train modulators, switching pulse train generators, detection receivers, and wideband antennas. Moreover, the subcomponents and methodologies were also known, e.g., avalanche

transistor switches, light-responsive switches, use of "subcarriers" in coding pulse trains, leading-edge detectors, ring demodulators, monostable multi-vibrator detectors, integration and averaging matched filters, correlation detectors, signal integrators, synchronous detectors and antennas driven by stepped amplitude input [37]–[40].

The ultrawide-band technology has gained momentum in the 1990s due to its application in the military as an impulse radar and data communication. The military radar was using UWB for better spatial resolution [41]. The UWB data communication using a sub-nanosecond pulse was allowing high data rate, multi-use management and transmission without the need for a carrier. In 2002, the first regulatory report was issued by FCC after recognizing the potential advantages of UWB technology. The issued report allowed the transmission of UWB signals in the unlicensed spectrum band (3.1 *GHz* – 10.6 *GHz*) for short-range communication and radar-imaging applications. An extensive constraint on power spectral density was imposed for the radiation of the UWB signal [10]. Nowadays, UWB technology is an emerging research topic in the field of short-range wireless communication for a variety of applications, such as the generation of large numbers of pulses in a short time interval, which is suitable for high data rate communication applications. Its lower power spectral density makes this technology well suited for military applications due to its low probability of detection. Its excellent time resolution makes a perfect candidate for short-range radar and imaging applications. It has the ability to resolve the multipath delay in the nanosecond range, which makes it ideal for indoor ranging applications [42].

2.1.2 Definition and Specifications

A UWB signal is defined as a signal which occupies ultra wide-bandwidth as compared to a narrowband signal in the frequency domain as shown in Figure 2.1. In addition to this, the power spectral density is comparatively lower than a narrowband signal. Usually, the UWB signal operates with a spectral density below the noise level as depicted in Figure 2.1. The UWB pulse in the time domain is reasonably shorter due to the ultrawide-bandwidth, and peak power is considerably high as compared to a narrowband signal shown in Figure 2.1.

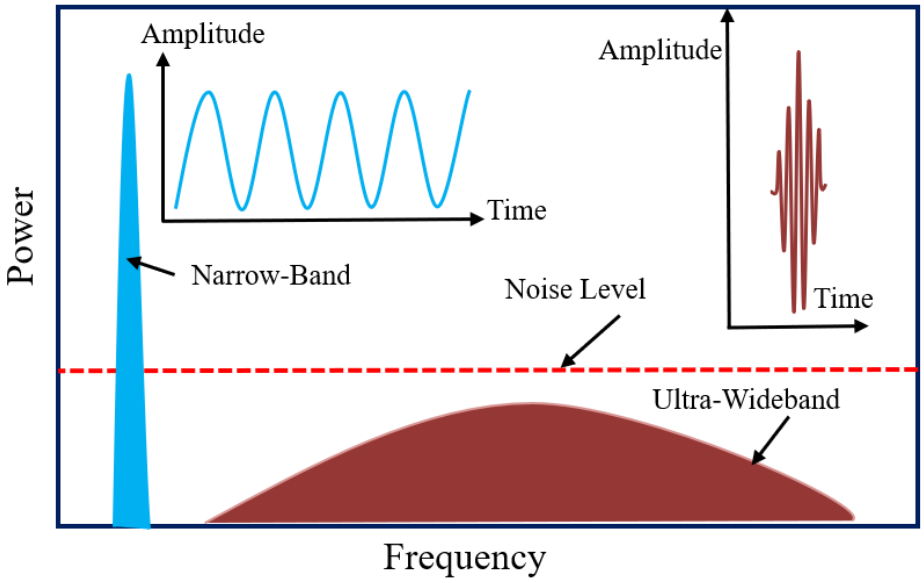

Figure 2.1. The comparative depiction of UWB signal with a narrow-band signal in the time domain as well as frequency domain

The FCC has defined the UWB systems as "any wireless system that occupies an absolute bandwidth larger than 500 *MHz* with the centre frequency (f_c) larger than 2.5 *GHz*, or having a fractional bandwidth larger than 20% with f_c lower than 2.5 GHz, is called UWB system" [10]. The f_c is the centre frequency at which the UWB signal has the maximum power density. The frequencies f_H and f_L are called higher and lower edge frequency, respectively. The f_H and f_L define at the location where the power spectral density is -10 *dB* below the maximum power density at centre frequency f_c. The fractional bandwidth is defined in (2.1) [42], [43].

$$BW_{frac} = \frac{BW}{f_c} \tag{2.1}$$

Here BW_{frac} is the fractional bandwidth and BW is the -10 dB absolute bandwidth of the UWB signal. The centre frequency (f_c) and the fractional bandwidth (BW_{frac}) can also be defined in terms of lower and higher edge frequency as shown in (2.2) and (2.3).

$$f_c = \frac{f_H + f_L}{2} \tag{2.2}$$

$$BW_{frac} = \frac{2(f_H - f_L)}{(f_H + f_L)} \tag{2.3}$$

The UWB technology appears as one of the most promising short-range wireless systems as compared with the narrowband RF system. UWB occupies larger bandwidth with a strictly regulated spectrum radiation power level, and hence acts as noise and does not interfere with any existing communication systems sharing the spectrum [44], [45]. The inherent properties of the UWB based systems are described as follows [44]–[52].

- *High temporal resolution:* The bandwidth of UWB systems is much higher than the existing narrowband systems. Therefore, UWB signals have a high temporal resolution. Typically, the width of UWB pulses is in the range of nanosecond or sub-nanosecond. This excellent temporal resolution of a UWB system is advantageous for ranging and positioning. The capability of resolving the delays in the range of 0.1 *ns* to 1 *ns* enables it to estimate the position of a transmitting tag with an accuracy of 3 *cm* to 30 *cm*.
- *Robustness against multipath fading:* In general, the narrowband systems suffer from multipath fading, which interferes with multiple path signals at the receiver. However, in the case of carrier-less impulse radio ultrawide-band signals or ultrashort UWB pulses, the multipath propagation delays of even less than 1 *ns* can be easily resolved.

- *Low power spectral density:* The low power spectral density of UWB signals is not intrinsic, but it is imposed by the radio spectrum regulatory board authority. It is indeed an important task to restrict the spectral radiation of the UWB signal. The bandwidth of UWB signals is spread over a wide range of the spectrum that makes it likely to coincide with the frequency bands already allocated for other existing radio systems. In order to allow the peaceful coexistence of the UWB systems with other narrowband systems, the power spectral density of UWB is limited to -41.3 *dBm/MHz*, which is equal to the unintentional radio transmission limit. The low power spectral density improves the safety of the UWB communication, which only persists for a comparatively shorter range than the narrowband signals.
- *Good obstacle penetration:* UWB comes under the electromagnetic wave spectrum, which offers excellent penetration capability into walls and non-metallic medium. The penetration depth is notably better for a lower frequency band of the allocated spectrum. The penetration through walls and other non-metallic medium enables the UWB systems to be utilized for non-destructive testing, through-the-wall imaging and other potential applications.
- *Protected and secure communication:* The UWB signals are spread over a broad range of spectrum and transmitted with a shallow power spectral density, close to the noise floor level of traditional narrowband radiocommunication receiver systems. These characteristics inherently enable secure transmission with a low probability of detection and interception.

2.1.3 Limitation of UWB techniques

Although various advantages of using UWB for indoor positioning is highlighted, there are some disadvantages associated with UWB technology.

- *Limited communication range:* Low spectral density indeed gives the flexibility to use the allocated frequency spectrum with the existing narrowband system. However, due to restricted EIRP level, the range of communication is limited.
- *Low data rate versus high output power:* The EIRP limit of FCC regulation can be satisfied with higher output power, provided the data rate is reduced arbitrarily low. Therefore, one has to make a trade-off between data rate and communication range. Achieving long-range sensing and higher data rate communication using the same bandwidth is principally challenging for UWB system. However, different pulse bandwidth could be utilized for the different task using a reconfigurable transmitter.

2.1.4 Spectrum Mask Regulations

There are several narrowband wireless systems coexisting with UWB systems. In order to protect existing radio systems from UWB interferences, regulatory bodies across the countries have released rules and emission limits for wireless UWB systems. In this thesis, the spectrum regulation released by FCC in the USA, the European Radiocommunications Office (ERO) in Europe and the Infocomm Development Authority (IDA) in Singapore are discussed. However, the regulation released by FCC is taken into consideration for the UWB emitter development.

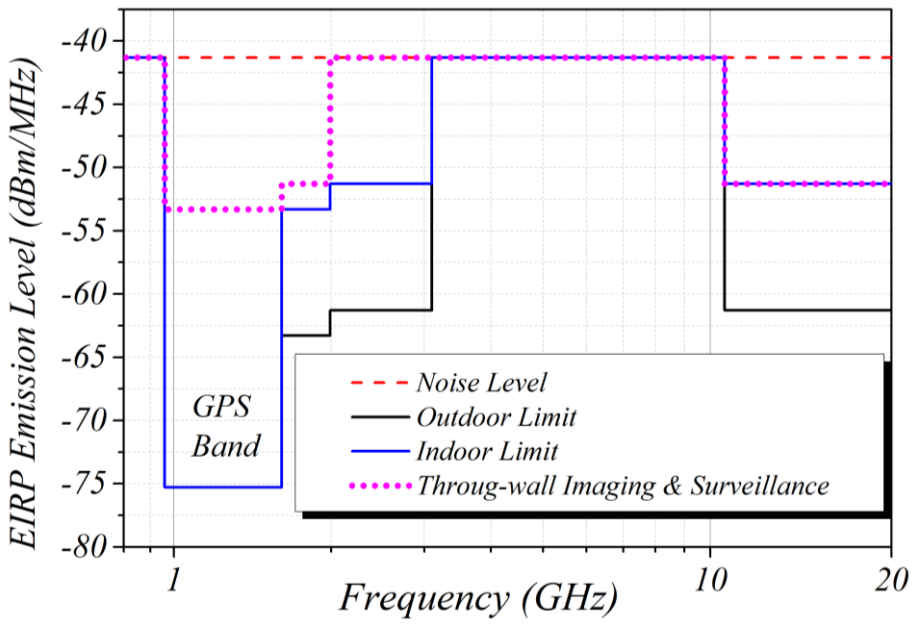

Figure 2.2. FCC designated emission mask limits for noise level, outdoor limit, indoor limit and through-wall imaging & surveillance [10] [41].

In 2002, the FCC approved the UWB unlicensed spectrum mask limit for commercial use and development of products in the specified frequency range [10], [46]. UWB systems are permitted to operate in the frequency range of 3.1 *GHz* to 10.6 *GHz* with minimum used bandwidth of 500 *MHz*. Under the new FCC regulations, the peak power of any unlicensed UWB emitter should not cross 0 *dBm* in a 50 *MHz* bandwidth, and the average power limit is -41.3 *dBm/MHz* [46].

The FCC categorized UWB systems into various types and released corresponding individual spectrum limits for each type. The detailed spectrum regulations for other types of UWB devices can be found in [10], [41]. The regulated spectrum mask limits allocated for UWB communication and measurement systems is shown in Figure 2.2. The emission limit for indoor and outdoor UWB systems is further differentiated. The EIRP limit for through-the-wall radar imaging and surveillance is co-plotted in Figure 2.2. The total average available power is minimal as compared to Wi-Fi or other existing narrowband systems. In addition to this, FCC

does not restrict the use of the entire available bandwidth, although it has given the flexibility to choose the operating frequency and desired bandwidth, which effectively reduced design complexity, design time and design cost [47].

The European Radiocommunications Office (ERO) is the facilitator for the European Technical Standards Institute (ETSI) and for the European Conference of Postal and Telecommunications Administration (CEPT), which deals with UWB spectrum sharing and compatibility studies. The UWB spectrum mask limit released for the European countries is shown in Figure 2.3. The bandwidth under European UWB regulation is 2.5 GHz.

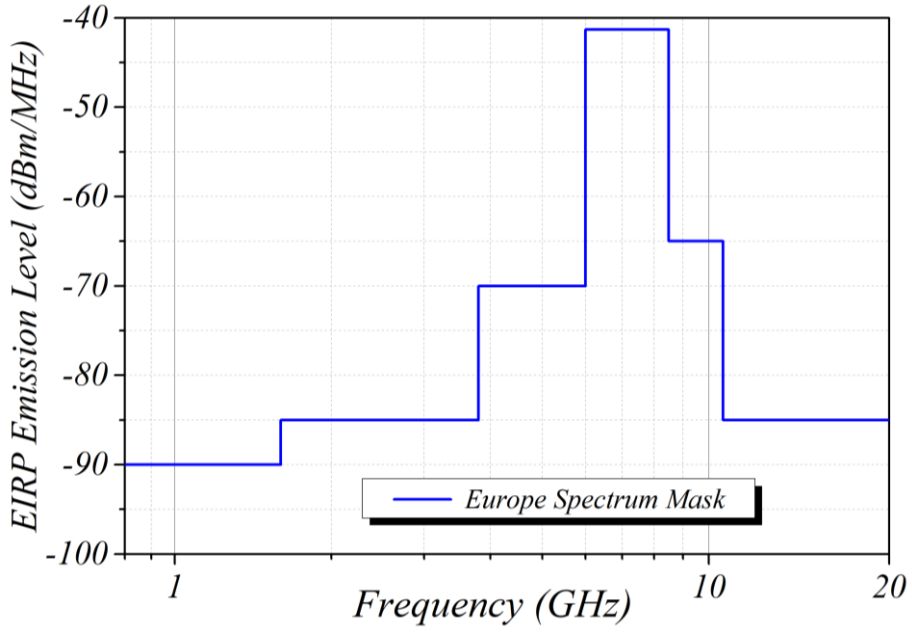

Figure 2.3. European spectrum mask limit [53]

The spectral emission limit for UWB in Singapore is regulated by the Infocomm Development Authority (IDA). The spectral limit for Singapore is shown in Figure 2.4. The bandwidth of UWB emission in Singapore is the same as the FCC regulation. Interestingly, the EIRP limit is for UWB emission in Singapore is -34 *dBm/MHz*, which is greater than the FCC limit of -41.3 *dBm/MHz*. Hence, the UWB emitter which follows the FCC regulation will be

able to operate in the Singapore region. In this thesis, the FCC spectrum regulation has been considered for UWB emitter design.

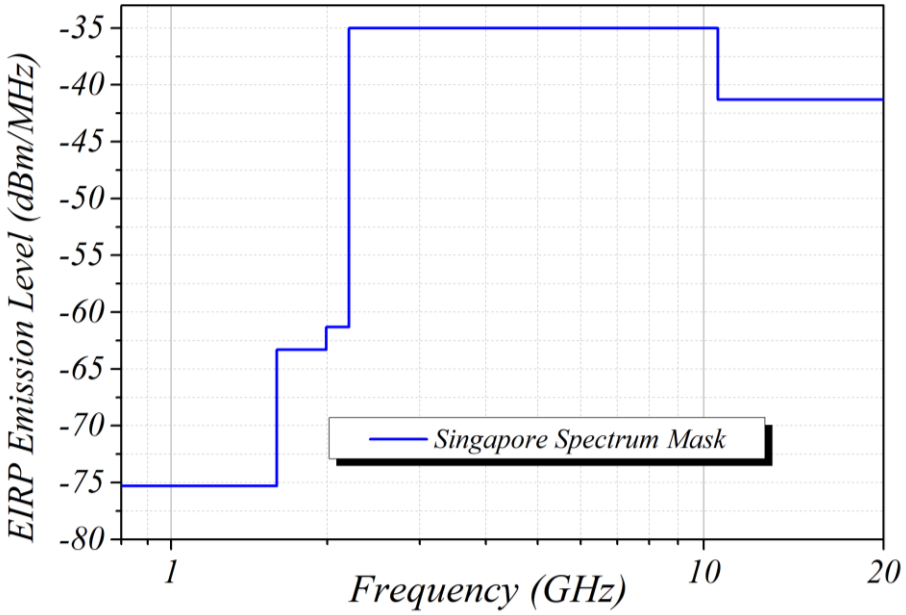

Figure 2.4. Singapore Spectrum mask limit [53]

2.1.5 Maximum Permissible Peak Power and Achievable Range

This section explains the maximum peak power permissible under the FCC regulation limit, which is based on the theory explained in [46]. The pulse repetition frequency (PRF) *vs* peak power is briefly explained and related calculation has been performed.

$$P_{ave} = P_{peak}\delta; \quad \delta = \tau R \tag{2.4}$$

The true average power of the UWB pulse waveform is given in (2.4), where δ is the pulse duty cycle, τ is the pulse width, R is the pulse repetition frequency, P_{peak} is the peak power of the pulse. If the same signal is measured using spectrum analyzer having resolution

bandwidth of B_R. Consider a case of low data rate, i.e. $R \ll B_R$. The average measured power is given in (2.5) and (2.6), where B_P is the 3dB full bandwidth of the pulse. Similarly, the peak measured power is given in (2.7) and (2.8).

$$P_{ave}^{m} = P_{peak}\tau^2 RB_R \tag{2.5}$$

$$P_{ave}^{m} = E_{pulse}\frac{B_R^2}{B_p}\tau_R R \tag{2.6}$$

$$P_{peak}^{m} = P_{peak}\tau^2 B_R^2 = P_{peak}\tau\frac{B_R^2}{B_P} \tag{2.7}$$

$$P_{peak}^{m} = E_{pulse}\frac{B_R^2}{B_P} \tag{2.8}$$

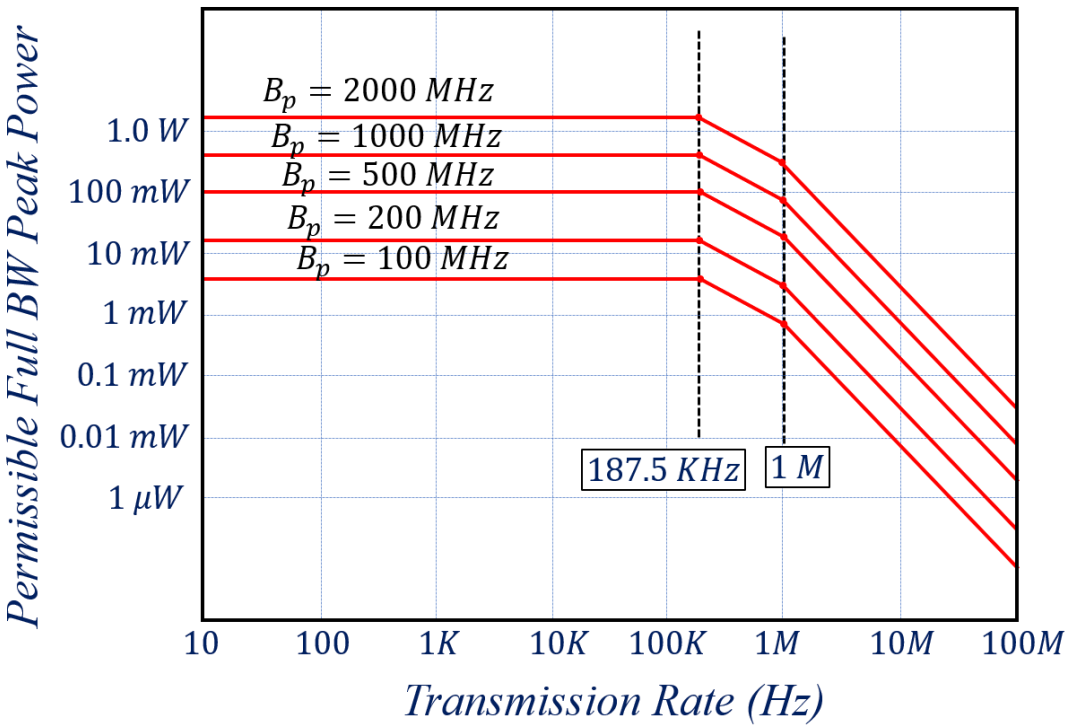

Figure 2.5. Full Bandwidth peak power constraint *vs* transmission rate for various -3dB pulse bandwidth [46].

It is to note that for a low data rate ($R \ll B_R$) UWB system, the peak power is dependent on resolution bandwidth of the spectrum analyzer and the pulse bandwidth. More importantly, it is independent of pulse repetition frequency. The Full Bandwidth peak power constraint *vs* transmission rate for various -3dB pulse bandwidth is shown in Figure 2.5. It can be observed from Figure 2.5 that for high data rate UWB system, the peak power limit decreases with the increasing data rate. However, it is interesting to see that for low data rate system (less than 187.5 *kHz*) the peak power limit is constant with the data rate.

The FCC spectrum regulation limit for average power and peak is given in (2.9) and (2.10), respectively. The maximum permissible measured peak power can be calculated from (2.5) to (2.8) using (2.9) and (2.10), which is given in (2.11) and (2.12). The calculated peak power assumes a rectangular envelope of UWB pulse, which may not be necessarily true for Gaussian enveloped UWB pulse. Therefore, the energy of the UWB pulse could be a better parameter to calculate, which will be true for all type of envelope. The maximum permissible energy of UWB pulse with 3*dB* bandwidth of 1*GHz* is 400*pJ*, provided a low data rate ($R \ll B_R$).

$$P_{ave}^{m} \le 75\,nW \quad in 1MHz\ resolution\ BW \tag{2.9}$$

$$P_{peak}^{m} = \left(\frac{B_R}{50 \times 10^6} \right)^2 \times 1mW; \quad 10^6 \le B_R \le 50 \times 10^6 \tag{2.10}$$

$$P_{peak}^{m}\Big|_{50\,MHz} = 1\,mW = E_{pulse}\,\frac{B_R^2}{B_P} = P_{peak}\,\tau^2 B_R^2 \tag{2.11}$$

$$E_{pulse} = 400\ pJ \quad and \quad P_{peak} = 400mW \tag{2.12}$$

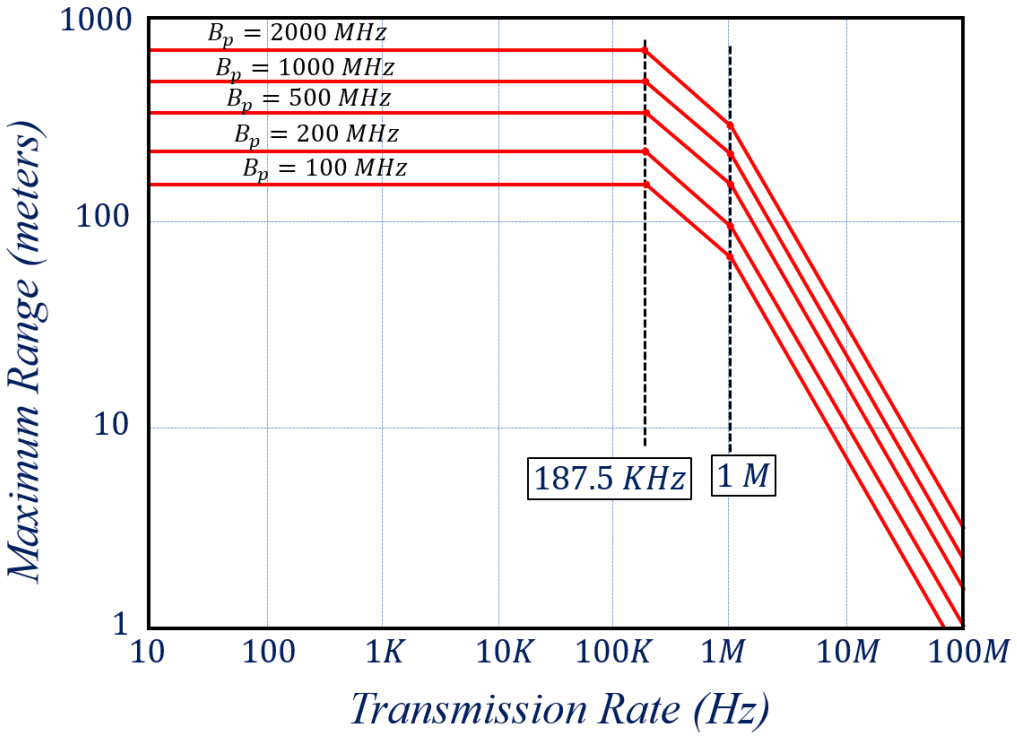

Figure 2.6. Maximum Achievable LOS Range *vs* Pulse Bandwidth and Transmission Rate [46].

Similarly, the maximum achievable range can be calculated using the Friis equation and the maximum permissible peak power plotted in Figure 2.5. The maximum achievable range is plotted in Figure 2.6. More details can be found in [46].

2.2 IR-UWB Pulse Generator

IR-UWB pulse generation and shaping are the critical functions of a wireless UWB system designed for indoor positioning and pulse radar applications. Recently, IR-UWB has emerged as one of the promising technologies for indoor positioning and tracking applications due to its inherent properties, such as ultra-fine temporal resolution, through-the-wall non-line-of-sight (NLOS) detection, multipath immunity, pulsed communication like radar, low power consumption, low cost, etc. [1]–[5]. There are numerous IR-UWB pulse generation techniques presented in the literature. However, IR-UWB pulse generation techniques based on the design architecture can be broadly classified into four major categories. These four categories are spectrum filtering, up-conversion, digital edge combining, and distributed waveform synthesizer [54]. A brief description of each category explaining the advantages and disadvantages is given as follows.

2.2.1 Spectrum Filtering

Spectrum filtering technique was a popular method in the early days' development of UWB pulse generators due to their simple architecture. The fundamental principle is to generate a delta-function like a baseband impulse with bandwidth much greater than the frequency band of interest. A pulse-shaping filter is then used to filter it out into the desired spectrum of frequency [5], [55]. The concept of spectrum filtering method is shown in Figure 2.7. A delta impulse function is usually generated using the impulse generator, the generated impulse is very short in time such that it has a wide range of frequency bandwidth. The generated delta-impulse function is fed through an optimized pulse shaping filter to get an IR-UWB pulse, which must satisfy the FCC spectral mask limits.

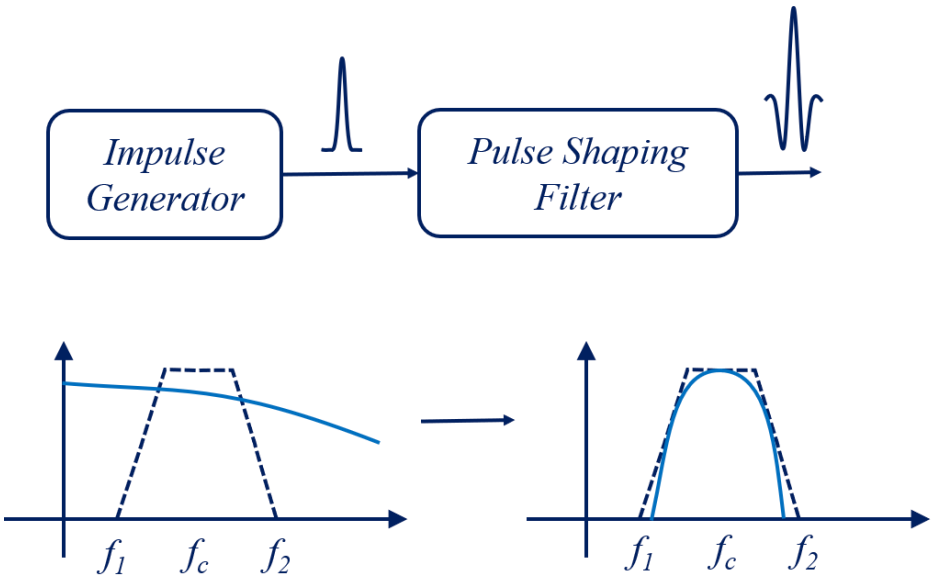

Figure 2.7. Pulse generation approach for the spectrum filtering method for FCC compliant IR-UWB pulse [54]

A step-recovery diode can be used to generate the ultra-fast impulse and a transmission line filter to shape it into a UWB pulse [5]. Greater than 5 Volt peak-to-peak output IR-UWB voltage has been reported using SRD and HBT [56], [57]. However, the reported pulses are limited to a monocycle pulse operating below 2 *GHz*. Spectrum filtering provides the advantage of simple implementation. Nevertheless, its efficiency is not good because a big portion of the spectrum is not in use. The shape of the generated pulse highly depends on the process variation when implemented on-chip. The quality factor of the filter fabricated on-chip is usually low, which makes the spectrum filtering technique inadequate and unstable. Thus, the pulse shaping filters are typically implemented off-chip [58], and therefore they have limited tuning capability. A UWB transmitter based on this pulse generation approach can only transmit a specific pulse shape, and hence, it is hardly reconfigurable. An active finite impulse response filter has also been proposed, however, it consumes a significant amount of power due to the need for a distributed network for a wideband impulse signal. [59]–[61].

2.2.2 Up-Conversion

The up-conversion method is relatively efficient as compared to the spectrum filtering method. In this approach, instead of filtering tens of gigahertz bandwidth, up-conversion method generates a baseband gaussian shaped signal and up-converts it to the targeted band of frequency using a mixer and local oscillator [62]–[64] A block diagram with a signal illustration of the typical up-conversion method is shown in Figure 2.8.

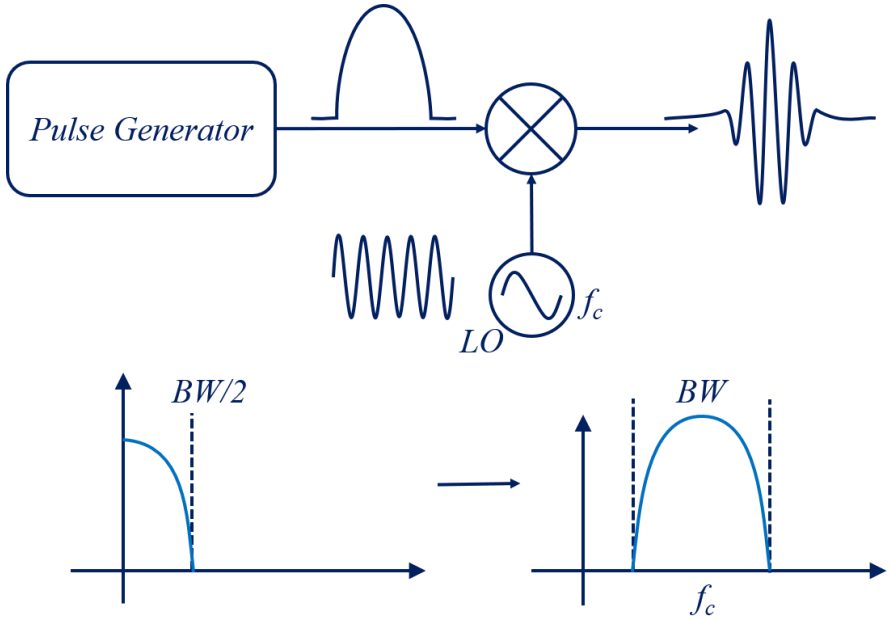

Figure 2.8. Graphical illustration of the pulse generation approach for the up-conversion technique of IR-UWB pulse [54]

The architecture of the up-conversion method is similar to the conventional narrow-band systems. Nevertheless, the carrier-based architecture increases the complexity and power consumption of the transmitter due to the need for a phase-locked loop (*PLL*) as the local oscillator (*LO*) and a mixer for up-conversion. In addition to this, the generation of baseband pulses with large bandwidth is equally challenging.

Another concern is the *LO* leakage to the transmitting antenna. Sometimes, it causes a reduction in transmitted power to remain FCC compliant. In order to overcome this issue, a

switching oscillator technique is presented. In this technique, a switching oscillator is turned ON and OFF for a few nanoseconds to get an IR-UWB pulse. An IR-UWB pulse generator using the switching oscillator has been presented for the 3-5 *GHz* band, 6-10 *GHz* band and multiband in the frequency range of 3-10 *GHz* [65]–[68]. The benefits of using the switching oscillator are a) better energy efficiency and b) reduction in *LO* Leakage. However, a major limitation associated is the transient time to start and stop the oscillator (typically a few nanoseconds) [69]. The relatively slow VCO transient behavior reduces the bandwidth of the IR-UWB pulses and henceforth, it degrades the TOA estimation accuracy in case of indoor positioning and limits the temporal resolution in case of radar as well [65].

2.2.3 Digital Edge Combining

The digital edge combining is the most popular approach for IR-UWB pulse generation with different techniques proposed over the years [8], [70], [71]. The fundamental principle is to delay and combine the rising and falling edge of the digital clock pulse. After the combination of digital pulses, it is fed through the pulse shaping circuit to filter out the off-band harmonics. The pulse-shaping filter must be optimized such that it produces an IR-UWB pulse compatible with FCC spectrum regulations for UWB emissions [8], [70], [72]–[74]. A typical block diagram with the graphical illustration of the signal at each stage is shown in Figure 2.9.

The delay to the digital data clock can be given using a chain of delay cell or delay-locked loop (DLL). A combination of the different delayed pulses is done through logic gates and then filtered out to remove the off-band harmonics. This method is easy to incorporate various kinds of digital modulation schemes such as binary phase shift key (BPSK) [71], [72] pulse position modulation (PPM) [75] etc. Another advantage is that most of the system design is digital

before filtering. The digital implementation can give the scaling of CMOS channel length in terms of speed and timing accuracy compared to other analog systems. It is power efficient and cost-effective (can be realized using low-cost digital process). However, its major shortcoming is limited output power, which effectively restricts the application of IR-UWB transmitter in a wide-range indoor sensor networks [24]–[26], [48], [76], [77]. The performance becomes even worse if the supply voltage is low as in the case of modern semiconductor process. In order to get a higher peak output power, an additional power amplifier is needed [8], [78], which substantially increases the overall power consumption.

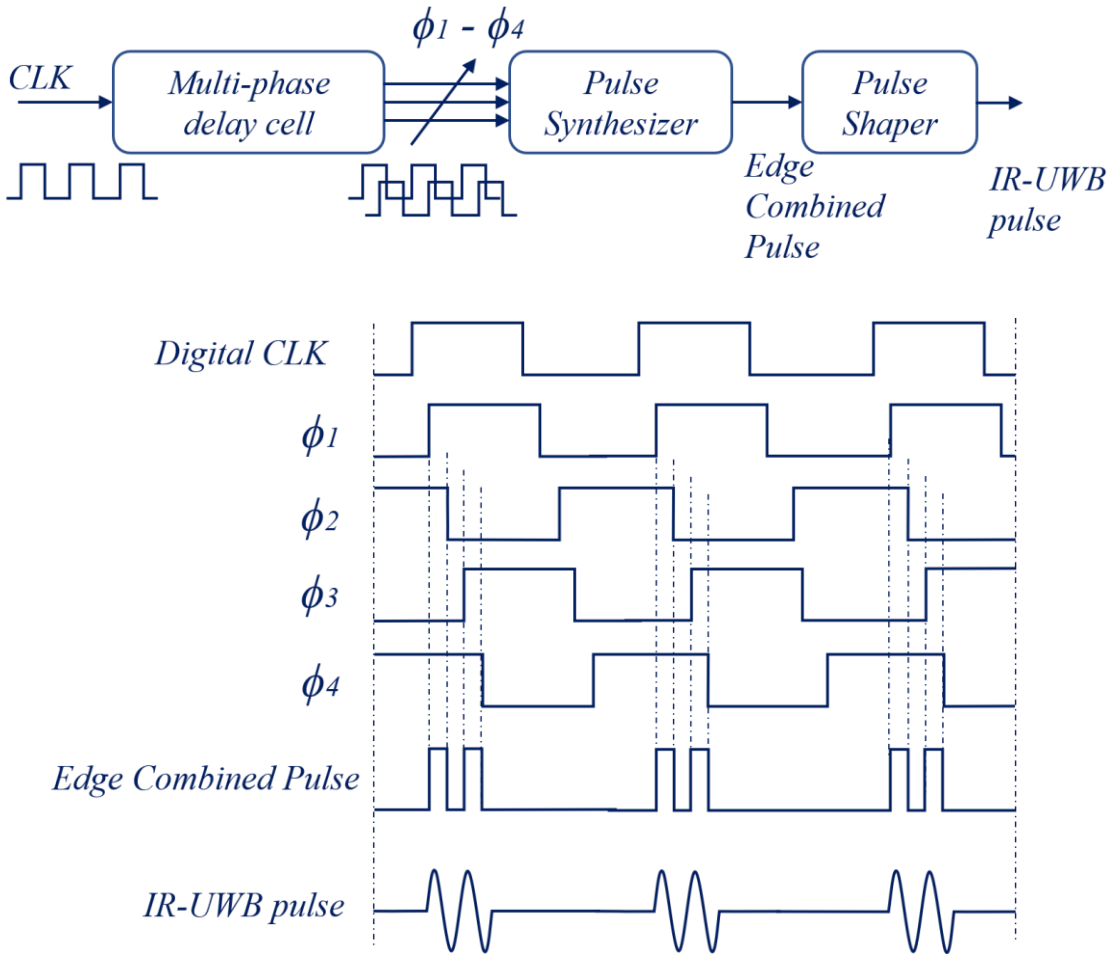

Figure 2.9. A typical block diagram with a graphical illustration of the digital edge combining approach of an IR-UWB Pulse generation [71]

The digital-to-analog (DAC) converter is also being used to generate the UWB pulse by means of multiphase sampling clock [73], [79], [80]. A high-speed DAC with good resolution can generate arbitrary pulse shapes and therefore it is fully reconfigurable. However, this technique is relatively less efficient due to the use of multiple DACs. The combination of DACs is also not able to achieve high output peak power without a power amplifier, which is the major limitation with the DAC based IR-UWB pulse generators. In addition to this, the requirement of high sampling rate increases the total power consumption [81].

2.2.4 Distributed Waveform Synthesizer

The distributed architecture of IR-UWB signal generators is a popular choice for broadband applications [82]–[85]. The deployment of artificial transmission-line structures between the different amplifier stages of distributed architecture solve the problem of broadband impedance match by simply incorporating the input and output capacitances. The amplifier consists of an input line, incorporating the input capacitances of the transistors and an output line incorporating the output capacitances. The signal on the input line is amplified and fed into the output line. As a result of this arrangement, the amplifier can operate over a very broad frequency range.

The typical block diagram representation of the distributed IR-UWB pulse synthesizer is shown in Figure 2.10 and a simplified version of the same topology is shown in Figure 2.11. In the distributed waveform synthesizer approach, a distributed amplifier is used to delay and combine several analog gaussian sub-nanosecond pulses with different polarities to construct a multi-cycle UWB pulse. A sub-nanosecond gaussian pulse $g(t)$ is fed to the power splitter that splits it into two gaussian pulses $g(t)^+$ and $g(t)^-$. The equally divided $g(t)^+$ and $g(t)^-$ pulses

are delayed and distributed to each tap with a specific (positive and negative) scaling factor. The distributed transmission lines are terminated with the matched load to minimize reflections. All the delayed and scaled pulse are combining at the output load to construct an IR-UWB pulse [9], [54], [86], [87].

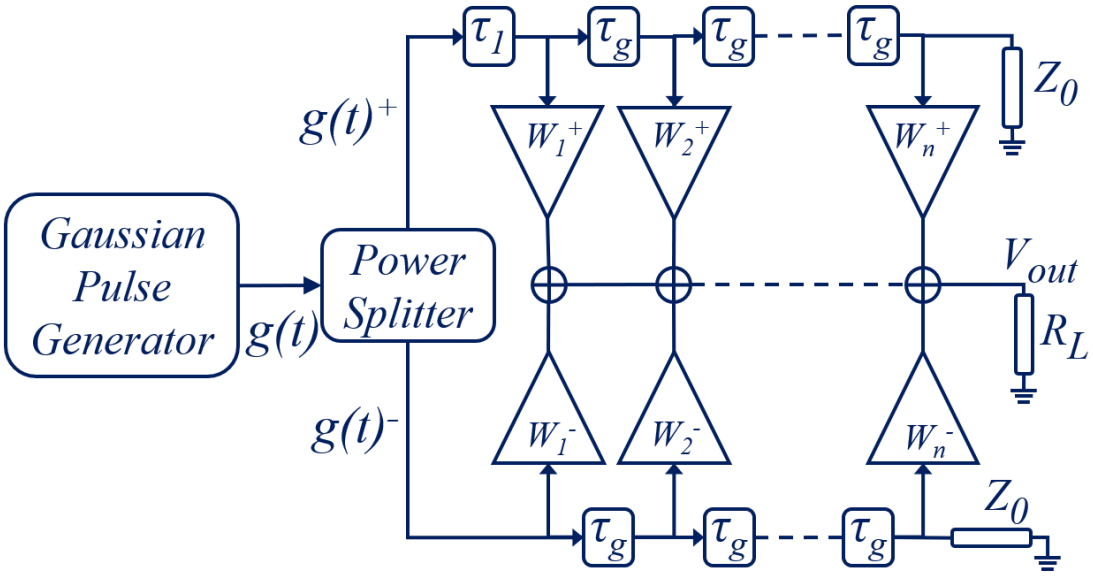

Figure 2.10. A typical representation of the distributed UWB pulse synthesizer

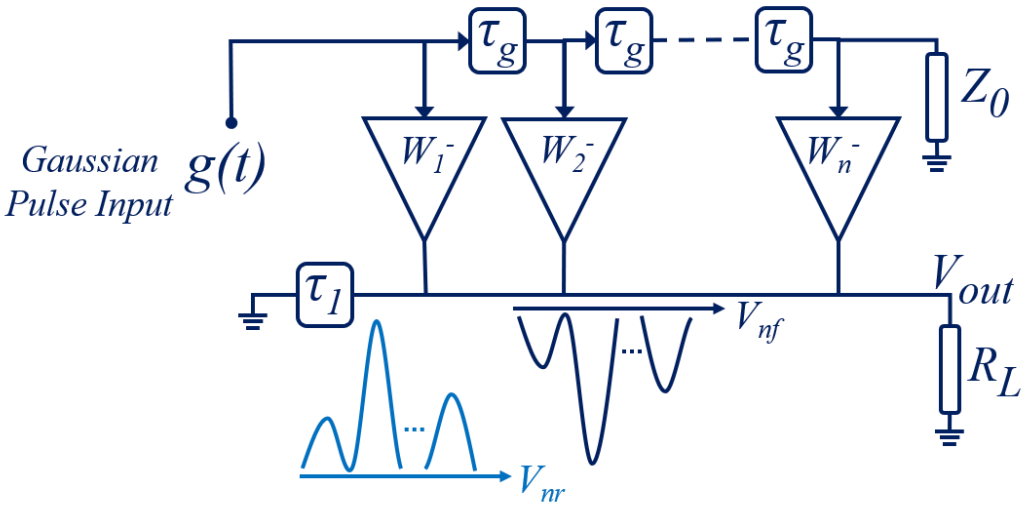

Figure 2.11. A simplified diagram of the above UWB pulse synthesizer

Among all the techniques, the distributed waveform synthesizer has the potential to generate a multi-cycle high voltage IR-UWB pulse with low power consumption. However, the transistor used for amplification at the different stages of distributed synthesizer network suffers breakdown at higher output voltage swings [9], [86], [87]. The breakdown of a transistor can be resolved by utilizing passive power combiner or transformer. Nonetheless, the use of a passive transformer will increase the losses, which will eventually make the pulse generator power inefficient. In addition, it requires a larger chip area, which results in a higher cost. A cascode pair transistors can also be utilized to significantly improve the output voltage swing without increasing the power consumption. In this thesis, the breakdown of the transistor junction is resolved by utilizing a cascode pair transistor. A distributed pulse generator circuit has been optimized and improved design is proposed to get a significantly higher peak-to-peak voltage IR-UWB pulse.

A detailed comparative study of state-of-the-art technology in terms of output peak power, pulse width, power consumption, etc., is provided in Table 2.1. It can be observed from Table 2.1 that the CMOS and Bi-CMOS are frequently used, which easily generates shorter time UWB pulse. However, these technologies restrict to get a higher peak-to-peak voltage pulse due to limited supply voltage. A power amplifier can be used to boost up the output peak power with an increase in power consumption. Remarkably, it can be noticed from Table 2.1 that SRD and HBT are able to produce higher peak-to-peak UWB pulse. However, the generated UWB signal is limited to the monocycle pulse. Furthermore, the GaAs based devices (relatively higher breakdown voltage) indicate that the generation of high peak-to-peak multi-cycle IR-UWB pulses is possible. It is important to note that non-CMOS technology has its drawback. The major drawback of non-CMOS technology is integration compatibility with existing CMOS chip. The integration of non-CMOS with CMOS technology is currently not possible,

which increase the cost of the whole on-chip system. Since most of the devices are fabricated using CMOS technology nowadays. Therefore, any component using non-CMOS must be fabricated individually and wire bond the complete system. This will not only increase the chip cost and make the system bulky but it also degrades the performance. In contrast, non-CMOS technology can provide higher ranging, which potentially reduces the overall cost of the system for indoor positioning and compensate the chip cost. In this thesis, a 2 μm GaAs HBT opted for fabrication and an IR-UWB design configuration is proposed, utilizing the same existing transistor (2 μm GaAs HBT), which effectively solved the breakdown issue and improved the circuit performance to get a significantly higher peak-voltage pulse. The complete design and circuit analysis of the proposed IR-UWB transmitter tag is presented in Section-2.3.

Table 2.1. State-of-the-art Technology of IR-UWB Pulse Generator

[Reference] (year)	Technique / Method	Technology / Process	V_{p-p}(V)	Efficiency	Pulse width (ns)	Pulse Type	Frequency Band	PRF	Power Consumption
[86] **(2010)**	Distributed Pulse Former	0.25 µm pHEMT	4.5 V	10%	1 nsec	Multicycle	3 – 5 GHz	10 MHz	5 mW
[87] **(2011)**	Distributed Pulse Former	0.25 µm pHEMT	6.4 V	13%	1 nsec	Multicycle	3 - 5 GHz	5 MHz	5 mW
[56] **(2006)**	Distributed Pulse Former	SRD	6 - 9 V	----	0.4 – 1.2 nsec	Monocycle	0.15 - 3.7 GHz	10 MHz	-----
[9] **(2010)**	Distributed Pulse Former	GaAs 2 µm HBT	6.32 V	10.4%	1 nsec	Multicycle	3 - 5 GHz	1 MHz	0.8 mW
[88] **(2014)**	Edge Combining	65 nm CMOS	0.8 V	----	2 nsec	Multicycle	3.1-4.8 GHz	200 MHz	0.72 mW
[89] **(2016)**	Edge Combining	65 nm CMOS	750 mV	----	0.75 nsec	Multicycle	6.9 – 9.3 GHz	28 MHz	1.8 mW
[15][90] **(2014)**	Edge Combining	0.18 µm CMOS	0.5 V	----	1.2 nsec	Multicycle	2-5 GHz	12.5 MHz	1.8 / 4 W
[91] **(2015)**	Edge Combining	0.18 µm CMOS	120 mV	----	2 nsec	Multicycle	3.5 – 4 GHz 4 – 4.5 GHz	100 MHz	1.69 mW
[8] **(2007)**	Edge Combining	0.18 µm CMOS	1.28 V	----	1.75 nsec	Multicycle	3.1 - 5.1 GHz	36 MHz	29.7 mW
[5] **(2010)**	Edge Combining	0.13 µm CMOS	1.42 V	6.4%	0.46 nsec	Multicycle	3.1 – 10.6 GHz	100 MHz	3.84W
[92][92] **(2006)**	Edge Combining	0.13 µm CMOS	0.2 V	0.05%	0.6	Multicycle	3 – 5 GHz	80 MHz	10 mW
[93] **(2014)**	Spectrum Filtering	0.18 µm CMOS	0.2 V	----	0.2 nsec	Monocycle	3.75-10.5 GHz	10 MHz	6 mW
[94][95] **(2006)**	Spectrum Filtering	0.13 µm InP-HEMT	0.8 V	----	0.5 nsec	Multicycle	24 – 29 GHz	----	620 mW

[Reference] (year)	Technique / Method	Technology / Process	V_{p-p}(V)	Efficiency	Pulse width (ns)	Pulse Type	Frequency Band	PRF	Power Consumption
[96] **(2017)**	Spectrum filtering / Derivative circuit	0.18 µm CMOS	1.2 V	----	1 nsec	Monocycle	0-1 GHz	200 MHz	1 mW
[57] **(2009)**	Spectrum Filtering / Derivative circuit	HBT	7.5 - 8.8 V	----	0.4 – 1 nsec	Monocycle	----	----	120 mW
[68] **(2014)**	Switching oscillator	0.13 µm CMOS	0.2 - 0.3 V	----	2 nsec	Multicycle	3-10 GHz	250 MHz	3.25 mW
[97] **(2009)**	Switching oscillator	0.18 µm CMOS	4.9 V	----	1 nsec	Multicycle	3.3 – 5.3 GHz	2 MHz	----
[67] **(2009)**	Switching oscillator	0.18 µm CMOS	673 mV	----	0.5 nsec	Multicycle	6 -10 GHz	50 MHz	1.38 mW
[65] **(2008)**	Switching oscillator	0.18 µm CMOS	160 mV	----	3.5 nsec	Multicycle	3-5 GHz	100 MHz	1.68 mW
[98] **(2009)**	Up Conversion	0.25 µm BiCMOS	0.2 V	----	----	Multicycle	7-8.5 GHz	60 MHz	413 mW
[66] **(2008)**	Up Conversion	0.18 µm CMOS	$7.2\ V^{100\Omega}$ $5.1\ V^{50\Omega}$	10.5%	1.2 nsec	Multicycle	3 - 5 GHz	1 MHz	0.8 mW
[62] **(2006)**	Up Conversion	0.18 µm BiCMOS	208 mV	----	2.4 nsec	Multicycle	5.1 – 5.6 GHz	100 MHz	31.3 mW
[99][100] **(2013)**	Up Conversion	0.25 µm BiCMOS	0.7 V	----	1 nsec	Multicycle	6.25 - 8.25GHz	56.64 MHz	43 mW
[101] **(2012)**	Up Conversion	0.25 µm BiCMOS	0.13 mV	----	2 nsec	Multicycle	7.75-8.25 GHz	499.2 MHz	130 mW
[102] **(2011)**	Up Conversion	SiGe 0.8 µm HBT	0.36 V	----	400 psec	Multicycle	5 – 9 GHz	100 MHz	6 mW
[102] **(2011)**	Up Conversion	SiGe 0.8 µm HBT	0.5 V	----	2 nsec	Multicycle	6.7 – 7.3 GHz	300 MHz	10 mW

2.3 Beamforming Transmitter Array

The on-chip generation of high-peak IR-UWB pulses is limited by the breakdown voltage of the transistor junctions. Therefore, as projected in Section-1.2, the beamforming technique was chosen for further amplification of the transmitted IR-UWB pulse in the steered direction. The beamforming technique enables transmitted pulses for spatially constructive interference in the steered direction and ultimately improves the output peak power. Beamforming not only improves the output peak power, but it comes with other advantages, which can improve the overall system performance. In this thesis, a multi-beam beamforming transmitter array utilizing the GDOP techniques for precise positioning application is projected. In this section, a brief overview of the beamforming transmitter array architecture is discussed. It is generally true that beamforming increases the size of the transmitter tag as well as it makes the system expensive. Therefore, one has to trade-off between the system's performance, cost, and size of the transmitter array. In addition, the power level should be under the regulated spectrum limit as explained in Section 2.1.5. The maximum permissible range and corresponding peak power limit should follow the FCC regulation limits. The details are provided in Section 2.1.5.

There are several architectures of beamforming transmitters published in the literature and are broadly divided into four major categories. In the first category, a simple introduction of a passive phase shifter to the RF signal path is done. In the second, implementation of a phase shifter in the intermediate frequency (IF) signal path is carried out. In the third, a digital phase shifter in the local oscillator's signal path is introduced. Finally, in the fourth, a true time delay element in the signal path flow is placed at the baseband digital data pulse.

2.3.1 Phase Shift to RF Signal

The simplest way is to insert a phase shifter in a separate RF path to introduce the desired path delay before the antenna. A typical block diagram representation is shown in Figure 2.12. The realization of phase shifter can be done by the passive phase shifter. In [103], 4×4 butler matrix BFN configuration and 8×8 Rotman lens BFN configuration are presented for RF beamforming network.

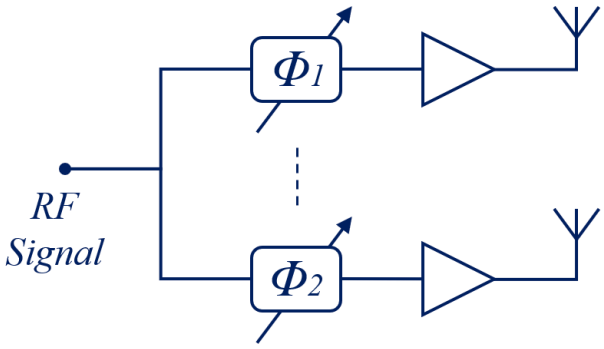

Figure 2.12. Typical beamforming transmitter architectures for RF phase shifter [104]

This method minimizes the number of RF building blocks by sharing one IR-UWB pulse generator by different paths. However, it is not appropriate because of high insertion loss into the passive components and takes a lot of space. This makes the overall transmitter size bulky. It is also not possible to navigate the beam electronically with the precise steering angle. In order to change the steering angle precisely, we need to rotate the entire antenna array mechanically. More importantly, it is difficult to maintain the same length in a signal distribution network hence contributing to different phase shift in each path. The phase difference is critical for beamforming system, especially for fast-time sync system.

2.3.2 Phase Shifter for IF Signal

In this technique, a phase shifter is used to provide the desired phase shift to the corresponding intermediate frequency (IF) signal path. Due to relatively low frequency, the designing of phase shifter becomes an easy task and is also less sensitive to the parasitic. The typical architecture is shown in Figure 2.13.

This design effectively minimizes the losses due to the passive component and makes the system smaller as compared to the passive network. However, poor linearity is the main issue with this type of architecture. The linearity issue becomes worse for high-amplitude signals as in this case. More importantly, the design of the proposed IR-UWB transmitter in this thesis is free from use of an oscillator [Section-3.2.] and hence, this technique cannot be adopted.

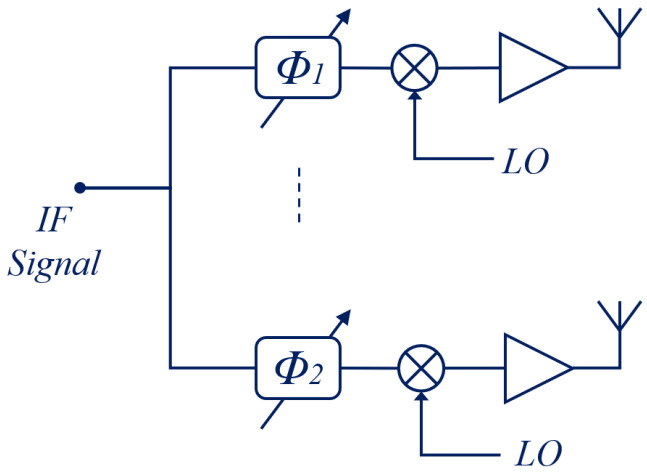

Figure 2.13. Typical beamforming architecture for the *IF* phase shift [104]

2.3.3 LO phase shifter

The local oscillator (LO) phase shifter technique implements a phase shifter to the signal path of a local oscillator. The block diagram representation of the technique is shown in Figure 2.14. The LO phase shifter scheme is suitable for narrowband beamforming. However, this is

not a good choice for beamforming of ultrawide-bandwidth signals. The dispersion of the signal causes signal distortion. In addition to this, the design of the proposed IR-UWB transmitter in this thesis is free from use of an oscillator [Section-3.2.]. Hence, this cannot be employed for getting delayed UWB pulse. The oscillator free design has been adopted for the proposed IR-UWB transmitter to minimize power consumption.

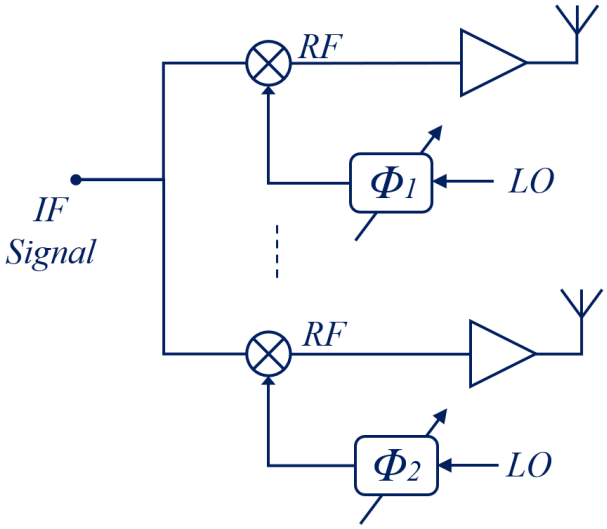

Figure 2.14. A typical beamforming transmitter architecture for *LO* phase shift [104]

2.3.4 True Time Digital Delay

The true-time digital delay concept is most appropriate for ultrawide-band beamforming. Since, the IR-UWB pulse generation takes a digital pulse as input and at the falling edge of the digital pulse, it generates an IR-UWB pulse as explained in the Section-3.2. A variable true-time digital delay element can be used to get the required delay to the baseband digital pulse. This technique also gives an electronic control over the true time delay elements, which allows steering of the beam in a particular direction. There are several delay element based architectures suggested in the literature [50], [104], [105]. Some of the architecture employed at baseband digital pulse to give equal relative delays between two consecutive paths are shown

in Figure 2.15. The architecture shown in Figure 2.15(a) is using only two different true-time digital delay elements (T_1 and T_2) with a variable delay control pin. These delay elements are configured as the Vernier delay cell concept to get the relative delay. The delay between two consecutive lines will always be ($\Delta T = T_2 - T_1$). This architecture has the advantage of a smaller number of control lines to calibrate the delay elements. However, the total number of delay elements is very high. The architecture has high power-consumption due to multiple delay elements.

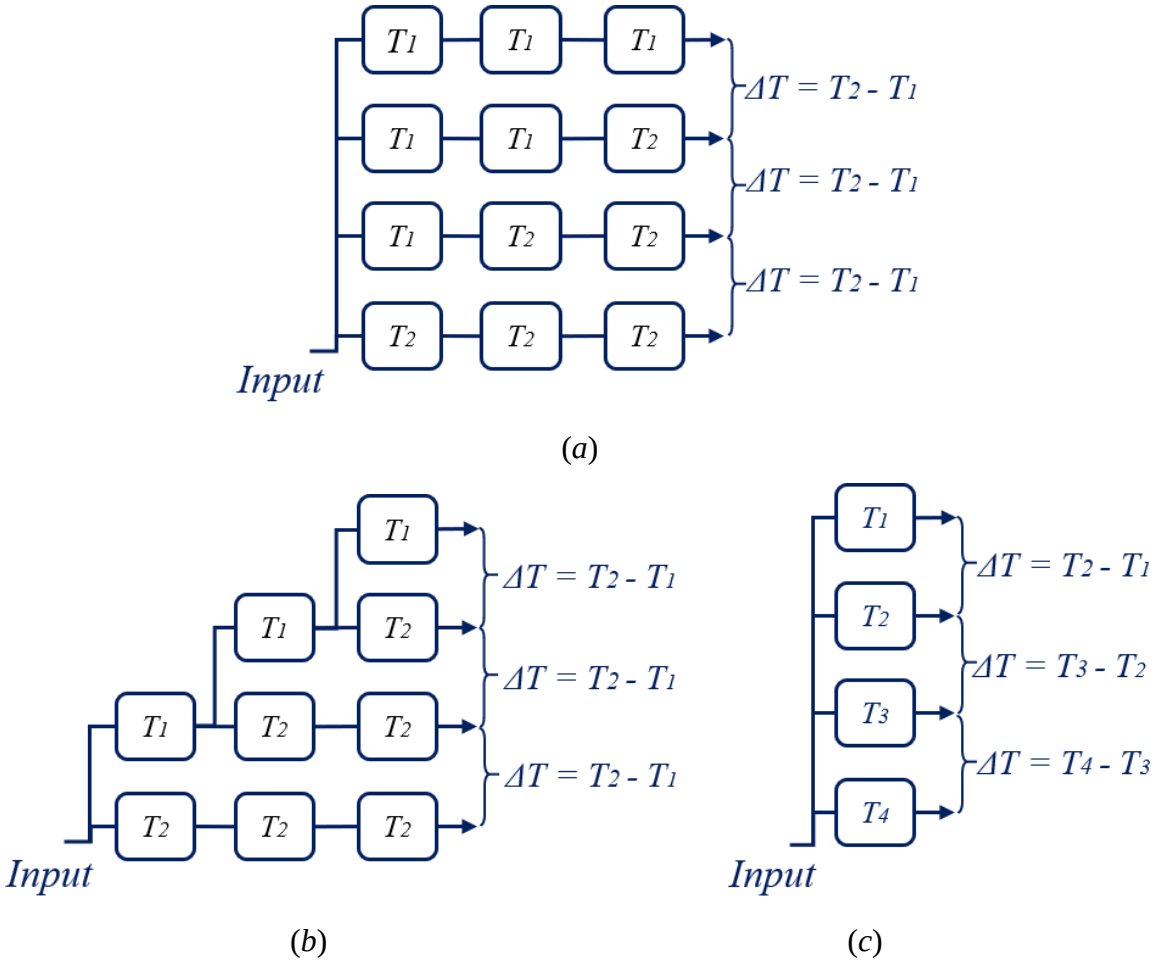

Figure 2.15 The true-time delay-based architecture at baseband for beamforming **(*a*)** basic Vernier delay line **(*b*)** improved Vernier delay line concept **(*c*)** relative delay line concept [104]

In order to minimize the number of delay cells in the configuration, an improved Vernier delay line design is shown in Figure 2.15(b). However, the total number of digitally controlled delay cells is still high. The architecture of the relative delay line concept is shown in Figure 2.15(c), which is less complex as compared to Vernier delay line architecture. The number of digitally controlled delay cells is significantly reduced in the relative delay line architecture. The consecutive delay in the case of four delay elements is given by $\Delta T = T_2 - T_1 = T_3 - T_2 = T_4 - T_3$, which gives the flexibility to change the delay between the consecutive transmitting elements. This flexibility will be used for another non-linear array optimization and beam steering as discussed in Chapter – 5. The minimization of the number of delay cells improves power-saving and makes the configuration power efficient. Hence, the relative delay architecture is chosen for the implementation of IR-UWB beamforming in this thesis. Some of the key requirements for the implementation of electronically control true-time delay concept are stated as follow [50], [106],

- The relative time spatial delay between adjacent antenna elements should be a fraction of the total pulse width T_p of the IR-UWB pulse.
- For an electronically controlled beam steering system, the true-time delay elements (steering delay) should be controlled variable to get the desired steering angle.
- Timing jitter and deviation of true-time delay elements should be minimum.

There are several published literature that uses a similar delay-based beamformer for the IR-UWB transmitter array [50], [104], [106], [107]. A similar concept has also been implemented at the receiver end [15], [108]. The reported works typically focus on a single beam array. However, there is insufficient research work done on simultaneous multi-beam IR-UWB transmitter array, which is critical for getting accurate positioning information inside the densely cluttered environment [109], [110]. The proposed beamforming system effectively

improves the directional peak-power level and produces multiple beams in desirable directions, which helps to reduced GDOP value, determine the initial orientation of the tag and improve the positioning accuracy, as explained in Chapter-4.

2.4 Collaborative Beamforming Virtual Array

The beamwidth of the practically viable transmitter array [usually 0.5 *m* length] operating in the 3-5 *GHz* frequency range is not appropriate for higher resolution through-the-wall imaging or long-range cluster-to-cluster directional positioning application. In order to get an arbitrary narrow beamwidth, the array length should be large enough, which is mechanically unstable and practically not feasible. Therefore, a collaborative beamforming virtual array is proposed for further improvement in peak-power level as well as higher imaging resolution of a radar sensor network and cluster-to-cluster directional positioning application. In addition, a single beam radiation pattern collaborative array inherently improves the dynamic resolution as compared to Omni-directional system. However, the static resolution will be the same as the omnidirectional system.

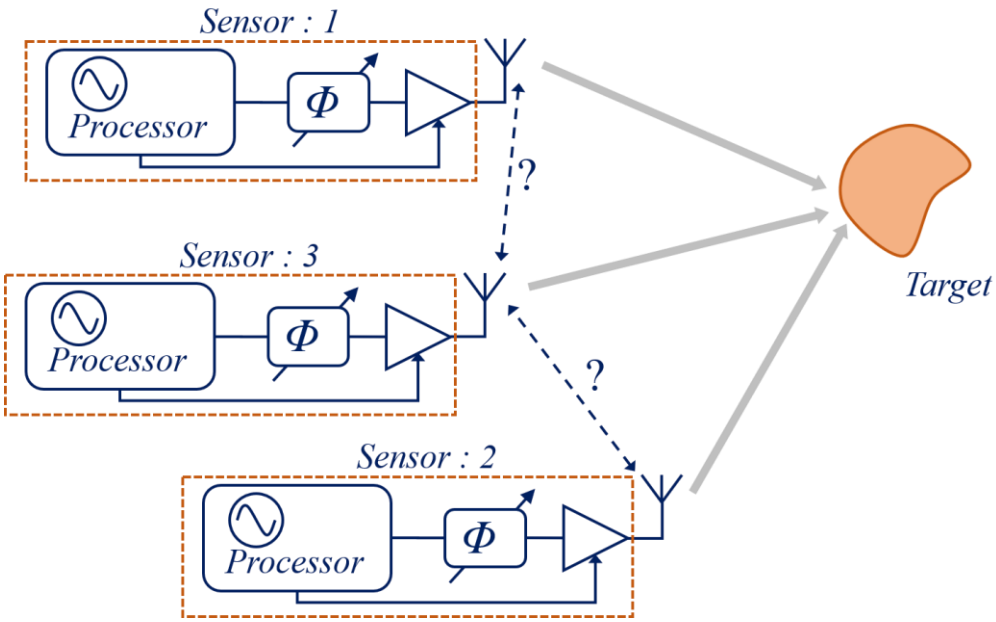

Figure 2.16. The block diagram representation of a collaborative beamforming virtual array system [111].

The block diagram representation of collaborative beamforming virtual array is shown in Figure 2.16. In the collaborative beamforming, few nodes within the WSN communicate

together collaboratively and make the desired formation to point a narrow beam towards the target [112]–[115]. The radar sensors utilize peer-to-peer ranging while forming a collaborative array. The peer-to-peer ranging is highly accurate for IR-UWB system, which is adequate for a collaborative array. The target for collaborative array could be hidden objects or behind the wall or a fairly far operative cluster of nodes. The mentioned applications principally need a steerable single narrow beam-pattern with significantly high peak output power in the direction of transmission. A single sensor node in the wireless sensor network (WSN) with an omnidirectional radiation pattern is not able to complete the task. In order to satisfy the requirement, collaborative beamforming is suitable. However, producing a single transmitting beam without grating lobes for an array with an electrically large separation between the transmitting elements is a challenging task [116]. The grating lobes disappear in the case of mono-cycle IR-UWB pulse or 2nd order Gaussian derivative [117], while the multi-cycle IR-UWB pulse produces multiple dominant lobes [116], as explained in Chapter 4. However, multi-cycle IR-UWB pulse is a better choice over mono-cycle pulse due to the FCC spectrum mask limit constraint and inefficiency of the antenna at lower center frequency [53].

The state-of-the-art related to IR-UWB beamforming can be found in [15], [118]–[120]. However, most of these published papers used a mono-cycle pulse, which effectively reduced the grating lobes radiation [118]–[120]. Some of the papers used a multi-cycle pulse with separation between the transmitting nodes less than a wavelength, which also minimizes the grating lobes [15]. The multi-cycle IR-UWB beamforming is still not explored significantly for collaborative transmitter array applications, where the sensor nodes separation will be in the order of several wavelengths. Nevertheless, it is considered important for the long-range applications, through-the-wall collaborative imaging, mobile robot formation control such as

drones operating collaboratively to send the signals in a certain direction etc. [111], [113], [115], [121]–[123].

The grating lobe reduction in the beam-pattern could be made possible by two techniques. First by optimizing the amplitude of each transmitting pulses, which will superimpose each other to produce minimum radiation in the grating lobes direction. However, optimizing the amplitude of each transmitting pulse will also significantly reduce the absolute radiation in the main transmitting beam. The second technique is to optimize the separation between the nodes such that the transmitted pulses superimpose constructively only in the steer direction and destructively otherwise. This way of optimizing the collaborative array will produce maximum possible radiation intensity in the steered direction. Therefore, in this thesis, the array spacing optimization is adopted for a single beam radiation pattern collaborative array.

It is important to note that collaborative beamforming in WSN has several challenges. Researchers have divided the problem into the following four major categories for independent research. These research categories are a) beam pattern synthesis and analysis, b) power and lifetime optimization, c) sensor nodes synchronization and d) WSN prototypes for collaborative beamforming [111]. In this thesis, the main focus is on the time-domain beam pattern synthesis and analysis in the case of a multi-cycle Gaussian-shaped IR-UWB pulse for collaborative beamforming. In addition, a prototype for beam-pattern measurements is developed for the proof of concept. The details of the proposed algorithm for collaborative beamforming and corresponding single beam radiation pattern synthesis is provided in Chapter-5.

2.5 Commercial IR-UWB Systems

There are several commercially available off-the-shelf products based on IR-UWB technology in the market. Some of them are studied and compared on the basis of the device's characteristics. The comparison is tabulated in Table 2.2. This study reflects mainly the hardware capabilities of the devices. For this study, the author mainly focuses on the product, which is compliant with the unlicensed FCC spectrum regulation limit.

Table 2.2. Comparison between different commercially available IR-UWB systems

		Manufacturer			
		Decawave Limited	**Zebra Technology**	**Time Domain Technology**	**Ubisense Technology**
Characteristic	**Product Name**	DW1000	Dart UWB	PulseON440 / PulseON410	9000IP / 7000IP
	Maximum Range (m)	290 m	200 m	350 m	160 m
	Localization Accuracy	10 cm	30	2.1 cm	15 cm
	Output power	5 dBm	NA	-14.5dBm to 0.7dBm (*power amplifier)	NA
	Frequency Range	3.5 GHz to 6.5 GHz	NA	3.1 GHz to 5.1 GHz	6 GHz to 8 GHz
	Bandwidth (BW)	500 MHz to 1 GHz (6 channel)	NA	1.4 GHz (*multi-channel)	NA
	Power Consumption	112 mW to 270 mW	NA	~1.8 watt	NA
	PRF (MHz)	16 MHz / 64 MHz	NA	10 MHz	NA
Application		Ranging / Data Communication	Ranging	Ranging / Data communication	Ranging

The Ubisens Technology provides series 9000IP and series 7000IP, which is a real-time detection tag that is characterized by its compact yet durable design. This device is specially designed to be installed into the assets allowing them to be pinpointed in real-time. It is commonly used in industrial areas where unfavourable conditions thrive. The industrial tag possesses a dimension of 71mm x 64mm x 47mm. The ubisense tag module research package is a real-time location system that can be used to track and locate assets and personnel to a three-dimensional accuracy of 15 *cm* in real-time. It utilizes the Time-Difference-of-Arrival (TDoA) and Angle-of-Arrival (AoA) techniques, which ensure both high accuracy and reliability of operation in challenging environments.

The Time Domain Technology released mainly two UWB products. The first product named PulsON 410 (P410) UWB module, which is a fully coherent, short-range radar that packs 1.4 GHz of RF bandwidth in a small, low cost, low power device. The second product is more advanced than earlier, which is PulsON 440(P440). The P440 module is a fully coherent UWB transceiver driven by FIFE, which combines two existing semiconductor chips into one chip lowering cost, reducing the power consumption, and physical size by half. The P440 uses Two-Way Time-of-Flight (TW-TOF) to achieve an accuracy of 2 cm at the rate up to 125 Hz. In addition to this, data communication is also supported by the same module. The UWB emissions are compliant with both the United States Federal Communications Commission (FCC) Part 15 regulations and the European Union ETSI EN 302 065 standard masks.

The Zebra Technology produces multiple devices based on UWB technology. The DART WAND module is a small table-top device, which can be located in the estimated range of less than 100 m. It can be easily configured using Zebra's dart wand application through a USB port. The DART TAGS are used to attach with assets or personnel to monitor and track their real-time location. The ranging limit is 200 m with an estimated line-of-sight accuracy of 30 cm.

The battery life of this device is very good, up to 7 years at 1 Hz blink rate. The DART SENSOR detects UWB pulses emitted by dart tags and provides asset visibility. The DART HUB is an intuitive and cost-effective product, which run zebra's advanced UWB RTLS, capable of delivering thousands of tags (high throughput) blinks per second at up to 30 cm accuracy.

The Decawave Limited manufactured DW1000, which is a fully integrated low power, single-chip CMOS radio transceiver IC compliant with the IEEE 802.15.4-2011 UWB standard. The DW1000 enables a precision of 10 cm indoors positioning, high data rate communications up to 6.8 Mb/s, and has an excellent communications range of up to 300 m. The DWM1000 module is optimized for indoor precision location and data communications for RTLS and WSN. The major advantage of Decawave product is low cost due to a fully integrated module.

Chapter – 3

IR-UWB Pulse Generator: Circuit Design and Optimization

This chapter discusses the design and implementation of the energy-efficient high peak power IR-UWB pulse generator. An in-depth circuital analysis of the energy-efficient high peak power IR-UWB pulse generator MMIC design using 2 μm GaAs HBT technology is presented. A trade-off between output peak power level and the frequency of operation is discussed. The proposed circuit is optimized for the highest possible output peak-power in the 3-5 GHz UWB band for ranging and radar application. The presented IR-UWB pulse former makes use of the cascode HBT configuration, which effectively improves the design for significantly higher output voltage swing as well as it reduces the total power consumption. The effect of coupling capacitors on the amplification factor of the pulse former stages and the impedance profile of the distributed transmission line are discussed in detail. The temperature-dependent parasitic component in the proposed circuit is studied. The effect of the parasitic on the transient behaviour of the proposed IR-UWB pulse generator is analyzed, which is important for IR-UWB beamforming applications. The required mathematical model for parasitic effects is derived and explained. Finally, the comparison of the fabricated IR-UWB pulse generator with the currently available published work is provided.

3.1 Introduction

The generation of IR-UWB pulse can be done by various methods as explained in Section-2.2. The shape of an IR-UWB pulse could be of numerous types, which can be broadly classified as a monocycle and a multicycle. The monocycle pulse generation is generally referred to as carrier-less IR-UWB pulse such as Rectangular monocycle, Rayleigh monocycle, Laplacian monocycle, Gaussian monocycle, Gaussian doublet, etc. The monocycle pulse is inherently useful for the lower band (less than 2 *GHz*) of the UWB spectrum. In addition, the inefficiency of an antenna at lower frequency is also an issue [124]. The multicycle UWB pulse on the other hand fully utilizes the spectrum in the upper-frequency bands as well as gives the flexibility to choose the center frequency for multi-channel communication. However, the shape of envelope is important to improve spectral efficiency and reduce any out-of-band emissions [125]. The ideal shape of the envelope is a sinc function, which has theoretically 100% spectral efficiency and 0% out-of-band emission [125]. However, generating a sinc enveloped multi-cycle IR-UWB pulse is difficult and the circuit complexity of the sinc pulse generator is relatively high.

Three easily achievable envelop shapes such as rectangular shaped, cosine-shaped, and bell-shaped Gaussian envelops in the time-domain and its frequency-domain characteristic are plotted in Figure 3.1. The rectangular-shaped envelope generation requires the simplest architecture to generate at baseband but results in the highest out-of-band emission with minor lobes, as shown in Figure 3.1. The cosine-shaped envelope generator is moderately easy to implement at baseband. In addition to this, the out-of-band emission is reasonably reduced, and the minor lobes are also reduced. The bell-shaped Gaussian envelope at baseband is comparatively difficult to generate and implement. However, it has out-of-band emission similar as compared to cosine shaped envelope but remarkably there are no side lobes present.

More importantly, the Gaussian-shaped envelope has the lowest time-bandwidth product among the three, which makes it a preferred choice and the most common envelope shape found in the literature [125].

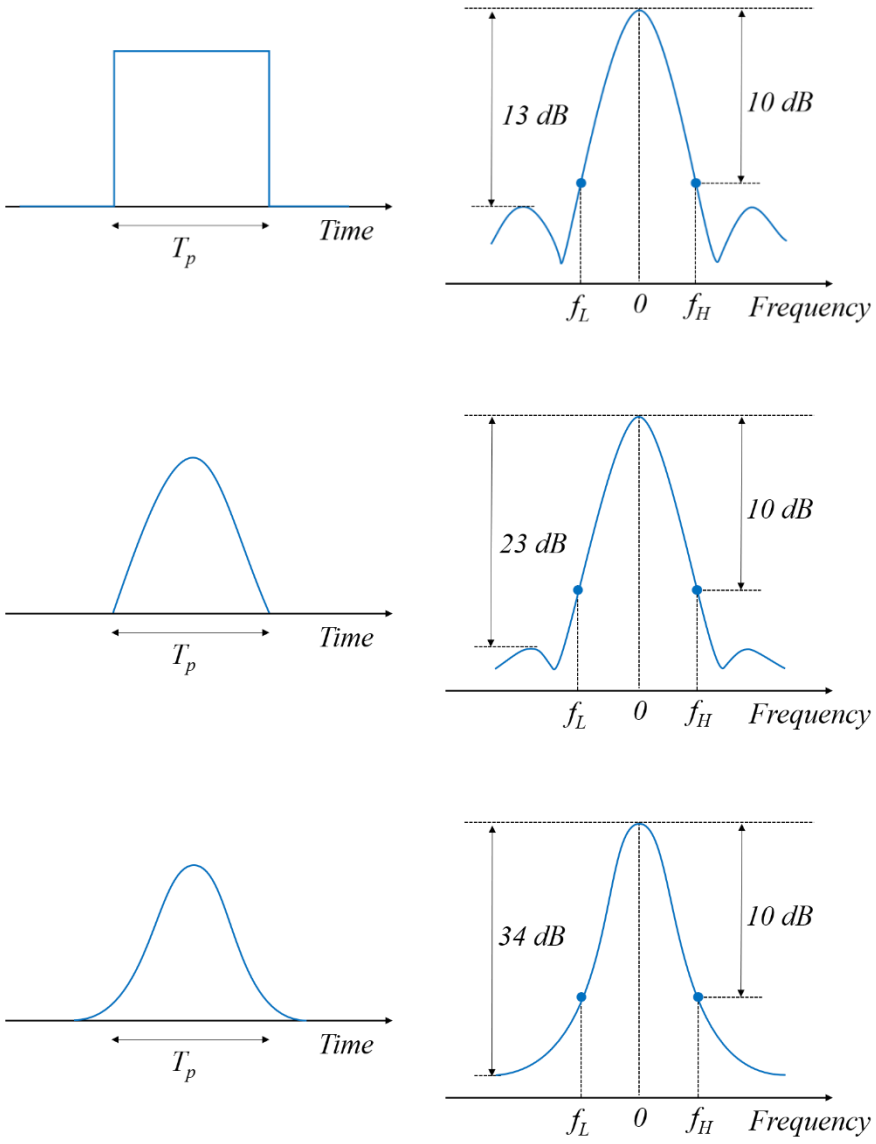

Figure 3.1. The time-domain baseband envelops and corresponding frequency domain representation. Rectangular shaped, cosine-shaped, and bell-shaped Gaussian envelops from top to down [2].

It is important to note that the smoother shape of the envelope has better performance parameters as compared to the sharp edge as shown in Figure 3.1. The Gaussian-shaped

envelope has the best characteristic among the three. However, it is difficult to achieve a precise Gaussian shaped envelope. Therefore, in this thesis, a Gaussian enveloped IR-UWB pulse is projected to achieve theoretically but practically in between Gaussian and cosine shaped envelope is achieved. A precisely Gaussian enveloped multicycle IR-UWB pulse with its frequency-domain characteristic is shown in Figure 3.1. The centre frequency can be easily tuned by changing the fundamental cycle time *"T"* as shown in Figure 3.1. This tuning can be used to tune the transmitter for multi-band communication. In addition to envelop mismatch, the carrier misalignment also arises side bands. Therefore, a pulse former should be able to minimize the carrier misalignment. In this thesis, the proposed pulse former used multiple sub-nanosecond impulse to construct a multi-cycle Gaussian shaped pulse, which principally eradicates the carrier misalignment problem. However, slight carrier misalignment may happen due to jitter in the generated sub-nanosecond impulse. Therefore, use of a Band Pass Filter (BPF) after Pulse Former stage will be wise to suppress the unwanted side bands.

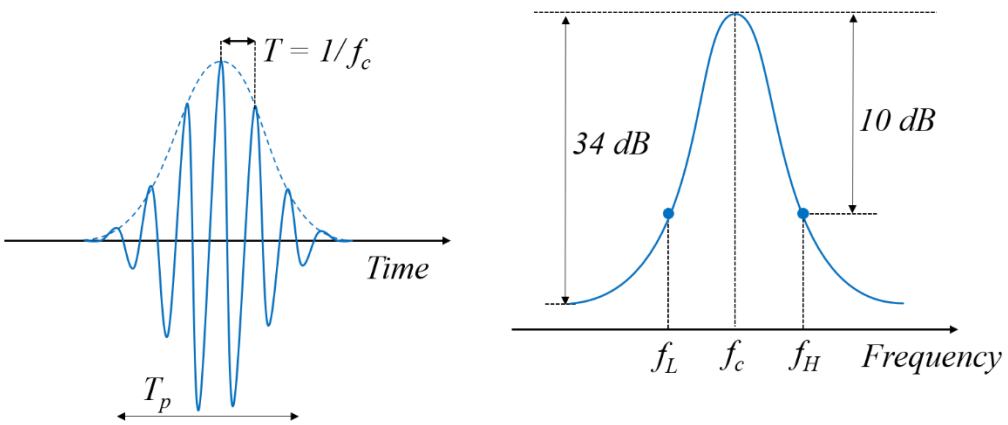

Figure 3.2. The time-domain multicycle Gaussian enveloped IR-UWB pulse and corresponding frequency-domain representation [2].

3.2 Proposed IR-UWB Pulse Generator

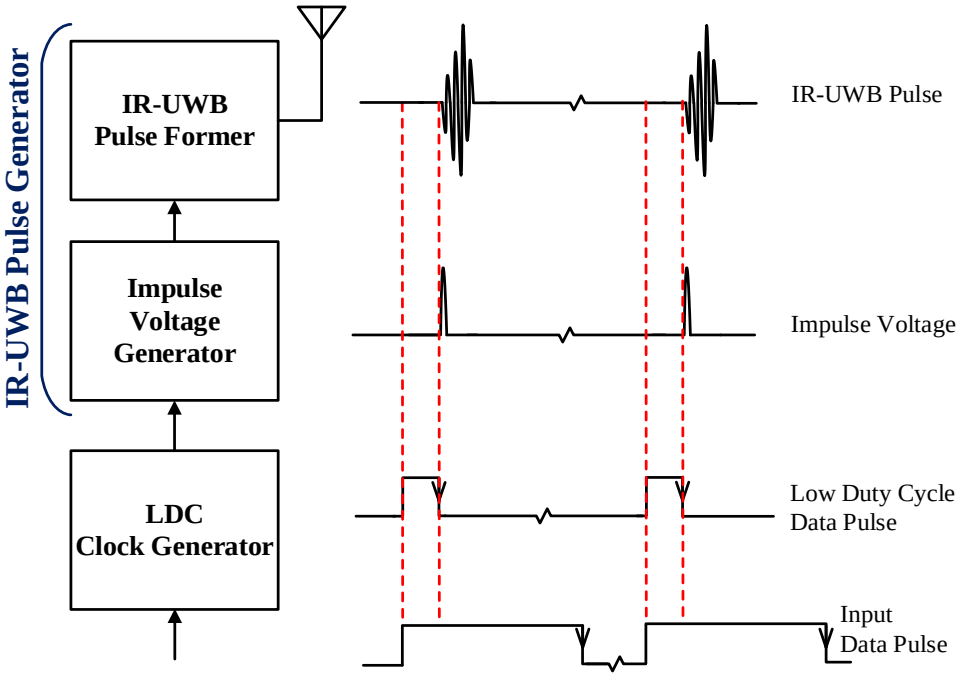

Figure 3.3. Block diagram of the proposed IR-UWB transmitter tag with a graphical illustration of IR-UWB pulse generation at each block.

The block diagram of the proposed IR-UWB transmitter tag and the generation of IR-UWB pulse is exemplified in Figure 3.3. The low duty cycle (*LDC*) digital clock generator block is intentionally opted to minimize the total power consumption and produce a sharp falling edge of the data pulse [9]. The implementation of the *LDC* block is done by the combination of digital logic gates. The *LDC* block took the digital data signal as an input and reduced the duty cycle of the data pulse.

The generation of the multi-cycle IR-UWB pulse is carried out through two different blocks on the MMIC. The first block is called the impulse voltage generator (*IG*), which generates a 7*V* output impulse voltage with a 90 *ps* full width at half maxima (FWHM). The impulse generator works on the principle of first fully charging and then abruptly discharging the base capacitance of HBT [93]. At the falling edge of the data pulse, the removal of space charge accumulation in the emitter region takes place. After removal of charge, the base current

quickly goes back to zero. The speed-up in the base current is then differentiated by an inductor at the collector terminal to get the sub-nanosecond impulse voltage.

In the second block of MMIC, a four-stage distributed network called the IR-UWB pulse former (*PF*) is designed and optimized to construct a gaussian IR-UWB pulse. The pulse former makes use of the generated impulse voltage from the impulse generator as an input. At each stage of the pulse former, signal scaling, time-shifting, and signal inversion are performed. Signal addition is then done at the output stage of pulse former to produce the desired gaussian-shaped multi-cycle IR-UWB pulse. For the time-shifting operation, off-chip transmission lines have been used between the pulse former stages. For signal inversion, a short-circuited stub has been used. A cascode pair configuration of the transistor is used for overcoming the transistor's junction breakdown issue, which significantly increases the output voltage swing range. In addition to this, the proposed cascode pair configuration also enables the high impedance path at the collector terminal of HBT, which draws less current from the biasing source and thus makes the design power efficient.

In this chapter, an improved design of distributed IR-UWB pulse generation is presented for significantly higher output voltage pulse without breaking-down of transistors. An in-depth circuital analysis of the proposed IR-UWB pulse generator is explicitly added. The ability to generate higher output peak power versus carrier frequency is discussed. The proposed circuit of the IR-UWB pulse generator is then optimized for the ranging and radar application in the 3-5 *GHz* UWB band. The effect of the coupling capacitor on the amplification factor and the impedance profile of the distributed pulse former network is explained in great detail. The proposed cascode HBT configuration to improve the breakdown voltage of HBT in the pulse former design is explained. The related simulation and analysis are performed to get the higher output voltage swing without the breakdown of HBT junction. The temperature-dependent

transient analysis of the proposed design is performed. The overall transfer function of the proposed design is deduced and explained. The total transient delay of the generated IR-UWB pulse due to temperature change is calculated and effect on the pulse forming network is discussed. In addition to this, the effect of jitter due to temperature change on the beamforming is discussed.

3.2.1 Impulse Voltage Generator

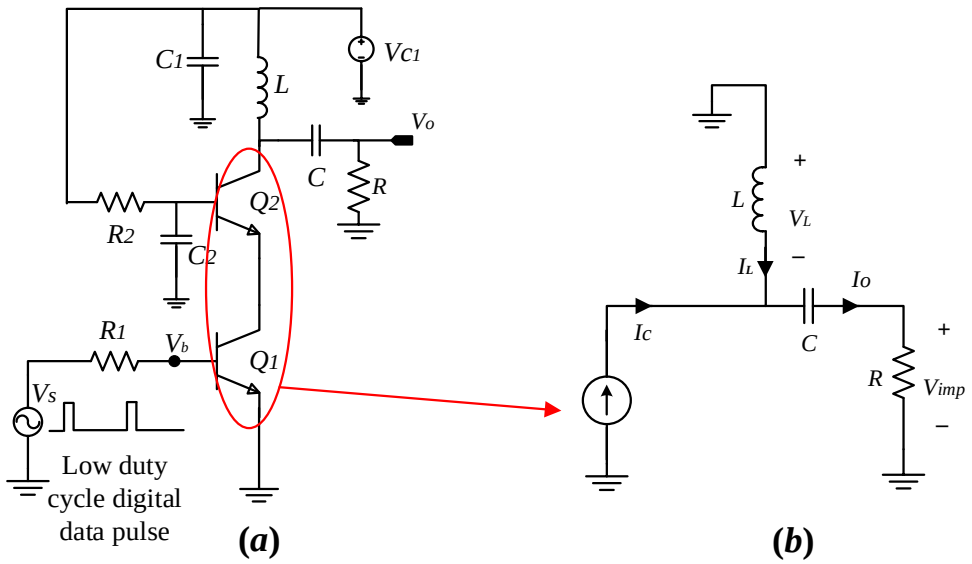

Figure 3.4. Schematic of (a) impulse voltage generator (*IG*) and (b) reduced small-signal model during the second step of discharging of *B-E* junction

$$I_C = \begin{cases} -I_m & ; t < 0 \\ \dfrac{I_m}{t_0} t - I_m & ; 0 \le t \le t_0 \\ 0 & ; > t_0 \end{cases} \qquad (3.1)$$

The schematic of the sub-nanosecond impulse voltage generator (*IG*) is shown in Figure 3.4(a) and reduced equivalent model is shown in Figure 3.4(b). The cascode HBT pair (Q_1 and Q_2) is used for achieving higher gain and large output impedance [126]. C_1 and C_2 are the RF

grounding capacitors. L is the off-chip inductor and V_{C1} is the biasing voltage of the impulse generator. The impulse generator works on the principle of first fully charging the input base emitter junction of HBT (drive Q_1 into the saturation region) and then abruptly discharging the base emitter junction of HBT (drive Q_1 into the cut-off region) [127], [128]. The change in state result in cutting off the collector current abruptly. This speed-up in the change of Q_1's collector current is buffered by Q_2 of the cascode HBT pair and then differentiated by an inductor at the collector terminal to obtain the sub-nanosecond impulse voltage.

At the falling edge of the data pulse (during discharging of *B*-*E* junction), the complete removal of stored charge takes place in two consecutive steps. In the first step, the base current slowly attended negative values to remove the stored charges. In this step, the HBT is still in saturation region until the slow removal of charge makes the voltage across the *B*-*E* junction equal to cut-off voltage. In the second step, the *B*-*E* junction becomes open-circuited. Hence, the collector current quickly goes back to zero. The speed-up in collector current of cascode HBT pair is then differentiated by an inductor L at the collector terminal to get the sub-nanosecond impulse voltage. It is important to note here that the removal of charge delays the *B*-*E* junction's turn-off process. The first step of charge removal quantifies as a transient delay of the IR-UWB pulse generation process. The transient delay depends on the quantity of stored charge across *B*-*E* capacitance. The second step of the charge removal is determined by the switching characteristic of transistors (HBT), which decide the rising edge of the generated impulse voltage. It eventually decides the time-width of the generated impulse voltage and the range of oscillation frequency of the generated IR-UWB pulse (discussed in section 3.2.2).

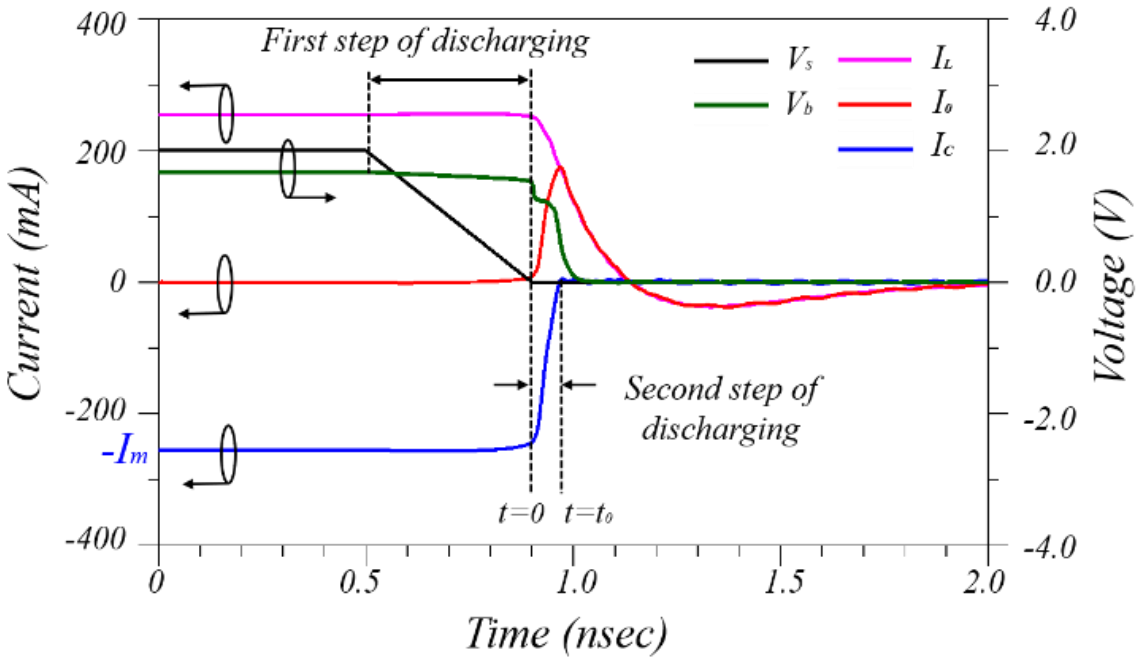

Figure 3.5. The Simulated source voltage V_s, base voltage V_b of transistor Q_1, collector current "I_c" of cascode pair, inductor current "I_L" and output current "I_0".

$$R\frac{dI_C}{dt} = \frac{dV_{imp}}{dt} + \frac{R}{L}V_{imp} + \frac{1}{LC}\int V_{imp}dt \tag{3.2}$$

$$V_{imp} = \frac{I_m L}{t_0}\left[1-\exp\left(-\tfrac{R}{L}t\right)\right] \qquad ; 0 \le t \le t_0 \tag{3.3}$$

$$V_{imp} = V_m \exp\left(-\tfrac{R}{2L}(t-t_0)\right)\left[\cos\omega(t-t_0) - \tfrac{R}{2L\omega}\sin\omega(t-t_0)\right]$$
$$\textit{where,} \qquad \omega = \sqrt{\tfrac{1}{LC} - \tfrac{R^2}{4L^2}} \qquad ; t > t_0 \tag{3.4}$$

To observe these effects, the simulated (using non-linear VBIC model of HBT) source voltage V_s, and base voltage V_b of transistor Q_1 is shown in Figure 3.5 along with the collector current "I_c" of cascode pair, inductor current "I_L" and output current "I_0". As shown in Figure 3.5, the input digital source voltage V_s goes to 0 from t = 0.5 *ns* resulting in charge removal

from the junction. This first step of discharging is quantified as a transient delay of the IR-UWB pulse generation process. When all the junction charges are withdrawn, the transistor changes state into cut-off. However, the collector current rate of change will depend on the load capacitances of Q_1. The combined output capacitance of Q_1 and input capacitance of Q_2 will set the second step of discharging, which decide the rising edge time of the generated impulse voltage. It eventually decides the time-width of the generated impulse voltage and the maximum oscillating frequency of the generated IR-UWB pulse (discussed in the sub-section 3.2.2).

In the second step of the charge removal process, the cascode pair is approximated as a ramp current source during the turn-off process due to its smaller parasitic capacitance and larger output impedance. As illustrated in Figure 3.5, the current during the saturation region is assumed to be $-I_m$ ($t < 0$), and 0 ($t > t_0$) during the cut-off region for modelling purpose, leading to (3.1) where t_0 is the switching time of the cascode pair. The current during the switching period ($0 < t < t_0$) is approximated as linear variation with a slope of I_m/t_0, as shown in Figure 3.5. The differential equation corresponding to the equivalent model of impulse generator is given in (3.2), which shows a relation between output voltage in terms of collector current I_C. The 2nd order differential equation shown in (3.2) corresponding to the small-signal model [Figure 3.4(b)] is solved for the approximated ramp current [equation (3.1)] with the initial condition $V_{imp(t=0)} = 0$. This gives the solution for the rising and falling edge of the generated output impulse voltage "V_{imp}". The deduced rising edge ($0 < t < t_0$) of the generated impulse voltage is given in (3.3) and falling edge ($t > t_0$) is shown in (3.4).

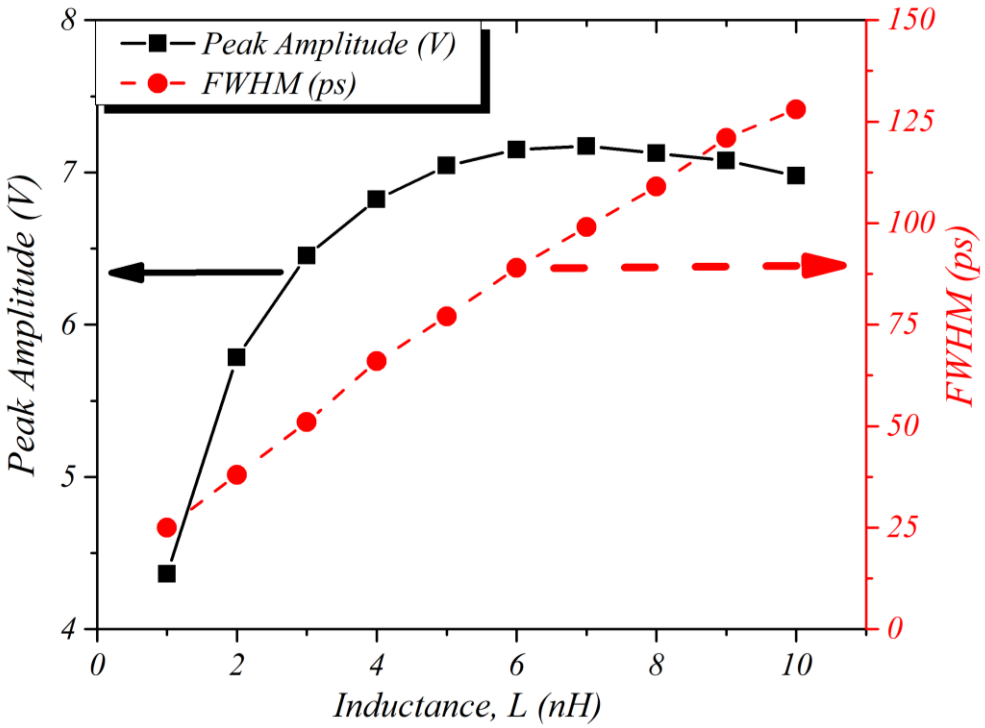

Figure 3.6. Study of peak amplitude and FWHM variation with the inductance value "*L*"

The amplitude and full width at half maxima (*FWHM*) of the generated impulse voltage "V_{imp}" can be controlled by varying inductance values [from (3.3) and (3.4)]. The plot of amplitude and *FWHM* versus inductance "*L*" is shown in Figure 3.6. The amplitude and FWHM of the impulse voltage decide the peak-to-peak voltage (V_{pp}) and the oscillating frequency of the generated IR-UWB pulse. The amplitude of V_{imp} increases exponentially and gets saturated with the increase in *L* and *FWHM* increases linearly with an increase in *L*. Hence, the inductance tuning can be used to optimize the proposed circuit for higher frequency band scaled up to millimeter-wave impulse radio radar applications. However, it is important to note that at a higher frequency of operation, $V_{p\text{-}p}$ will be greatly reduced. Hence, one has to consider a trade-off between frequency band and output peak power level using the design equation given in (3.3) and (3.4). In this thesis, the proposed circuit is optimized for the highest possible $V_{p\text{-}p}$ operating in the 3-5 *GHz* UWB frequency band.

3.2.2 IR-UWB Pulse Former

In the second block of MMIC, an *n*-stage distributed network called the pulse former (*PF*) is proposed and optimized to construct a Gaussian shaped multi-cycle IR-UWB pulse. The schematic of the *n*-stage pulse former is shown in Figure 3.7. The IR-UWB pulse generation principle consists of signal scaling (depicted by blocks A_1, A_2, ... A_n), time-shifting (depicted by τ_1) and signals inversion (depicted by τ_2) operation at each stage of the proposed pulse former.

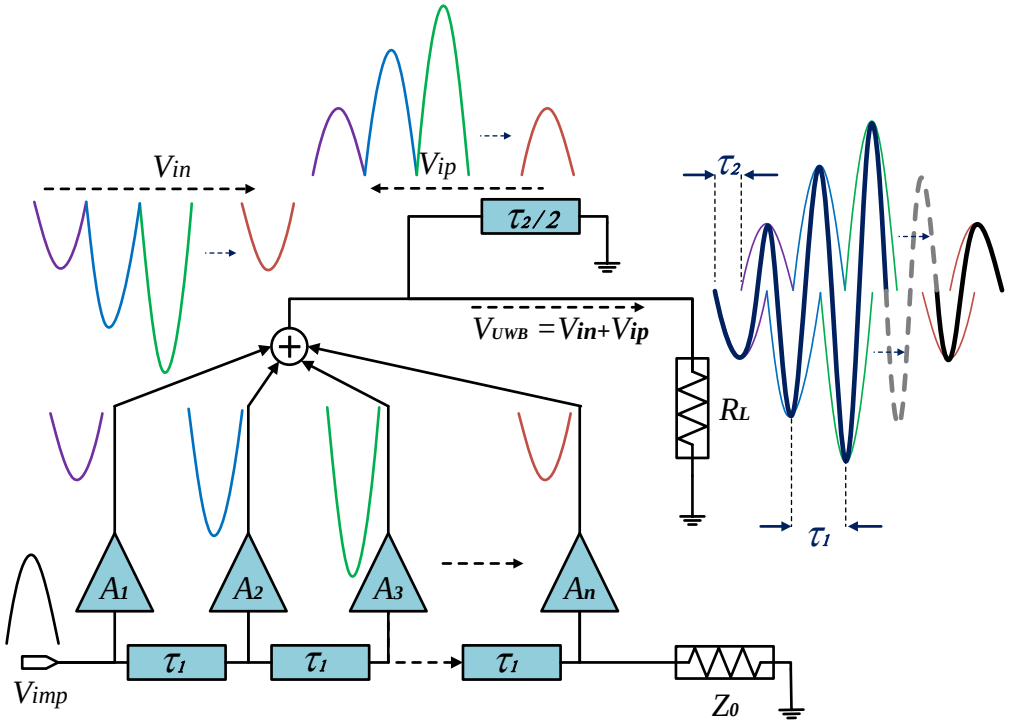

Figure 3.7. The Schematic of pulse former (*PF*) and graphical illustration of IR-UWB pulse waveform formation.

$$V_{UWB} = V_{in} + V_{ip} = \sum_{n=1}^{N} \begin{bmatrix} A_n V_{imp}\left\{t-(n-1)\tau_1\right\} + \\ A_n V_{imp}\left\{t-\tau_2-(n-1)\tau_1\right\} \end{bmatrix} \tag{3.5}$$

The signal scaling and time-shifting operation is an important parameter to decide the frequency characteristic of the generated IR-UWB pulse. The value of τ_1 (ideally equal to the

total pulse width of V_{imp}) decides the fundamental frequency provided that $\tau_2 = \tau_{1/2}$. The signal scaling decides the envelope of the pulse, which controls the frequency characteristic within the operating band. The time-shifted scaled signal and the corresponding inverted signal is added at the output stage of the pulse former to construct the IR-UWB pulse [9], [77], [86], [87]. The graphical illustration of IR-UWB pulse waveform generation is shown in Figure 3.7. The mathematical representation of IR-UWB pulse formation is given in (3.5). V_{in} and V_{ip} are the negative and positive impulse voltage, respectively, as shown in Figure 3.7. A_n is the scaling factor and V_{imp} is the generated impulse voltage [from (3.3) and (3.4)].

As depicted in Figure 3.7 and (3.5), the pulse-width "τ_1" of V_{imp} decides the oscillating frequency. The number of unit impulses used to construct the IR-UWB pulse determines the envelope pulse width and the frequency spectrum. In order to optimize the pulse generator for better performance in the 3-5 *GHz* band, four-cycle IR-UWB pulse is adopted based on the study reported in [9]. The Impulse Generator (*IG*) is optimized to generate a 7*V* impulse voltage with a ~240 *ps* full width at tenth maxima (FWTM). The generated impulse is used to generate four positive amplitude impulses "V_{in}" using four-stages of Pulse Former (*PF*). Similarly, four negative amplitude impulses "V_{ip}" are generated using the short circuit stub, as explained in Figure 3.7. In total, four positive impulses, and four negative impulses are used to construct the IR-UWB pulse. The total pulse width of the generated IR-UWB pulse is approximately 1 *ns*, which provides sufficient temporal resolution in the case of indoor positioning application. More importantly, the output V_{pp} is significantly improved for the optimized pulse generator.

The circuit diagram of the proposed IR-UWB pulse former is depicted in Figure 3.8. The time shifting is achieved by realizing a delay striplines. The delay-lines can be realized using integrated lumped capacitance and inductors. However, it is important to note that the inductor occupies a larger area on-chip for the frequency range 3-5 *GHz*. The chip area, especially for

GaAs wafer, is far expensive than Roger PCB area. In order to save the cost, the delay line is realized using a distributed transmission line (stripline). In addition, the distributed line also provides better phase noise as compared to discrete on-chip design.

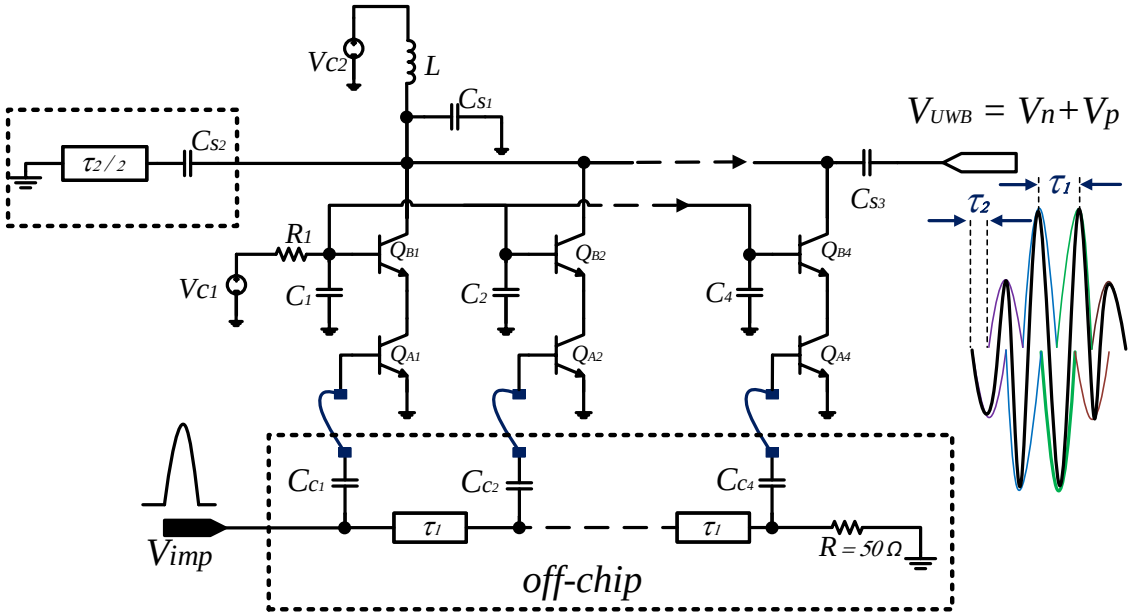

Figure 3.8. Circuit diagram of the proposed IR-UWB pulse former showing off-chip components within the dashed rectangle

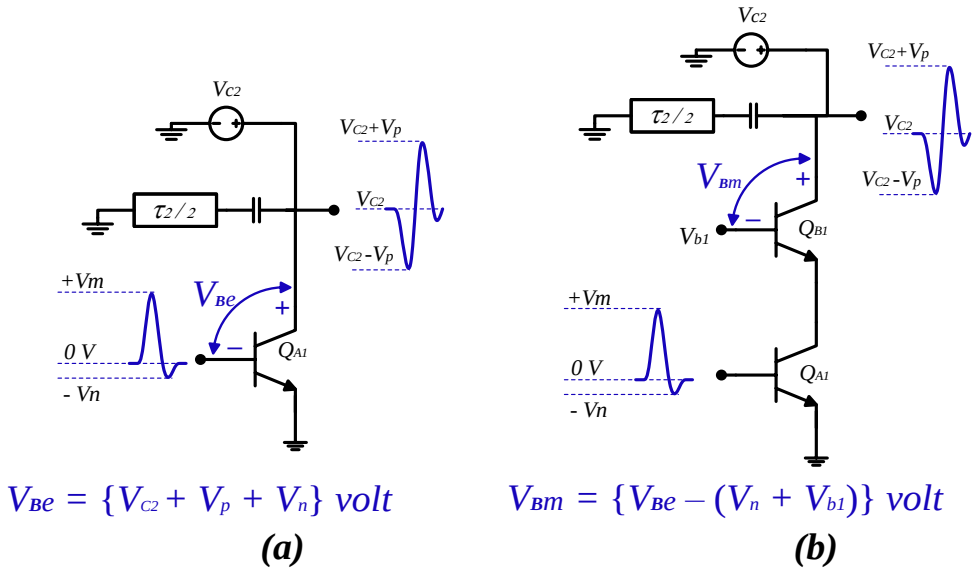

Figure 3.9. DC bias configuration of **(*a*)** earlier design and **(*b*)** improved design for the breakdown of transistor

The signal scaling of the impulse voltage is done by the cascode pair [Q_{An} and Q_{Bn} $(1 < n < 4)$] at each stage of the pulse former. The cascode pair configuration of the HBT alleviate the issue of the breakdown of the *B-C* junction for higher output voltage swing unlike in the earlier designs available in the literature [9], [86], [87]. The earlier designs used single transistor configuration (such as common-emitter) and directly fed the impulse voltage at the base terminal of the transistor as shown in Figure 3.9. In this case, the effective voltage drops "V_{Be}" across the base-collector terminal becomes more than the breakdown voltage. The impulse voltage attains negative value "$-V_n$" due to overshoot. Hence, the effective $V_{Be} = \{V_{C2} + V_p + V_n\}$ *volt* [In Figure 3.9(a)]. The proposed design uses cascode pair configuration and connects the base terminal of the HBT Q_{Bn} to a constant DC source by a passive resistor such that the voltage at the base terminal is "V_{b1}" as shown in Figure 3.9(b). The effective voltage drop across the base-collector terminal of the modified circuit becomes $V_{Bm} = \{V_{Be} - (V_n + V_{b1})\}$ *volt*. Hence, it effectively reduces the voltage drop by $(V_n + V_{b1})$ *volt*.

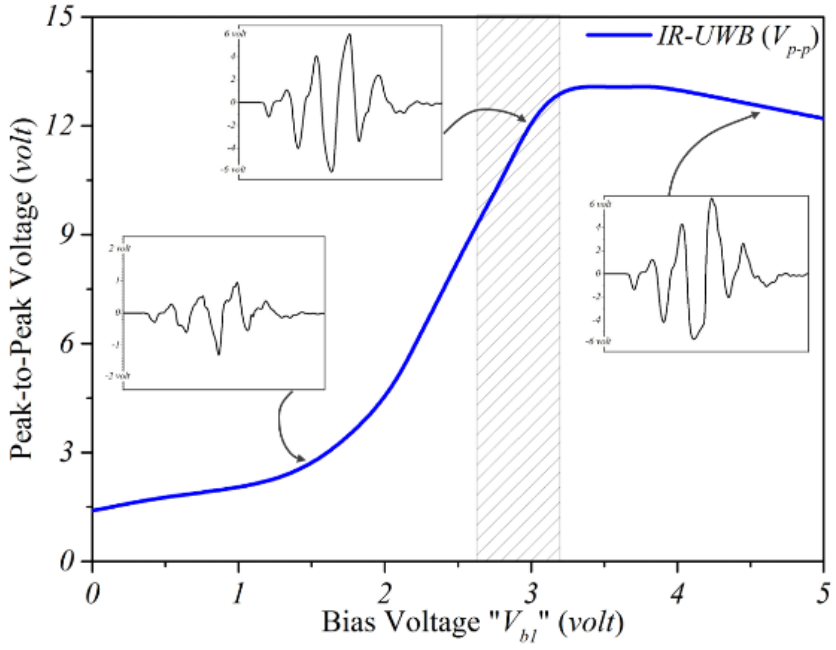

Figure 3.10. The simulated peak-to-peak voltage output of IR-UWB pulse with the bias voltage "V_{b1}" at the base terminal of Q_{Bn}

For the proposed design, various simulations have been performed with the variation of base bias V_{b1} and peak-to-peak voltage of the generated IR-UWB pulse is observed. The observed peak-to-peak voltage with the change in V_{b1} is plotted in Figure 3.10. For the lower V_{b1} the generated IR-UWB pulse has the lowest voltage swing. In addition, the pulse shape is also distorted [as shown in the inset of Figure 3.10.]. For the higher V_{b1}, the voltage-swing saturates. Nonetheless, it also distorts the pulse shape. The shaded area [in Figure 3.10.] is the proper bias voltage-range which gives pulse with optimal peak-to-peak voltage without distortion. The value of $V_{b1} = 3V$ [same as biasing source V_{C1} of *IG* in Figure 3.4(a).] is chosen after careful consideration. In this example, $V_n = 3\ V$ and $V_{b1} = 3\ V$, which gives the flexibility to increase the voltage swing [by ($3\ V + 3\ V = 6\ V$)] of the output IR-UWB voltage pulse without causing the breakdown of HBT.

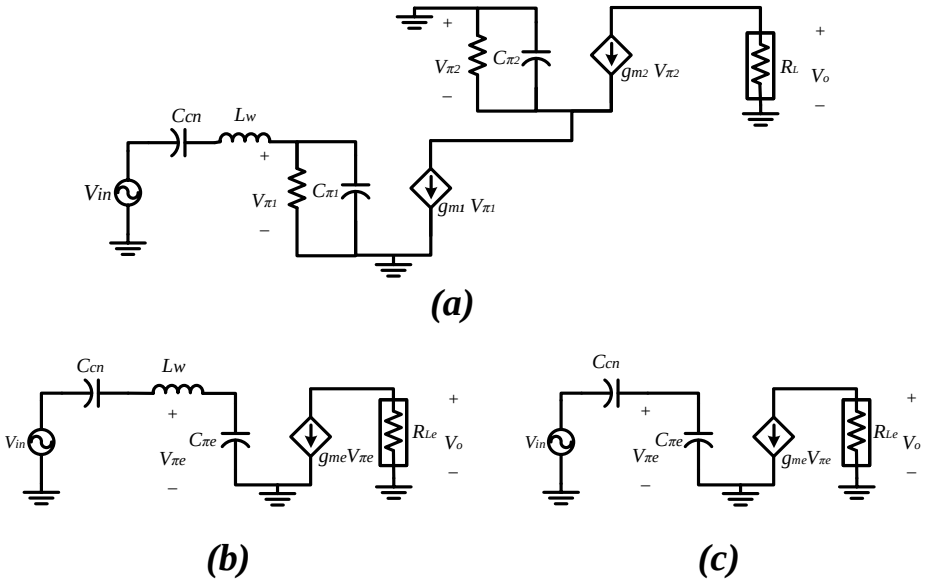

Figure 3.11. (*a*) The small-signal model of one stage of the proposed IR-UWB pulse former. The simplified small-signal model (*b*) with the effect of L_w (*c*) without the effect of L_w

In the next step, the gain of each stage has to be set precisely in order to achieve the smoother Gaussian envelope of the multi-cycle IR-UWB pulse as discussed in Section-3.1. The small-signal model of a single-stage pulse former is shown in Figure 3.11(a). The first HBT stage of

the cascode pair acted as a buffer and reduced the miller effect, which increases the operating bandwidth. However, the equivalent gain of a cascode HBT pair is almost the same as one HBT stage of common emitter's gain. Hence, for the gain calculation, the two HBT stage is reduced to one equivalent HBT stage. The simplified model of the equivalent HBT stage of the pulse former stage is shown in Figure 3.11(b). For high-frequency transient analysis, the effect of the input resistance "r_π" of the HBT is neglected. The effect of bond wire inductance "L_w" between the coupling capacitor C_{cn} $(1<n<4)$ and the base terminal of the HBT Q_{An} has been incorporated in the small-signal model in Figure 3.11(b). The gain of one stage is given in (3.6), where the term $\omega^2 C_{cn} C_{\pi e} L_w$ is due to "L_w" and is very small as compare to C_{cn} and $C_{\pi e}$. Hence, neglected in the final simplified circuit as shown in Figure 3.11(c).

$$A_n = \frac{V_0}{V_{in}} = -g_{me} R_{Le} \frac{C_{cn}}{C_{cn} + C_{\pi e} - \omega^2 C_{cn} C_{\pi e} L_w} \tag{3.6}$$

$$\frac{A_{(n+1)}}{A_n} = \exp(-\alpha l) \frac{C_{C(n+1)} \,/\!/\, C_{C(n+1)} + C_{\pi e}}{C_{Cn} \,/\!/\, C_{Cn} + C_{\pi e}} \tag{3.7}$$

The ratio of voltage gain of one stage of the pulse former to consecutive stage is given in (3.7), where the term A_n denotes the voltage gain of n^{th} stage, α denotes the attenuation constant of effective medium and l denotes the length of the off-chip stripline used for time-shifting operation between the pulse former stages. The shape of the IR-UWB pulse envelope depends on the amplification factor of each stage, which can be tuned by changing the values of Cc_n ($1 \leq n \leq 4$) using (3.7). However, the changing values of coupling capacitance Cc_n also results in

mismatched the characteristic impedance of the distributed transmission line between each stage of pulse former as shown in Figure 3.12(a).

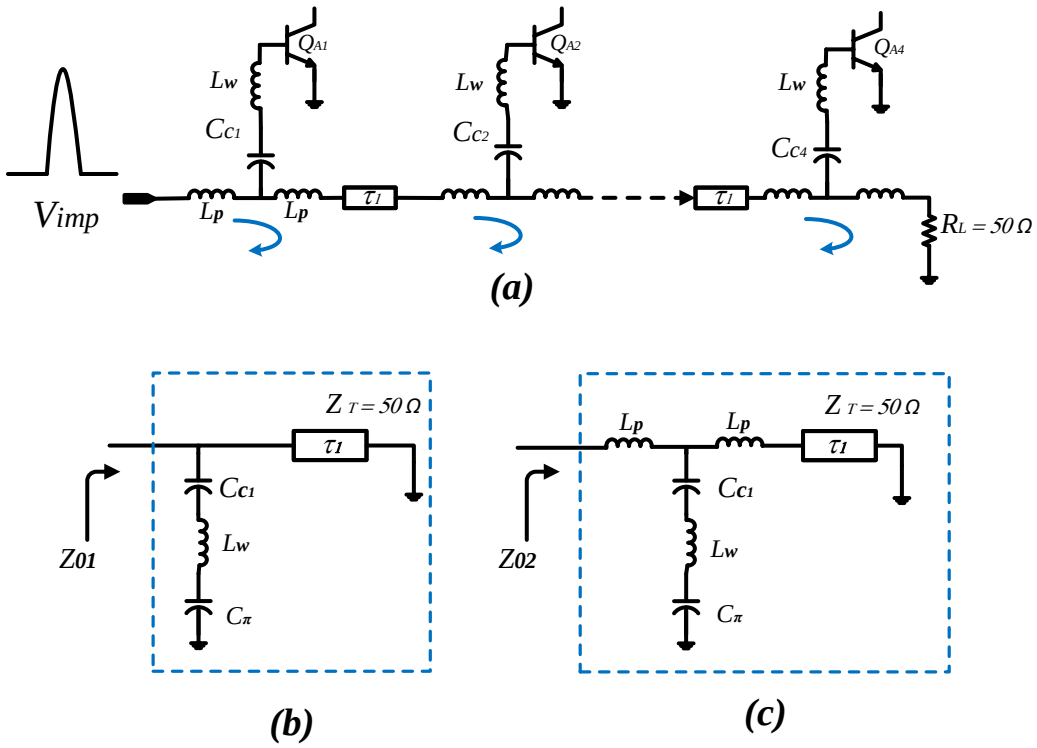

Figure 3.12. (*a*) The distributed transmission line in the proposed pulse former for time-shifting operation. Equivalent characteristic impedance **(*b*)** without the effect of parasitic inductance L_p **(*c*)** with the effect of parasitic inductance L_p

$$Z_{01} = \left(\frac{1}{j\omega C_{cn}} + \frac{1}{j\omega C_{\pi}} + j\omega L_w \right) \| \, Z_T = \left(\frac{1}{j\omega C_{eqv}} + j\omega L_w \right) \| \, Z_T \tag{3.8}$$

$$\left| Z_{01} \right| = \frac{Z_T \left(\frac{1}{\omega C_{eqv}} - \omega L_w \right)^2}{\left(\frac{1}{\omega C_{eqv}} - \omega L_w \right)^2 + Z_T^2} \tag{3.9}$$

$$Z_{02} = j\omega L_p + \left(\frac{1}{j\omega C_{cn}} + \frac{1}{j\omega C_{\pi}} + j\omega L_w \right) \Big\| \left(j\omega L_p + Z_T \right)$$
$$= j\omega L_p + \left(\frac{1}{j\omega C_{eqv}} + j\omega L_w \right) \Big\| \left(j\omega L_p + Z_T \right) \tag{3.10}$$

$$\left| Z_{02} \right| = \frac{Z_T \left(\frac{1}{\omega C_{eqv}} \right)^2}{\left(\frac{1}{\omega C_{eqv}} - \omega L_p \right)^2 + Z_T^2} \tag{3.11}$$

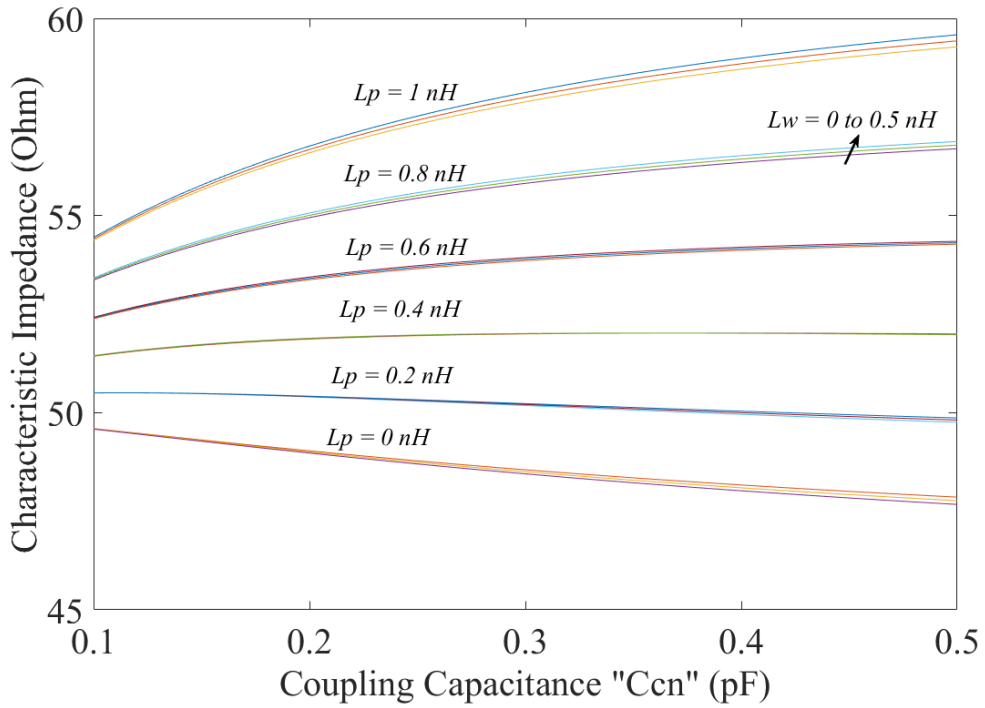

Figure 3.13. Variation of the characteristic impedance of the distributed transmission line with "C_{cn}", "L_w", and "L_p"

The characteristic impedance of the distributed transmission line is dependent on input capacitance of the HBT "Cc_n" and "C_π", the parasitic inductance "L_w" due to gold wire bonding between coupling capacitance and base terminal of the HBT Q_{An}, and the parasitic inductance

"L_p" due to the PCB track. The capacitance values due to PCB track and pads are in *fF* range whereas the inductance value of the PCB track is 0.5 *nH* for 1 mm length [129]. The inductive effect due to the PCB track is significant as compared to the capacitive effect. Hence, the inductive effect is taken into consideration whereas the capacitive effect is neglected in the circuital analysis of the proposed design.

At first, only the effect of "C_{cn}", "C_{π}" and "L_w" is incorporated as shown in Figure 3.12(b). The characteristic impedance Z_{01} is evaluated using (3.8), (3.9) and plotted in Figure 3.13. It can be seen that the variation of characteristic impedance is negligible due to "L_w". In the second analysis, the effect of inductance "L_p" due to the PCB track is also taken into consideration as shown in Figure 3.12(c). The characteristic impedance Z_{02} is evaluated using (3.10), (3.11) and plotted in Figure 3.13. It is observed that the variation in the characteristic impedance is significant due to "L_p". Therefore, the effect of inductance due to PCB tracks and wire bonding are incorporated in the simulation. However, the values of C_{π}, L_p, and L_w are inherently fixed and cannot be altered. Hence, the characteristic impedance of the transmission line can only be tuned by changing the value of Cc_n.

It should be noted that values of Cc_n calculated from (3.7) for the desired gaussian-shape multi-cycle IR-UWB Pulse may result in mismatched transmission lines impedance at the interface of each stage. This causes reflection of the signal at each stage resulting in distorted output pulse shape. Therefore, several iterative simulations have been performed to optimize the coupling capacitance value "Cc_n" for minimum reflection at each stage.

The minimization of reflection produces a smooth impulse voltage with the required delay $\tau_{1,}$ at each input stage of the pulse former. The proposed four-stages of pulse former is used to generate the 4-cycle IR-UWB pulse whose carrier frequency is determined by $1/\tau_1$. For each

cycle, the generated impulse forms half a cycle while the other half is created by reflecting off the short circuit stub with delay $\tau_2/2 = \tau_1/4$ [shown in Figure 3.8.].

All the simulations are performed in Keysight's Advance Design System environment. The Process Design Kit (PDK) of 2 μm GaAs HBT provided by WIN Semiconductor foundry is utilized for the non-linear model of transistors used in the proposed design. The Coil craft ADS RF library file is utilized for off-chip inductor model and Murata ADS library is exploited for off-chip capacitor model. The linear model derived in this chapter is analytically simulated and verified in the MATLAB environment.

3.2.3 Effect of Temperature

The change in temperature of the MMIC will change the amount of stored charges in the *B-E* junction and thus have a dominant effect on the delay in transient response of the HBT. The delay due to temperature change is critical while optimizing the circuit for beamforming applications, where beamforming is sensitive for picosecond (*ps*) change of delay [116]. This section explains the effect of temperature change on the total propagation delay and derives related mathematical models.

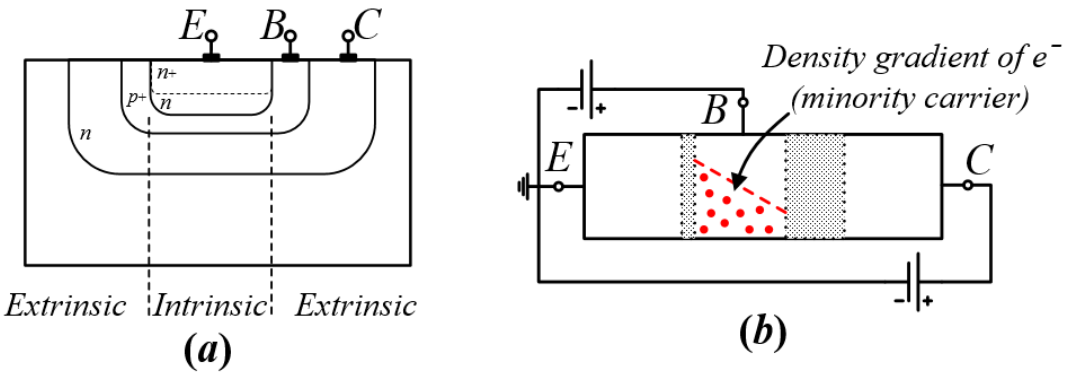

Figure 3.14. **(*a*)** Cross-sectional view of a typical npn HBT showing intrinsic and extrinsic sections, **(*b*)** an intrinsic part of the npn HBT, highlighting minority carrier in the base region due to change in temperature

The rise in temperature changes the parasitic across extrinsic and intrinsic parts of the HBT shown in Figure 3.14(a). However, the parasitic developed across the intrinsic section of the transistor will have a dominant effect on the transient and switching characteristic of HBT. In particular, the capacitance across HBT junctions consist of depletion and diffusion capacitances. The depletion capacitance depends on the depletion width and charge/ions within the depletion region, which is almost invariant with temperature. However, the change in temperature will significantly change the diffusion capacitance due to an increase in minority charge carriers with an increase in temperature. The electrons (minority carrier) density charge gradient in the intrinsic base region of HBT is shown in Figure 3.14(b).

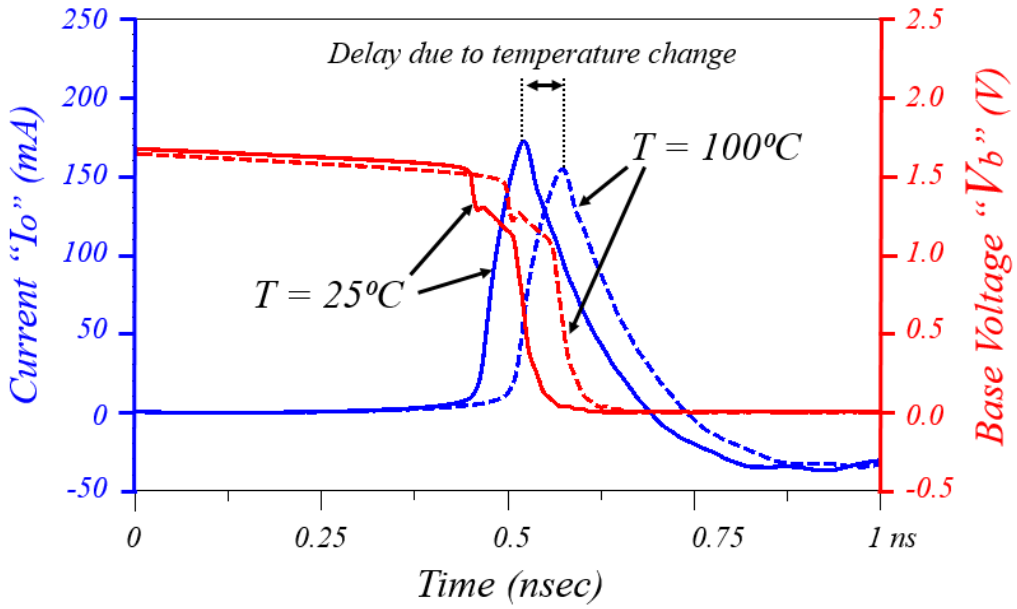

Figure 3.15. Simulated output current *"I_o"* and base voltage *"V_b"* of Impulse generator circuit at room temperature T = 25ºC and T = 100ºC.

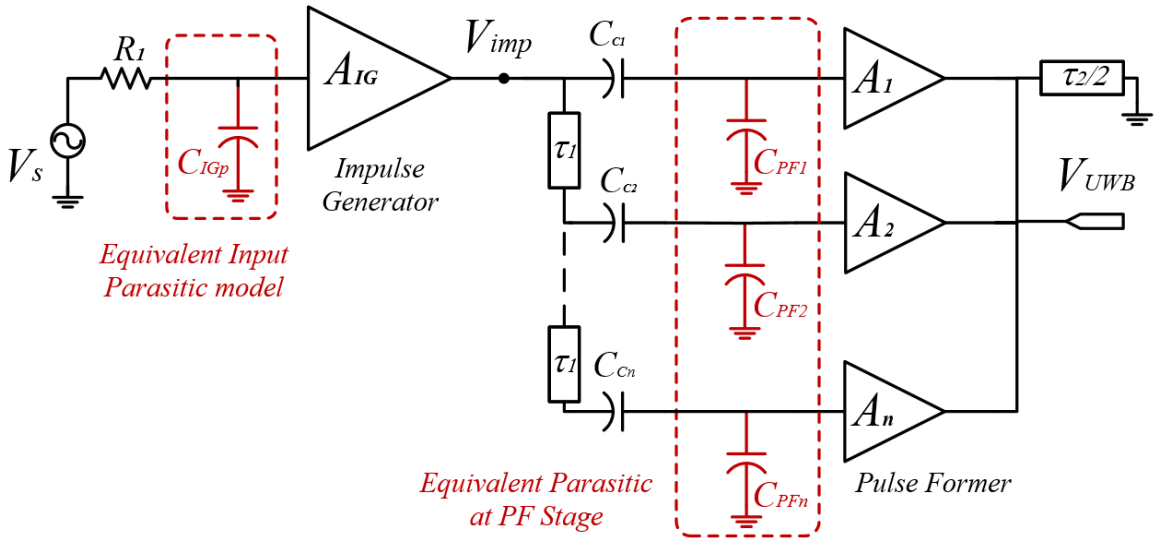

Figure 3.16. Schematic of IR-UWB pulse generator circuit highlighted with parasitic component due to temperature change

The effect of temperature change is investigated by simulation using non-linear VBIC model of HBT in Agilent's Advanced Design System (ADS). Initially *IG* block is simulated and plotted in Figure 3.15. From the simulation results shown in Figure 3.15, the impulse output

current "I_o" is delayed by a significant amount due to change in temperature. It is also noted that the shape of the impulse output current does not change with temperature. For the convenience of modelling and analysis, this can be represented by an addition temperature-dependent parasitic capacitance "C_{IGp}" at the input of the impulse generator circuit, as shown in Figure 3.16. The value of effective parasitic input capacitance calculated from simulated results is ≈ 2 *pF* over a temperature change of 75 degrees. This change is linear with temperature.

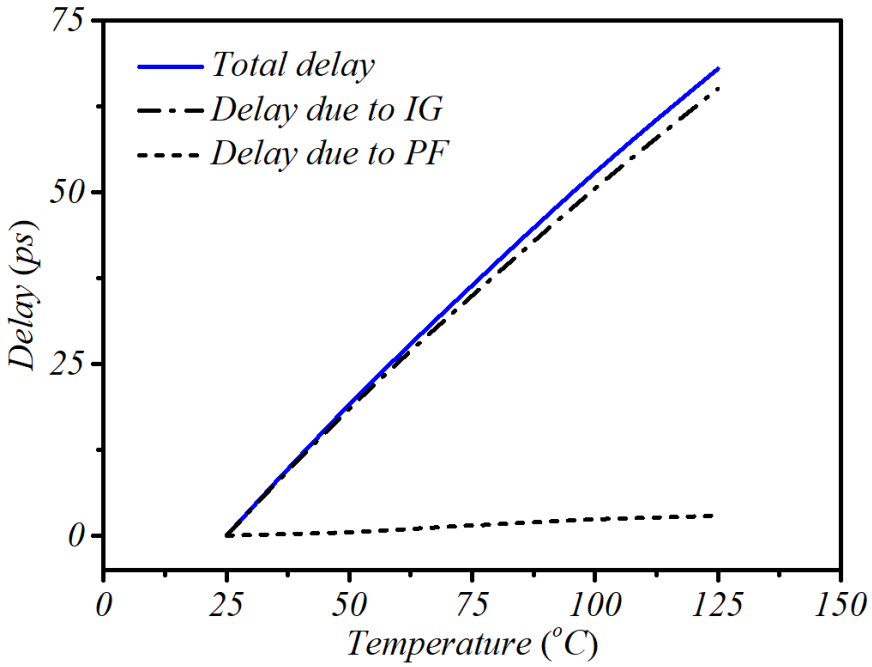

Figure 3.17. The simulated delay of different circuit block with the change in temperature

The effect of temperature on *PF* block is also simulated and delay due to temperature change is plotted in Figure 3.17 together with delay in the *IG* block and total transient delay. In order to simplify the analysis, a temperature dependent parasitic capacitance "C_{PFn}" at the input of the n^{th} stage of PF block is considered, as shown in Figure 3.16. It is important to note that the temperature dependent parasitic capacitance at the input of the *IG* block significantly affects the transient characteristic because the cascode pair is biased in saturation to the cut-off region.

However, in the *PF* circuit, the effect of parasitic capacitance at each stage of the *PF* block is negligible because the cascode pair is operating in the active region (for signal scaling operation), as explained in subsection-3.2. The ADS simulated output IR-UWB pulse with different temperature setting of *IG* and *PF* block are plotted in Figure 3.18.

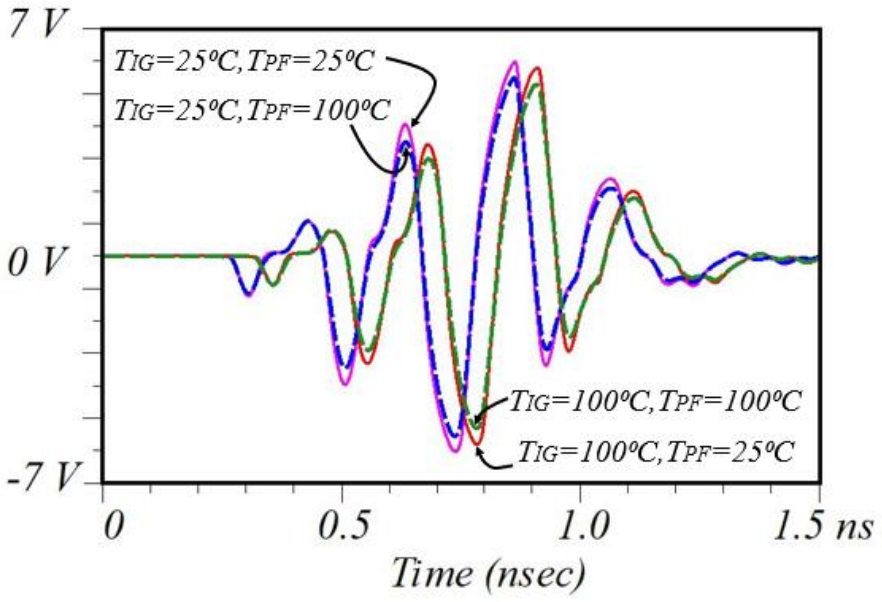

Figure 3.18. Simulated IR-UWB pulse at different temperature of impulse generator (*IG*) and pulse former (*PF*) blocks.

$$V_{UWB} = \sum_{n=1}^{N} \begin{bmatrix} A_n V_{imp} \left\{ t - t_n^{IG}(T_c) - (n-1)\tau_1 - t_n^{PF}(T_c) \right\} + \\ A_n V_{imp} \left\{ t - t_n^{IG}(T_c) - \tau_2 - (n-1)\tau_1 - t_n^{PF}(T_c) \right\} \end{bmatrix} \quad (3.12)$$

Assume that the parasitic capacitor at the input terminal of *IG* and each stage of *PF* causes a transient delay $t_n^{IG}(T_c)$ and $t_n^{PF}(T_c)$, respectively. This transient delay may affect IR-UWB pulse formation, as explained in subsection-3.2. Hence, it is incorporated in the pulse formation equation given in (3.5). The modified equation of pulse formation is shown in (3.12). It is important to note from (3.12) that the $t_n^{IG}(T_c)$ and $t_n^{PF}(T_c)$ will be constant for each stage of pulse formation for a given chip temperature T_c. Therefore, there is neither distortion in the

envelope of the IR-UWB pulse nor frequency change. This will only add an offset delay to the overall pulse formation process, which will change linearly with T_c. The offset delay is an important factor to consider in the case of IR-UWB beamforming for independent transmitting nodes, as reported in [116].

Hence, regulation of the chip temperature of *IG* MMIC can effectively control the offset delay. A feedback loop to the beamforming network should compensate for the parasitic offset delay (minimize the jitter due to temperature change) according to Figure 3.17 to better realize the IR-UWB beamforming, as discussed in [116].

3.3 Fabrication and Measurements

The proposed pulse generator has been fabricated using the 2 μm GaAs HBT process. Two different MMICs, one operating as the Impulse Generator (*IG*) and the other as the Pulse Former (*PF*) have been fabricated. The 2 μm HBT process has the beta (β) value of 75 and common emitter breakdown voltage (BV_{CEO}) of 15 *V*. The biasing voltage values of V_{C1} = 3 *V* and V_{C2} = 10 *V* is chosen by means of iterative simulations and optimization. The fabricated IR-UWB pulse generator PCB board with the impulse generator and pulse former MMICs mounted on it are illustrated in Figure 3.19.

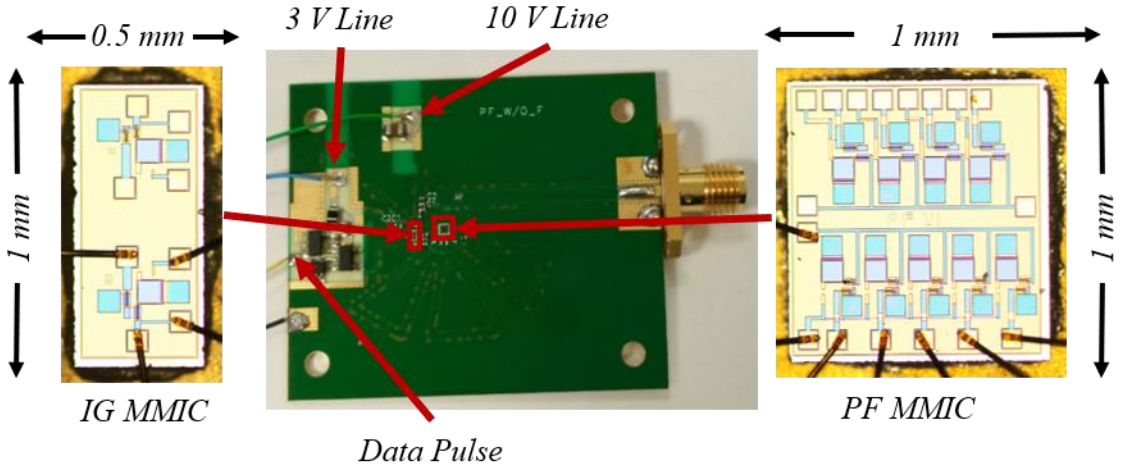

Figure 3.19. Fabricated IR-UWB pulse generator board and MMIC chips.

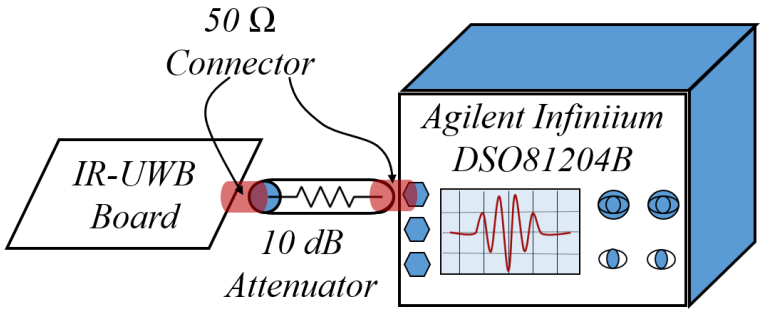

Figure 3.20. Complete measurement setup for time domain IR-UWB pulse.

The output of the fabricated IR-UWB pulse generator board was measured using a high-frequency oscilloscope (*Agilent Infiniium DSO81204B*). The complete measurement setup for time domain IR-UWB pulse is shown in Figure 3.20. The measured IR-UWB pulse with a $V_{p\text{-}p}$ of 10.2 *V* is recorded from the pulse generator terminating with the 50 Ω load impedance. A comparison of the measured and simulated time-domain pulses is presented in Figure 3.21 and frequency domain pulse is shown in Figure 3.22. It can be noticed from Figure 3.21, that the envelope of the measured UWB pulse is not exactly Gaussian bell-shaped. This can be attributed to the effect of the off-chip coupling capacitors Cc_n, which control the amplitude of the individual impulses within the multi-cycle IR-UWB pulse. Since it is extremely difficult to obtain surface-mount capacitors with precise values of capacitance with minimal tolerance range. Capacitors with rating closest to the values used in the simulation of the MMIC have been chosen. This caused the shape of the generated UWB pulse to distort slightly as compared to the simulated pulse.

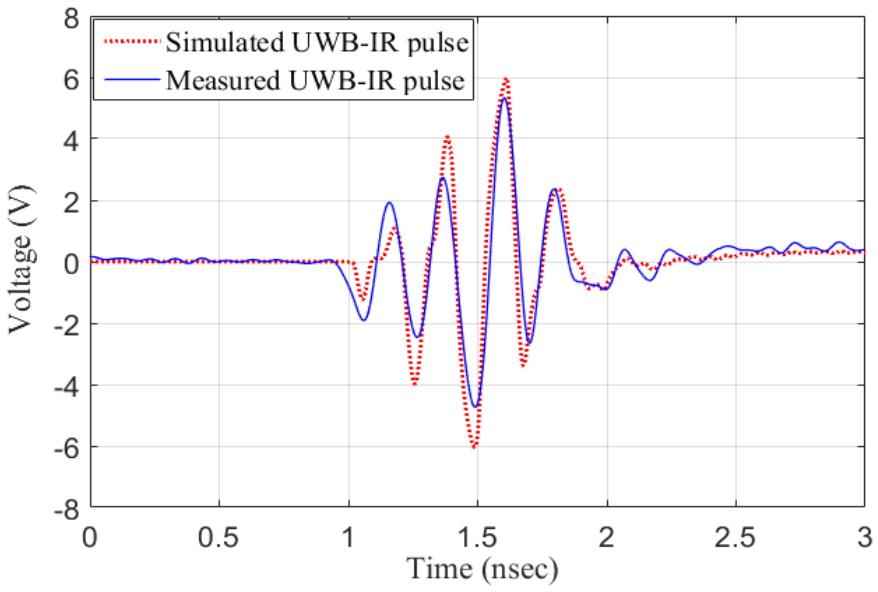

Figure 3.21. Comparison of simulated and measured IR-UWB time domain pulse.

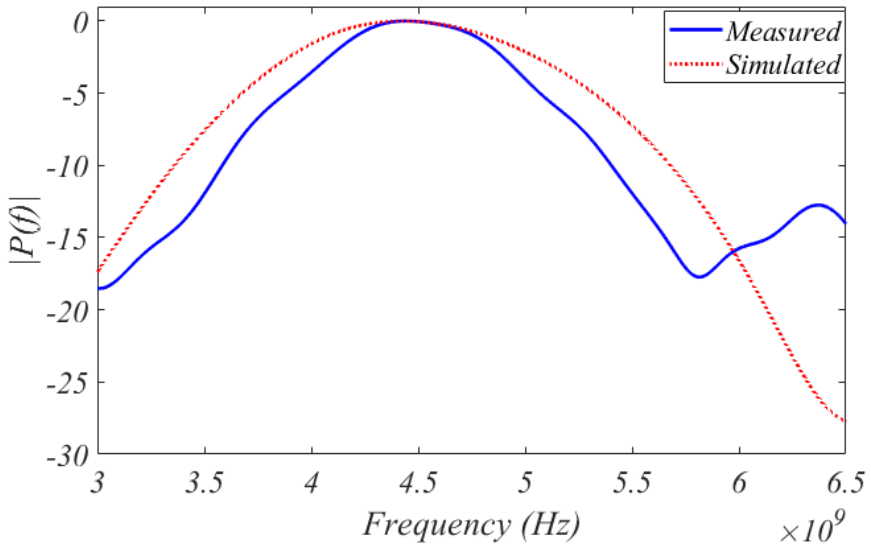

Figure 3.22. Comparison of simulated and measured IR-UWB frequency domain pulse.

The fabricated IR-UWB pulse generator PCB board is indicating *LDC* clock pulse generator, impulse voltage generator (*IG*), pulse former (*PF*) stage, and off-chip transmission line in Figure 3.23(a). The magnified *IG* and *PF* stage on the PCB board highlighting the *IG* and *PF* MMIC chip and off-chip coupling capacitors is shown in Figure 3.23 (b) and (c). A pulse repetition frequency of 100 *kHz* is chosen to satisfy the FCC regulatory spectrum mask limit [46]. The peak power spectral density (*dBm/50MHz*) of the IR-UWB pulse passing through the high pass filter is plotted in Figure 3.24 with the FCC spectrum mask limit. The corresponding time-domain pulse is shown in the inset of Figure 3.24. The center frequency of the measured IR-UWB pulse is 4.45 *GHz* with a –10*dB* bandwidth of 2 *GHz*. it can be clearly observed that the generated IR-UWB pulse is fully utilizing the FCC regulatory spectrum mask limit in the operating band.

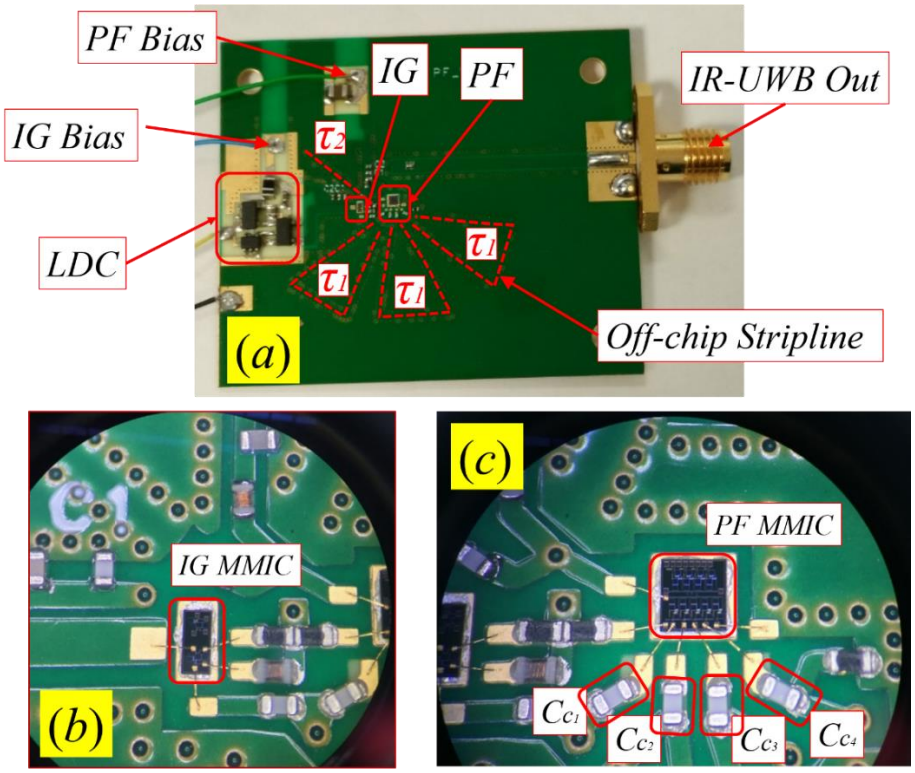

Figure 3.23. (*a*) Fabricated IR-UWB pulse generator PCB board indicating each stage of pulse formation and off-chip delay lines, **(*b*)** magnified Impulse Generator (*IG*) indicating *IG* MMIC chip and **(*c*)** magnified Pulse Former (*PF*) stage indicating coupling capacitors and PF MMIC chip

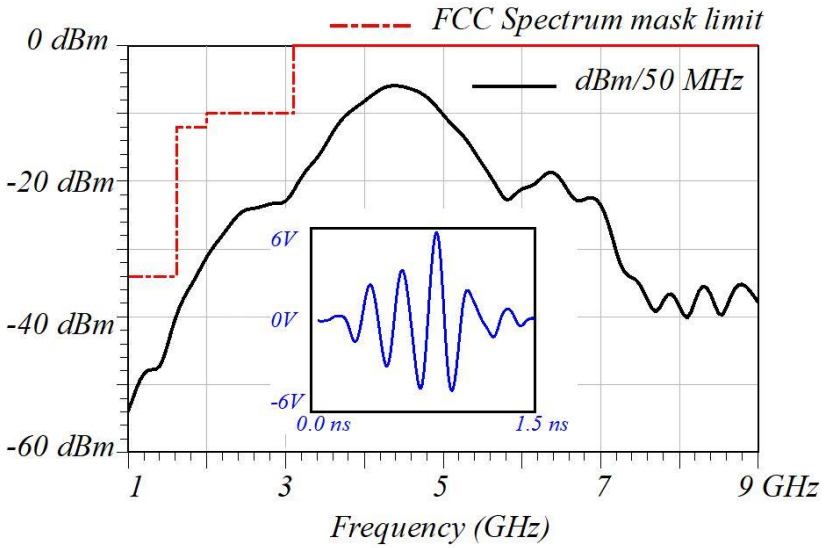

Figure 3.24. The time-domain (inset) and corresponding frequency domain IR-UWB pulse with the peak power FCC Spectrum mask limit in *dBm/50MHz*.

Table 3.1. DC Power consumption of UWB pulse generator.

	Impulse Generator	Pulse Former	Total Power (µW)
Voltage (V)	3.0	10	122
Current (µA)	19	6.5	

$$Efficiency(\eta) = \frac{\frac{V_{peak}^2}{2R_0} \cdot t_{eff} \cdot f_{PRF}}{P_{DC}} \quad (3.13)$$

$$Efficiency(\eta) = \frac{\int_{-T/2}^{T/2} \frac{V_{UWB}^2(t)}{R_0} dt \; . \; f_{PRF}}{P_{DC}} \quad (3.14)$$

Table 3.2. Performance Comparison with available Multi-Cycle IR-UWB Pulse Generators

Process	Peak-to-peak amplitude	%Efficiency	Power consumption	Pulse width (ns)	[Reference] (year)
0.18µm CMOS	1.2 V	---	1 mW	1.0	[96] (2017)
65 nm CMOS	750 mV	---	1.8 mW	0.75	[89] (2016)
0.25 µm BiCMOS	0.7 V	---	43 mW	1.0	[99] (2013)
0.25µm pHEMT	4.5 V	#10%	5 mW	1.0	[86] (2010)
0.25µm pHEMT	6.4 V	#13%	5 mW	1.0	[87] (2011)
2 µm HBT	6.3 V	#10.4%	0.8 mW	1.1	[9] (2010)
2 µm HBT	10.2 V	#18.4% *9.18%	0.12 mW	0.85	This work

** Efficiency calculation based on the energy of the pulse given in (20)*

 # Efficiency calculation based on peak output power

The IR-UWB pulse generator has peak output power of 260 *mW* or 24.15 *dBm*. The total energy associated with the measured IR-UWB pulse is 112 *pJ*. The total power consumption of the IR-UWB pulse generator board is 122 μW per pulse at 100 *kHz* pulse repetition frequency. The individual power consumption of *IG* and *PF* blocks along with total power consumption are tabulated in Table 3.1. The efficiency of the proposed pulse generator is 9.18%, evaluated using (3.13). The integration term in the numerator of (3.13) represents the total energy of the pulse. This term is explicitly chosen to get accurate efficiency in case of the Gaussian-shaped pulse [130], [131]. $V_{UWB}(t)$ represents the IR-UWB voltage pulse and R_0 denoted the load resistance. The term P_{DC} denotes DC power consumption and f_{PRF} denotes pulse repetition frequency.

The obtained results have been compared with state-of-the-art technology as shown in Table 3.2. It can be seen from Table 3.2, that the measured IR-UWB pulse peak-to-peak amplitude of 10.2 *V* is the highest reported value, to the best of authors' knowledge. The efficiency is calculated 9.18% based on the energy of pulse and 18.4% based on peak output power, which is comparable to the reported values.

3.4 Chapter Conclusions

In this chapter, an energy-efficient high peak power IR-UWB transmitter tag with MMIC design and optimization is presented. The improvement technique (using a cascode pair) to get a significantly higher output voltage swing is demonstrated. The 2 μm GaAs HBT process is used for the fabrication of the proposed MMIC. The measured peak-to-peak voltage of the generated IR-UWB pulse is 10.2 V (24.15 dBm) for a 50 Ω load impedance, which is the highest reported amplitude to the best of the author's knowledge. The generated UWB pulse is centered at 4.45 GHz, with a –10-dB bandwidth of 2 GHz. The total power consumption is 0.122 mW at a pulse repetition frequency of 100 kHz and a power efficiency of 9.18% (18.4%) is obtained. An in-depth circuital analysis is performed and explained in detail. The impulse voltage generation process is explained in detail. The analysis of the distributed pulse former circuit is performed to get the proper impedance match and precise amplitude control of impulse voltage at each stage of pulse former. The temperature-dependent parasitic effect is studied, and the corresponding mathematical model is derived. The individual transient delay of each stage of the IR-UWB pulse generator is calculated. The effect of transient delay on IR-UWB pulse formation and beamforming is explained. The proposed pulse former could be extrapolated to the higher UWB band (6-8.5 GHz) by changing the length of off-chip delay lines.

Chapter – 4

Multi-Beam IR-UWB Array: Radiation-Pattern Synthesis & Analysis

The precise positioning of an autonomous robot in a wireless sensor network with a high refresh rate is important for any well-ordered and efficient system. An orthogonally transmitted simultaneous multi-beam system improves the geometric dilution of precision (GDOP) and expedites the refresh rate of the system. In this chapter, the beam-pattern analysis of an electronically steerable multi-beam impulse radio ultra-wideband (IR-UWB) transmitter tag is presented and demonstrated. The multi-beam transmitter tag is optimized to improve the real-time positioning accuracy of an autonomous robot for an indoor positioning and tracking system. Two linear arrays of four elements with an inter-element spacing of 18 cm and 10.2 cm are proposed and optimized. The array with spacing of 10.2 cm is intentionally configured to produce orthogonal beams, which eventually provides better geometric dilution of precision. The beam steering-angle analysis is performed to better utilize the steering delay range and scanning angle range. The radiation intensity in the direction of the transmitted beam is calculated. Consequently, a novel intensity table for the Gaussian-modulated multi-cycle IR-UWB beamforming array is proposed. The intensity table gives an easier way to calculate the peak intensity and the number of cycles of the radiated IR-UWB pulse in the transmitted beam direction. The proposed beamforming transmitter arrays are observed to achieve the scanning

range from –60º (–90º) to +60º (+90º) with a scanning resolution of 5º and 8º in the measurements.

4.1 Introduction

The Impulse Radio Ultra-wideband (IR-UWB) is a promising technology for short-range wireless communication applications due to its inherent properties such as low power consumption, low cost, pulse communication like radar, etc. [1], [2]. The average power spectral density level of the authorized spectrum is below -41.3 *dBm/MHz* for high pulse repetition frequency (PRF) systems, which can be met by arbitrarily high EIRP power level by lowering the system PRF. To limit interferences to other narrowband systems sharing the same frequency band, FCC set the peak power spectral density limit of 0 *dBm/50MHz* [10]. Under this limit, the peak power level of the low PRF system depends on the pulse shape and increases with $20\text{Log}_{10}(B)$, where B is the bandwidth of the UWB pulse. EIRP can be as high as 32*dBm* for pulse shape that occupies 2*GHz* bandwidth [10], [46], [132].

The unlicensed UWB spectrum has drawn the attention of researchers around the globe for a wide range of promising applications such as indoor positioning and tracking [11], [12], [52], vital sign detection [14], [123], [133], ultra-fine infant movement detection [16], real-time monitoring of highways and bridges, and other civil infrastructures etc., [1], [48], [53]. However, there are some limitations with the existing IR-UWB systems, which restrict the technology to encompass an even bigger market size. The major limitation associated with the current state-of-the-art technology is the limited output peak power, as explained in Section-1.1.2 and in [24]–[26], [48], [76], [77].

The limited output peak power causes mainly two issues a) it restricts the range of sensor network: example, in the case of indoor positioning and tracking system, deployment of multiple IR-UWB receivers is needed to cover the larger area such as warehouses, airports, train stations, shopping malls, etc. The performance severely degrades for non-line-of-sight (NLOS) conditions [25], [26], [134], which is very common for such areas of application. b) It directly affects the signal-to-noise ratio of the paths in the channel impulse response. For example, in the case of the radar system, the lower signal-to-noise ratio degrades the quality of received echo signals at various delays, which introduces errors in the final outcomes. The signal to noise ratio plays an important role where ultra-fine movement detection is required such as medical and healthcare applications [14], [16], [34], [133], [135]–[137]. While correlation in a high PRF system can be used to improve the paths SNR, it imposes more time for this process which can have a significant impact on the latency. In addition to these, power consumption is always an issue for a WSN system, which increases the maintenance costs and makes the system expensive [30], [138]. Therefore, a high voltage, high-efficiency IR-UWB transmitter with low power consumption is desirable for a robust system. The open literature has several publications, which sufficiently addressed the generation of the finer pulse-width with low power consumption [5], [9], [89], [96]. These are required for a robust IR-UWB based indoor positioning system. However, the critical requirement for a NLOS indoor positioning system with good precision is to generate an IR-UWB pulse with high peak-to-peak voltage ($V_{p\text{-}p}$) amplitude [25], [26], [134]. In addition to this, a multi-beam IR-UWB system is desirable for the precise indoor positioning system [109]. Such a system directs the energy to the direct path and suppresses multipath energy that produces range bias errors.

The authors of this thesis have developed a high voltage IR-UWB pulse generator and fabricated using 2 μm GaAs HBT, details can be found in Chapter-3. The proposed pulse

generator can produce an IR-UWB pulse with 10.2 *V* (24.15 *dBm*) peak-to-peak voltage amplitude ($V_{p\text{-}p}$), which is the highest reported value to the best of author's knowledge. However, increasing the output voltage causes the breakdown of transistor junctions. Hence, either an alternative fabrication process or beamforming can overcome the issue. The multi-beamforming system not only increases the output peak power level but also helps to get better positioning accuracy. Despite the several advantages of beamforming, it increases the cost and the size of the system. In addition, it is important to note that the output peak power of the beamforming transmitter should follow the spectrum limit regulation as explained in the Section-2.1.5. Therefore, one has to make a trade-off between cost, size and performance. In this chapter, an electronically steerable multi-beam IR-UWB beamforming transmitter array is adopted.

The basic principle of beamforming is to introduce a relative spatial propagation delay between the transmitted IR-UWB pulses, which superimpose each other in space to form an IR-UWB beam in a particular direction. The spatial propagation delay is controlled by varying the inter-element separation between the transmitting nodes. The inter-element spacing, and the number of transmitting nodes decide the number of transmitting beams (grating beams) and the beam-width of the transmitting beams (grating beams). The direction of the transmitting beam depends on the steering delay. The steering delay is the finite delay introduce between the signal chain flow of the array. Various architectures have been proposed and implemented in the open literature. A review of the beamforming techniques is provided in Section-2.3.

In this Chapter, the beam-pattern synthesis and analysis are performed for a multi-beam IR-UWB transmitter tag operating inside the indoor environment. The proposed transmitter arrays are prototyped and demonstrated for multi-beam orthogonal beam-pattern measurements. The main contribution of this chapter is summarized below.

- An electronically steerable multi-beam IR-UWB transmitter array based on a true-time tunable delay cell is proposed and demonstrated for the multi-beam orthogonal beam-pattern measurements. A typical algorithm for determining the orientation of the autonomous robot is discussed.
- Two different arrays are proposed and optimized, in which one array is configured to produce orthogonal beams. The orthogonal beams are intentionally formed to get a better geometric dilution of precision (GDOP) [139], [140].
- In-depth beam steering-angle analysis is performed for the proposed transmitter arrays. This analysis facilitates better utilization of the steering delay range and scanning angle range.
- The intensity table of the proposed transmitter array is explicitly derived to get the information of radiation intensity and pulse cycle in the beam direction.
- Finally, the measurement setup for time-domain radiation pattern measurement is discussed. The measurement results of the IR-UWB transmitter arrays and the comparison with simulation results are presented, which shows a great match.

4.2 Problem Statement

The detection and precise localization of distributed nodes in WSN are one of the key requirements [141]–[143]. The IR-UWB pulse generator produces a very short time pulse [53], [26], which leads to a precise and ultra-fine temporal resolution for the Real Time Locating System (RTLS) application. This is the main reason researchers around the world are interested in developing an IR-UWB system targeted for the RTLS. The RTLS is an electronic system that can track and identify the location of moving objects, mobile people and assets in real-time. In RTLS, readers and tags are arranged in the targeted area of application, where readers receive signals from the transmitting tags and collectively determine the positions of moving objects consisting of the tag [144], [145]. However, in a cluttered indoor environment, the existence of multipath is common due to the presence of reinforced concrete walls, wooden blocks, large metallic objects (such as machines) and humans etc. The presence of these mediums causes enormous attenuation to the IR-UWB signal [25], [26]. The attenuation due to different mediums for various thicknesses is provided in [33]. A typical indoor positioning environment with possible propagation conditions is presented in [116].

A practical example of the autonomous robot in a densely cluttered environment such as an industrial warehouse is depicted in Figure 4.1. There are multiple receiver systems (Anchor Points) mounted at different known positions to cover the complete area of the warehouse. The placement of the anchors can be estimated as per the environment scenario and application requirements [139], [146]. The anchors should be physically connected and synchronized with a wired connection. The proposed system in the mentioned scenario (in Figure 4.1.) has been examined and the advantages of a multi-beam system over a conventional omnidirectional system are discussed. There are mainly two types of information needed for the robots to complete the assigned task efficiently and accurately. Firstly, the estimation of the orientation

of a robot at the beginning of the task. The orientation information helps to plan for collecting the consignment efficiently and estimate the possible execution paths. Secondly, the precise real-time location information helps the robot to follow the desired path accurately and avoid a collision.

The estimation of the orientation of a robot at the beginning of the task without any movement is almost impossible with the conventional omnidirectional systems. The proposed multi-beam (three beams in this case) system can identify the orientation of the robot with the help of a prescribed mode of propagation. In order to know the orientation, it must transmit data in three consecutive modes of propagation with a time-division scheme. The first mode is to transmit beams (red shaded) with no additional steering delay after the initial scanning operation, as shown in Figure 4.2(a). The second mode is to transmit with the additional steering delay of T ($T = 1/f_c$ = time period of the fundamental frequency), which will point only two beams, as shown in Figure 4.2(b). The third mode is to transmit with an additional steering delay of $-T$ as shown in Figure 4.2(c). The decipher data at the anchor point will give the information of the beam. The decipher data string [1 1 1], [1 1 0], and [1 0 1] represent primary beam *"P"*, secondary beam on the positive side *"Sp"* and secondary beam on negative side *"Sn"*, respectively as shown in Figure 4.2(d). The beam steering-angle information and predefine anchor positions collectively estimate the orientation of the robot at the beginning. The accuracy of orientation depends on the beam-width, narrower the beam-width higher the accuracy.

Next, the path following precision depends on the accuracy of the positioning information. The autonomous robot has to estimate dynamic position, which is better in the case of multiple-beam systems exploiting the GDOP technique as compared to Omni-directional system [139], [147]. The multi-beam system inherently minimizes the short multipath, which eventually

gives better dynamic ranging resolution. In addition to this, the accuracy of tag positioning depends on the GDOP value as given in (4.1)and (4.2) [140]. The σ_x and σ_y are the standard deviations of the *x* and *y*-axis components, which is a function of the tag position with respect to the direction of the anchors for a given range measurement error σ, as illustrated in Figure 4.3. The desired ranging beams to the anchors should be orthogonal, as illustrated in Figure 4.3(a).

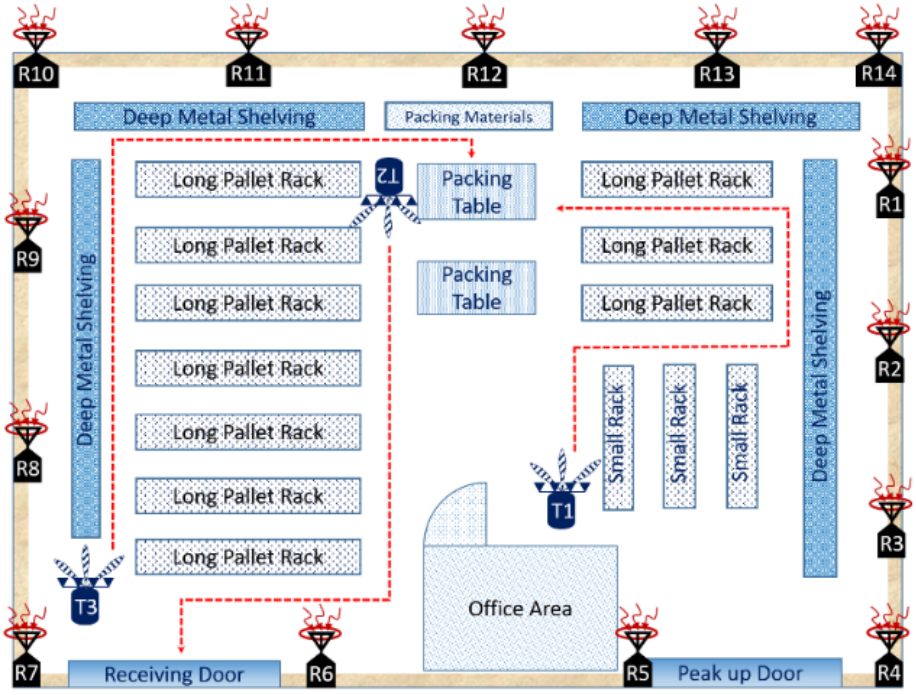

Figure 4.1. An illustration of a real-world condition, where autonomous robots are moving within the industrial warehouse in order to complete the assigned task

$$\Delta Range = GDOP \cdot \Delta Error \tag{4.1}$$

$$GDOP = \sqrt{\frac{\sigma_x^2 + \sigma_y^2}{\sigma} + 1} \tag{4.2}$$

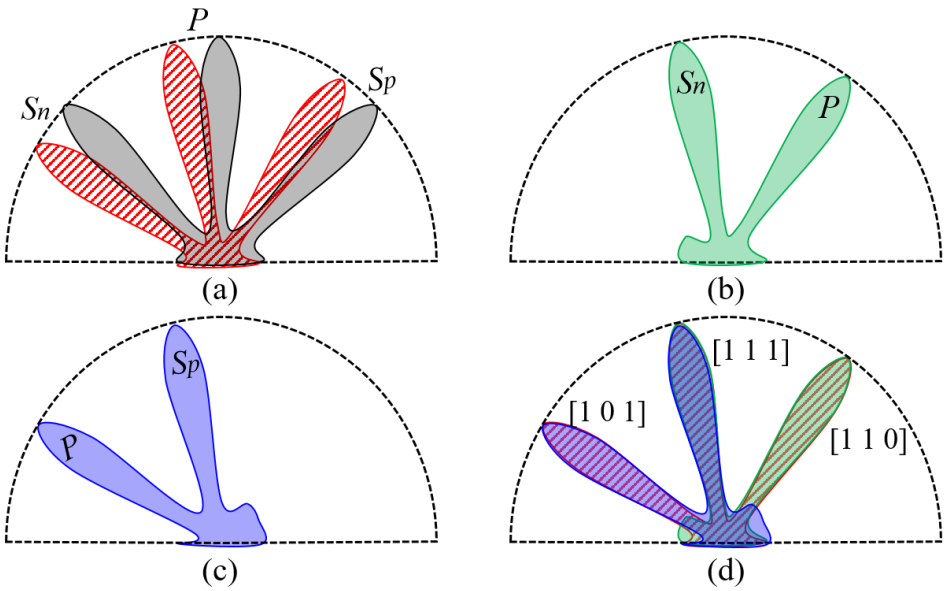

Figure 4.2. Three modes of propagation (a) initial beams (black) and scanning beams (red), (b) scanning beams (green) with an additional steering delay of $+T$, (c) scanning beams (blue) with an additional steering delay of $-T$, (d) all three modes of propagation for determination of orientation.

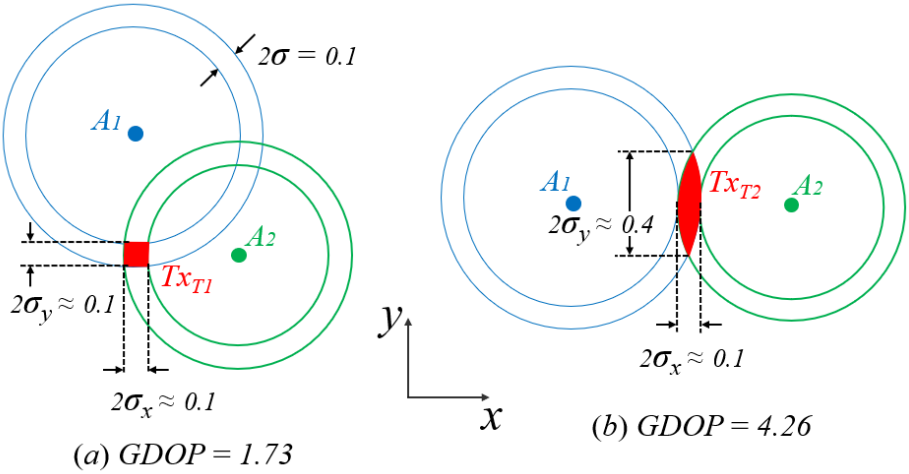

Figure 4.3. Graphical illustration of the geometrical dilution of precision (GDOP). The annulus shows the standard deviation error bounds of the range corresponding to the anchors and the overlapped region in red shows the standard deviation of the expected area of the tag position.

In Figure 4.3(a), the position of tag "Tx_{T1}" is measured by the range calculated by anchors "A_1" and "A_2", which is in orthogonal (intersection angle 90º) directions to the tag position thus giving best GDOP. With the multiple beam system as illustrated in Figure 4.2, beams *"Sn"*

and *"Sp"* are operating simultaneously to the anchors in orthogonal directions thus speeding up the positioning process with good GDOP. The flow chart diagram of the proposed approach is shown in Figure 4.4, which summarizes the complete process.

From the above discussions, it is clear that the proposed multi-beam high peak power IR-UWB transmitter array is pertinent for the application explained above. Nonetheless, the multi-beam IR-UWB transmitter array for the indoor positioning and tracking of moving objects in a densely cluttered environment has not been explored considerably. The proposed work utilizes an energy-efficient, high voltage IR-UWB pulse generator and implements an electronically steerable multi-beam IR-UWB transmitter arrays, which significantly reduces the technology-gap for the aforementioned application.

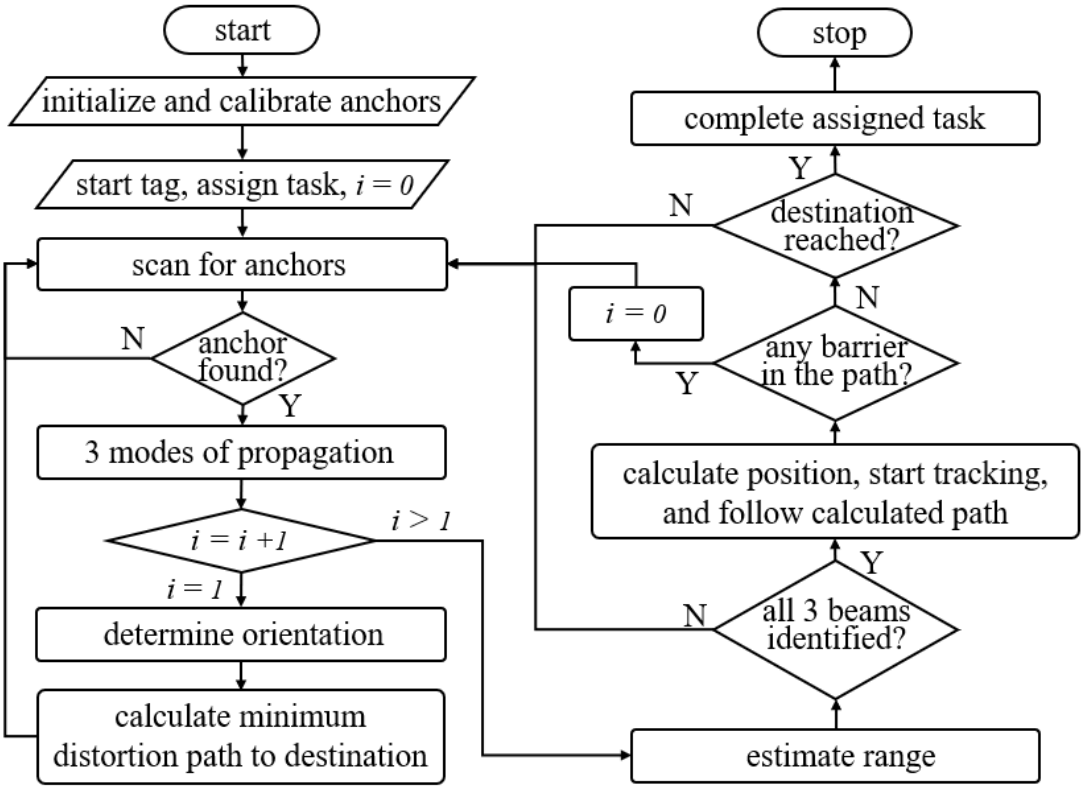

Figure 4.4. Graphical flow chart diagram of the proposed approach

4.3 Radiation-Pattern Synthesis and Analysis

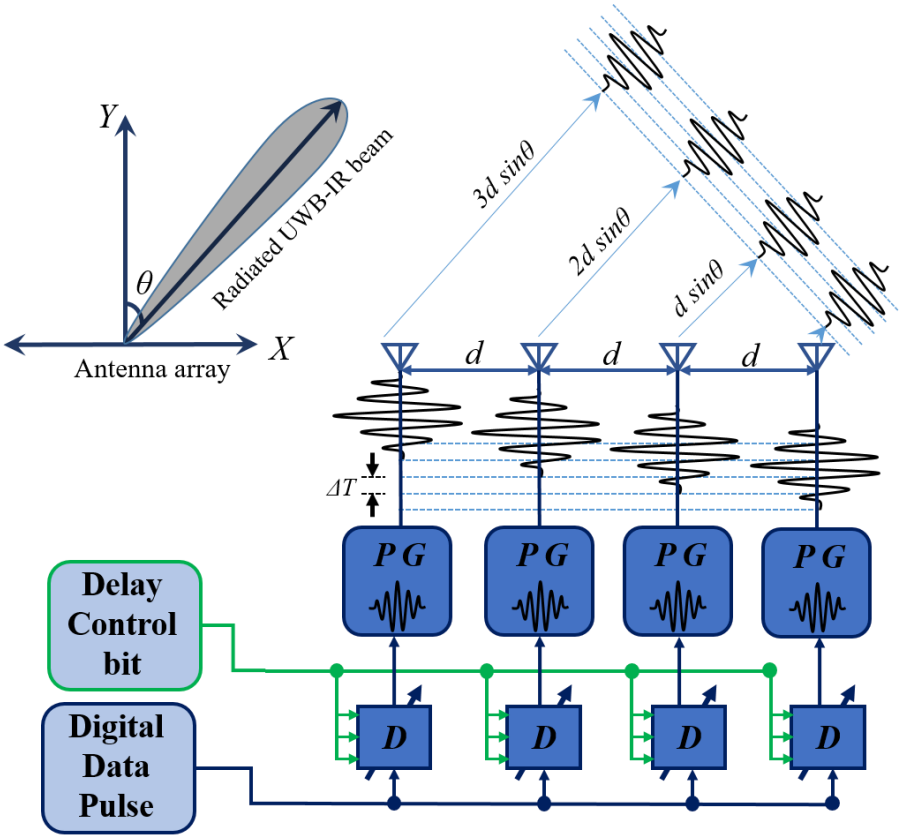

Figure 4.5. Proposed electronically steerable IR-UWB beamforming network with a graphical illustration of multi-cycle IR-UWB beamforming transmitter array operation

The transient approach is preferred for the impulse radio ultra-wideband beamforming study and beam pattern analysis [148], [149]. The basic principle of the time-domain beamforming is to delay the IR-UWB pulse with finite time, which spatially superimposes each other in the aligned direction. The mechanism of beamforming is illustrated in Figure 4.5. The steering angle of the beam depends on the steering time delay between the IR-UWB pulses and the separation between the transmitting elements. The steering angle of the beam *"θ_0"* is defined in (4.3) for a linear array, where ΔT represents the relative steering delay time between transmitting pulses, *"d"* is the separation distance between the antennas and *"c"* is the velocity of the electromagnetic wave [104].

$$\theta_0 = sin^{-1}\left(\frac{\Delta T\, c}{d}\right) \tag{4.3}$$

Realization of the delay elements using RF phase shifter is a commonly used technique [104], [107]. However, the phase shifter is inherently narrowband and designing an ultra-wideband phase shifter is practically problematic [50]. Therefore, as explained in Section-2.3, tunable true-time delay cell-based beamformer would be the right choice for IR-UWB beamforming [15], [50], [104], [106]–[108]. The block diagram of the proposed electronically controlled beamforming transmitter array is shown in Figure 4.5. The digital data pulse is first fed to the tunable delay cells (Block *D* in Figure 4.5), which provides a finite time delay (steering delay) to the data pulses. The IR-UWB pulse generator (Block *PG* in Figure 4.5) uses the falling-edge of the delayed data pulses and generates corresponding delayed IR-UWB pulses [77]. The delayed IR-UWB pulses are transmitted through equally spaced antennas, which superimpose spatially to form a focused IR-UWB beam in the steered direction. The improvement in the directional peak power level of the beamforming transmitter array is expected to increase by $20\log_{10}(N) = 12\ dB$ for $N = 4$ [104], [107].

4.3.1 Simulations and Analysis

A linear transmitter array with four *(N=4)* equally spaced isotropic radiating elements is realized in MATLAB for time-domain beamforming analysis. The time-limited Gaussian-envelope multicycle IR-UWB pulse in (4.4) is used to approximate the generated pulse in Chapter-3. The pulse given in (4.4) is plotted in Figure 4.6, indicating each crest and trough. The peaks (crests and trough) of the time-limited IR-UWB pulse (shown in Figure 4.6.) are

Gaussian-modulated. The resultant received signal in the far-field at any arbitrary angle of observation is given in (4.5) for N number of transmitting elements, where $A_G(\theta)$ is the angular gain of the transmitting antenna [117]. Since the spatial interference of IR-UWB pulses at some observation angle θ may produce dominant positive peak values and at another angle it may produce dominant negative peak values. Hence, the peak-to-peak amplitude has been chosen for the radiation pattern plot to eliminate the ambiguity as shown in (4.6) [50].

$$x(t) = \frac{1}{\sigma\sqrt{2\pi}} e^{-\left(\frac{t^2}{2\sigma^2}\right)} \left(cos2\pi f t\right) \tag{4.4}$$

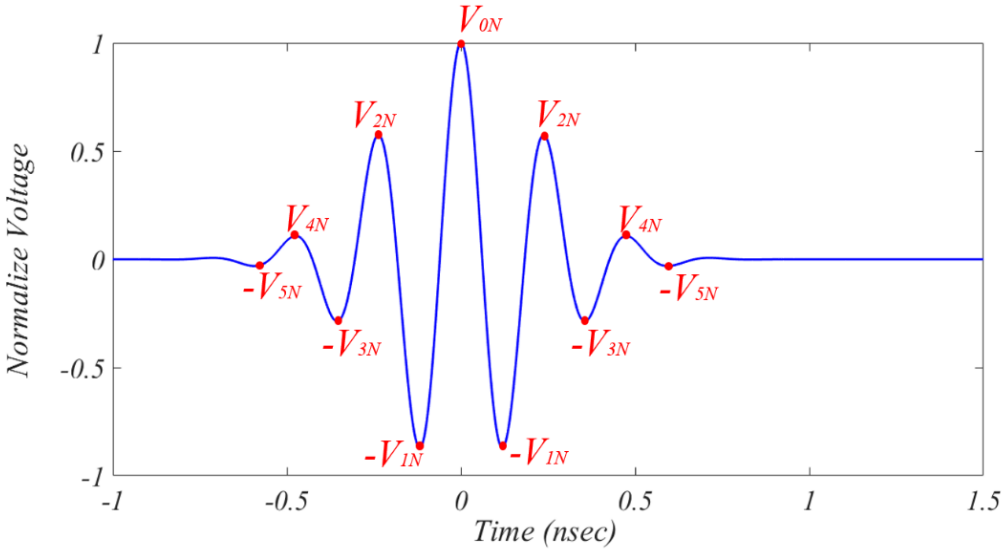

Figure 4.6. An approximated time-limited Gaussian-envelop multi-cycle IR-UWB pulse used in MATLAB simulation as given in (4), indicating peaks

$$y(\theta,t) = A_G(\theta) \sum_{i=1}^{N} x\left(t - (i-1)\frac{d}{c}(sin\theta_0 - sin\theta)\right) \tag{4.5}$$

$$BP(\theta,t) = \frac{\left|y_{P-P}(\theta,t)\right|}{\left|y_{P-P}(\theta,t)\right|_{\max}} \tag{4.6}$$

In the case of monocycle IR-UWB pulse, there would not be any grating radiation beams even if the separation between the transmitting elements exceeds one wavelength "λ" [117]. However, the spatial summation of the multi-cycle IR-UWB pulse may produce multiple additional lobes if the separation (*d* in Figure 4.5.) is larger than one wavelength. This condition is intentionally achieved in the proposed beamforming transmitter array in order to form multiple beams. The number of transmitting beams will be equal to (*2K+1*), where *K* is the integer part of d/λ. The steering angle of the multiple beams can be evaluated using (4.7) for $m = 0, \pm1, \pm2, \ldots \pm K$ [44]. It is important to note [from (4.7)] that the number of transmitting beams depends on the separation (*d*) however, the steering of beams depends on the ΔT.

$$\theta_m = sin^{-1}\left(\frac{\Delta T\ c}{d} - m\frac{c}{f\,d}\right);\quad -90° \le \theta_m \le +90° \tag{4.7}$$

In practical realization, the maximum possible relative steering time delay (ΔT) and delay resolution are fixed by the digitally tunable delay cell *D* in Figure 4.5. Assuming that the maximum possible relative steering time delay is ±600 *ps* for the maximum steering angle of ±90º, the separation between the transmitting antenna elements is 18 *cm* using (4.3). Hence, an array with four transmitting elements (*N=4*) with the separation of 18 *cm* is chosen for the study. The number of transmitting beams in this case at a center frequency of $f \approx 4$ *GHz* ($\lambda \approx$ 7.5 *cm*) will be *2K+1=5*. The peaks of each cycle in the Gaussian-envelope IR-UWB pulse are not equal as shown in Figure 4.6. Therefore, the time-domain summation of four IR-UWB

pulses, relative spatially delayed by one carrier cycle (at first grating beam) will produce peak-to-peak amplitude that is smaller as compared to the summation with no relatively spatially delay (at main beam). Similarly, the resultant peak-to-peak value for the Gaussian-envelope pulse (Figure 4.6) at the second grating beam (relative spatially delayed by two carrier cycles) will be small enough than the main beam to be neglected. Hence, the four transmitting elements separated by 18 *cm* will be approximated to produce three dominant beams, appearing at 0º and ±23.5º for no relative steering delays ($\Delta T=0$), calculated by (4.7) for $m = 0, \pm 1$ and $f \approx 4\ GHz$. The intensity along all the transmitted beam is calculated and explained in subsection-4.3.2 with great details.

The steering-angle analysis of the array of four transmitting elements with 18 *cm* separation is performed for better utilization of steering delay range and scanning angle range. The variation of steering angle with the variation of steering delay (ΔT) between the transmitting IR-UWB pulses is plotted for the array spacing with 18 *cm* in Figure 4.7. It can be seen that one beam transmitter array needs ±525 *ps* steering delay difference to scan the area ranging from -61º to +61º (red line plot in Figure 4.7.) without significant change in beam-width. It can scan up to ±90º, which requires ±600 *ps* relative steering delay. However, the beam width becomes significantly wider at the higher angles. It can also be noted from Figure 4.7. that almost equal area (-59º to +59º) can be scanned with three beams transmitter array without significant change in beam width, which needs only ±275 *ps* steering delay range. The reduction in steering delay tuning range improves the refresh rate of the system. In addition to this, the area between ±27º will be scanned twice, which makes the system more reliable. However, an indoor positioning system with better GDOP requires the IR-UWB beams spatially apart. Ideally, it should be at orthogonal direction as explained in Section 4.2 [139], [140].

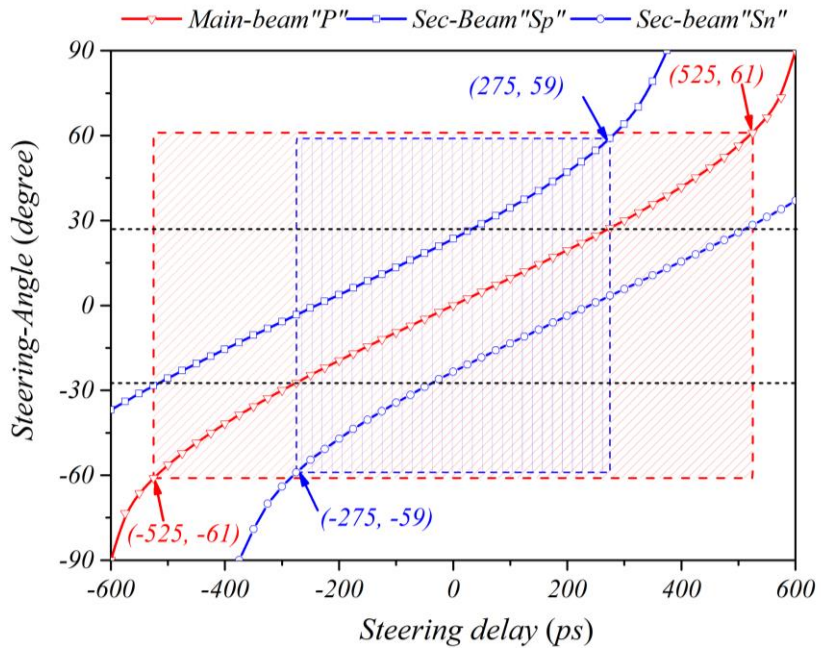

Figure 4.7. Steering angle variation of beams with the steering delay for the array of 4-elements with spacing 18 *cm*

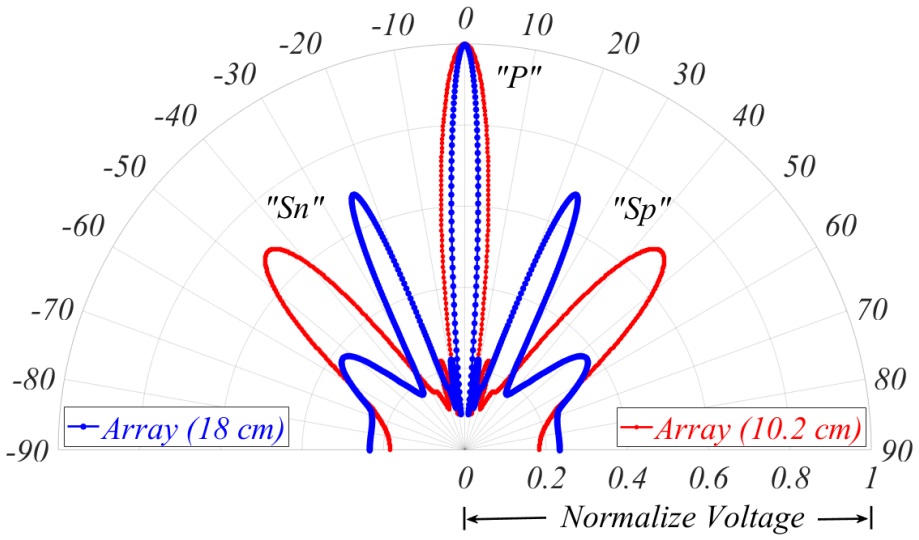

Figure 4.8. The simulated normalized radiation pattern of the arrays with spacing 18 *cm* (Blue) and 10.2 *cm* (Red).

Therefore, in order to improve the GDOP, another transmitter array is optimized. The required separation between a transmitting array of 4-elements is calculated 10.2 *cm* using (4.3) and (4.7), which can produce three beams at 0º and ±45º for no relative steering delay ($\Delta T=0$). The normalized radiation pattern [using (4.6)] of the array with 18 *cm* separation (blue) and

array with separation of 10.2 *cm* (red) is plotted in Figure 4.8. It is evident that the array with separation of 10.2 *cm* has beams at 0º and ±45º, which will eventually improve the GDOP.

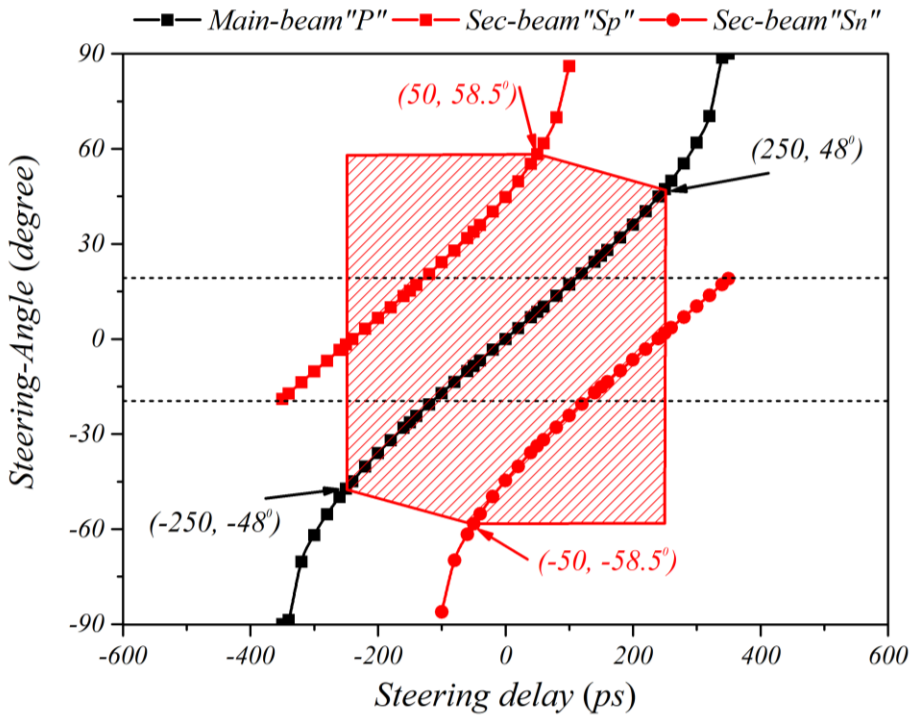

Figure 4.9. Steering angle variation of beams with steering delay for the array of 4-elements with spacing 10.2 *cm*

Similar to the array with a spacing of 18 *cm*, the steering-angle analysis for the array with 10.2 *cm* spacing is performed. The steering angle variations with relative steering delay (ΔT) are plotted in Figure 4.9. Results indicate that ±250 *ps* is required to cover the area between ±58.5º without significant change in beam-width. Additionally, it scans the area between ±20º thrice and the rest of the area twice, which makes the system more reliable. However, for a fast processing system, the array can tune the steering delay variation from 50 *ps* to -250 *ps* or -50 *ps* to 250 *ps* to cover the area between ±58.5º. However, the covered area will be scanned by only one of the three beams in the specified regions. It will make the scanning less reliable but eventually speed up the processing time. This is required for applications with a high refresh rate, where the self-localization of moving objects is needed. Furthermore, it consists of two

orthogonal beams and does not have any minor lobes as compared to an array with d = 18 *cm*, shown in Figure 4.8. However, the beam-width increases as compared to an array with 18 *cm* spacing. Therefore, a trade-off is required according to the specific application scenario. In this chapter, both arrays have been realized and measurement results are presented.

$$y(\theta,t) = A_G(\theta)\sum_{i=1}^{N}\left[\begin{array}{l}\{1-k_R(\mathrm{i})\}\bullet \\ \left\{x(t-J_R(i)-(i-1)\frac{d}{c}(sin\theta_0 - sin\theta))\right\}\end{array}\right] \tag{4.8}$$

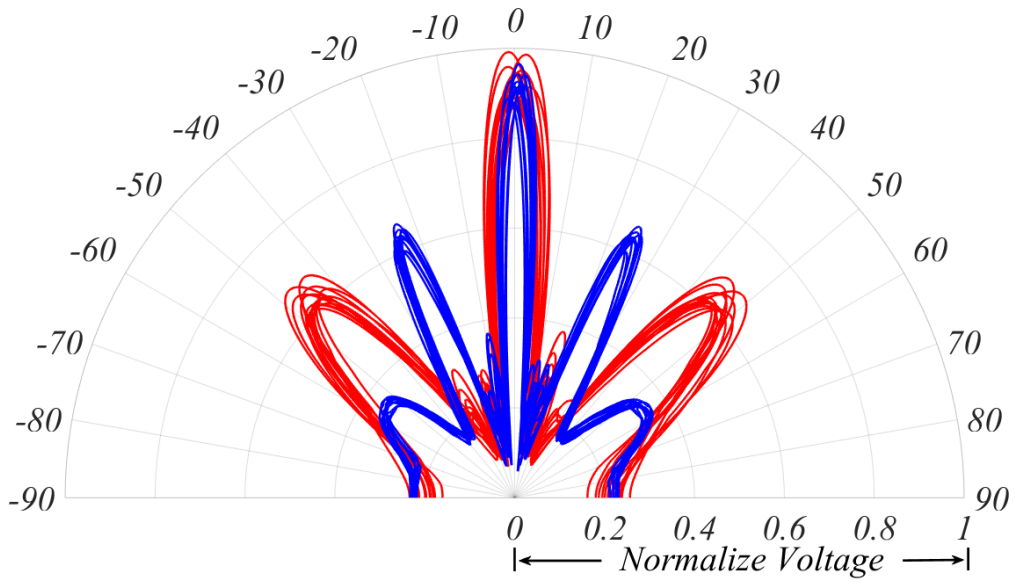

Figure 4.10. Normalized radiation pattern of the proposed array with a random noise range of $0 < k_R(i) < 0.1$ and $-20\ ps < J_R(i) < +20\ ps$.

The measurement noise is added in the simulation to observe the change in the radiation pattern of the proposed array. The received pulse at the receiver in the far-field incorporated with the measurement noise (variation in the steering delay and the amplitude of IR-UWB pulse) is given in (4.8). A random jitter "$J_R(i)$" of ±20 *ps* in the steering delay and random variation of amplitude "$k_R(i)$" of IR-UWB pulse by 10% is incorporated into the simulation as

measurement noise. The normalized beam-patterns with the above-mentioned random noise are plotted in Figure 4.10.

4.3.2 Radiation Intensity Calculation

Table 4.1. Intensity table for the radiation along the main beam of transmitter array with *N* transmitting elements

Electrical length (Time)	*1st Pulse*	*2nd Pulse*	*3rd Pulse*	*4th Pulse*		*Nth Pulse*	*Resultant Pulse*
-7λ/2 (-7T/2)	- -	- -	- -	- -	- -	- -	- -
-3λ (-3T)	- -	- -	- -	- -	- -	- -	- -
-5λ/2 (-5T/2)	$-V_{51}$	$-V_{52}$	$-V_{53}$	$-V_{54}$	- -	$-V_{5N}$	$-V_{5R}$
-2λ (-2T)	V_{41}	V_{42}	V_{43}	V_{44}	- -	V_{4N}	V_{4R}
-3λ/2 (-3T/2)	$-V_{31}$	$-V_{32}$	$-V_{33}$	$-V_{34}$	- -	$-V_{3N}$	$-V_{3R}$
-λ (-T)	V_{21}	V_{22}	V_{24}	V_{24}	- -	V_{2N}	V_{2R}
- λ/2 (-T/2)	$-V_{11}$	$-V_{12}$	$-V_{13}$	$-V_{14}$	- -	$-V_{1N}$	$-V_{1R}$
0	V_{01}	V_{02}	V_{03}	V_{04}	- -	V_{0N}	V_{0R}
λ/2 (T/2)	$-V_{11}$	$-V_{12}$	$-V_{13}$	$-V_{14}$	- -	$-V_{1N}$	$-V_{1R}$
λ (T)	V_{21}	V_{22}	V_{23}	V_{24}	- -	V_{2N}	V_{2R}
3λ/2 (3T/2)	$-V_{31}$	$-V_{32}$	$-V_{33}$	$-V_{34}$	- -	$-V_{3N}$	$-V_{3R}$
2λ (2T)	V_{41}	V_{42}	V_{43}	V_{44}	- -	V_{4N}	V_{4R}
5λ/2 (5T/2)	$-V_{51}$	$-V_{52}$	$-V_{53}$	$-V_{54}$	- -	$-V_{5N}$	$-V_{5R}$
3λ (3T)	- -	- -	- -	- -	- -	- -	- -
7λ/2 (2T/2)	- -	- -	- -	- -	- -	- -	- -

In this section, a novel intensity table is proposed to calculate the radiation intensity and the number of cycles of the radiated multi-cycle IR-UWB pulse along the transmitting beams. The intensity table of the *N* elements Gaussian-modulated transmitter array along the main transmitting beam is shown in Table 4.1. The first column of Table 4.1 indicates the time and corresponding electrical lengths. The pulse generated by each transmitting element (Block *PG* in Figure 4.5.) is converted into the peak's values corresponding to each electrical length indicated in column 1 of Table 4.1 (as indicated in Figure 4.6.). Similarly, the *N* number of pulses is represented by the consecutive columns of Table 4.1. The last column represents the resultant received pulse in the far-field, which is the summation of all peak values in a row corresponding to each electrical length indicated in column 1 of Table 4.1. In the direction of the main transmitting beam, there will be no relative spatial delay between the transmitted pulses. Therefore, all the pulses shown in Table 4.1 are aligned with time. The resultant pulse in the last column is the summation of all the aligned pulses. The amplitude of the resultant received pulse will be *N*-times the individual transmitted pulse. However, the number of cycles of the resultant received pulse along the main beam will be the same as the pulse transmitted by individual pulse generators, as shown in Table 4.1.

The intensity table for the radiation along the first grating beam of an array with four transmitting elements is shown in Table 4.2. At first grating beam (*Sp* beam as shown in Figure 4.8.), the relative spatial delay will be one carrier cycle *T* ($T=1/f_c$). Therefore, all the pulses are shifted by a relative delay of *T* in Table 4.2. Similarly, the *Sn* beam (shown in Figure 4.8.) can be obtained by shifting the column with a relative delay of $-T$. The received resultant pulse along the first grating beam (*Sp* beam as shown in Figure 4.8.) is obtained by the summation of all peaks in a row corresponding to the time shown in column 1 of Table 4.2. Since, the peak value of the cycle is Gaussian-modulated, the maximum peak-to-peak value will be smaller

than the received pulse along the main beam, as shown in Table 4.1. In addition, the number of cycles in the received pulse will increase.

Table 4.2. Intensity table for the radiation along the first grating beam of the array with four transmitting elements

Electrical length (Time)	*1st Pulse*	*2nd Pulse*	*3rd Pulse*	*4th Pulse*	*Resultant Pulse*
-3λ (-3T)	- -	- -	- -	- -	- -
-5λ/2 (-5T/2)	$-V_{51}$	- -	- -	- -	$-V_{8R}$
-2λ (-2T)	V_{41}	- -	- -	- -	V_{7R}
-3λ/2 (-3T/2)	$-V_{31}$	$-V_{52}$	- -	- -	$-V_{6R}$
-λ (-T)	V_{21}	V_{42}	- -	- -	V_{5R}
- λ/2 (-T/2)	$-V_{11}$	$-V_{32}$	$-V_{53}$	- -	$-V_{4R}$
0	V_{01}	V_{22}	V_{43}	- -	V_{3R}
λ/2 (T/2)	$-V_{11}$	$-V_{12}$	$-V_{33}$	$-V_{54}$	$-V_{2R}$
λ (T)	V_{21}	V_{02}	V_{24}	V_{44}	V_{1R}
3λ/2 (3T/2)	$-V_{31}$	$-V_{12}$	$-V_{13}$	$-V_{34}$	$-V_{0R}$
2λ (2T)	V_{41}	V_{22}	V_{03}	V_{24}	V_{1R}
5λ/2 (5T/2)	$-V_{51}$	$-V_{32}$	$-V_{13}$	$-V_{14}$	$-V_{2R}$
3λ (3T)	- -	V_{42}	V_{23}	V_{04}	V_{3R}
7λ/2 (7T/2)	- -	$-V_{52}$	$-V_{33}$	$-V_{14}$	$-V_{4R}$
4λ (4T)	- -	- -	V_{43}	V_{24}	V_{5R}
9λ/2 (9T/2)	- -	- -	$-V_{53}$	$-V_{34}$	$-V_{6R}$
5λ (5T)	- -	- -	- -	V_{44}	V_{7R}
11λ/2 (11T/2)	- -	- -	- -	$-V_{54}$	$-V_{8R}$
6λ (6T)	- -	- -	- -	- -	- -
13λ/2 (13T/2)	- -	- -	- -	- -	- -

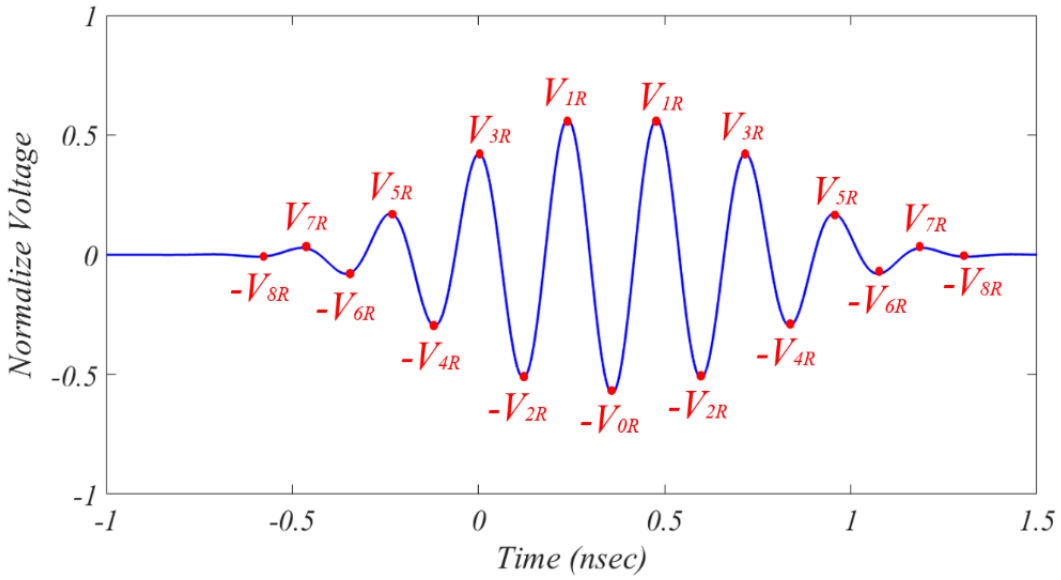

Figure 4.11. The resultant received pulse along the first grating beam of Gaussian-modulated four-element beamformer as obtained in the last column of Table 2.

The simulated resultant received pulse along the first grating beam is shown in Figure 4.11. It is evident from Figure 4.11. that the peak-to-peak amplitude is lower as compared to the pulse transmitted along the main beam and the pulse is broadened as compared to the transmitted pulse (Figure 4.6.). However, the most important thing to notice here that the pulse radiated at the first grating beam (*Sp* beam as shown in Figure 4.8.) is not only time-broadened but it provides an offset to the peak time stamp by *3T/2* as shown in Table 4.2 and Figure 4.11. Similarly, it will cause *–3T/2* offset shift for the first grating beam (*Sn* beam as shown in Figure 4.8). Hence, it is important to compensate for the offset time stamp in the algorithm while calculating the positions of an autonomous robot after identifying the beams as explained in section 4.2. The intensity table along the higher-order grating beam can also be calculated in a similar way but the intensity along the higher-order grating beam will be smaller as compared to the main beam for the IR-UWB pulse shown in Figure 4.6. Hence, the intensity along the higher-order grating beam is neglected.

4.4 Measurement Results

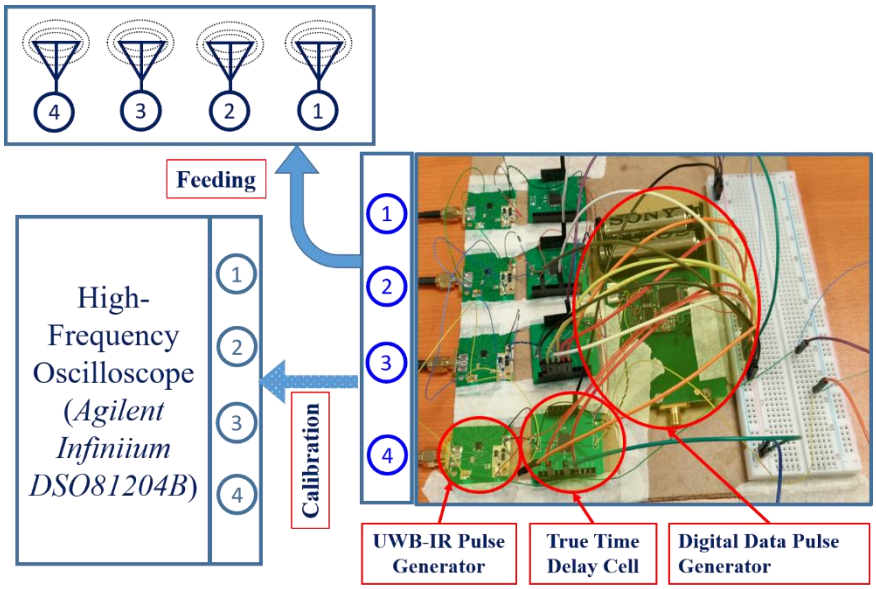

Figure 4.12. Proposed beam-steering sub-circuit for calibration and feeding to antenna, which is realized using relative delay line architecture.

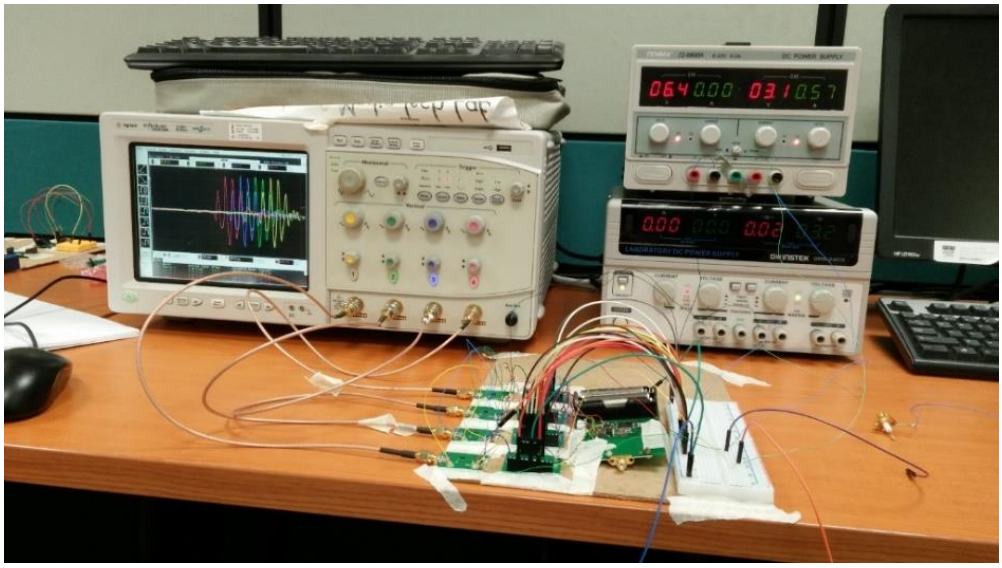

Figure 4.13. Measurement setup for delay calibration

The proposed transmitter arrays have been prototyped using commercially available delay IC *"SY100EP195V"*. It has a total programmable delay range of 10 *ns* with a fine increment of 10 *ps*. The proposed beam-steering sub-circuit is shown in Figure 4.12. In order to verify the steering delay difference between IR-UWB pulses, firstly the output of four pulse generators

is directly fed to an oscilloscope (*Agilent Infiniium DSO81204B*) through the 50 Ω coaxial cable as indicated in Figure 4.12. The IC delays are first calibrated to eradicate the offset between the IR-UWB pulses. The setup for delay calibration is shown in Figure 4.13. The generated UWB pulses are recorded for a different case. First, all the delay elements are tuned to remove the offset delay. The IR-UWB pulse captured after the calibration is shown in Figure 4.14.

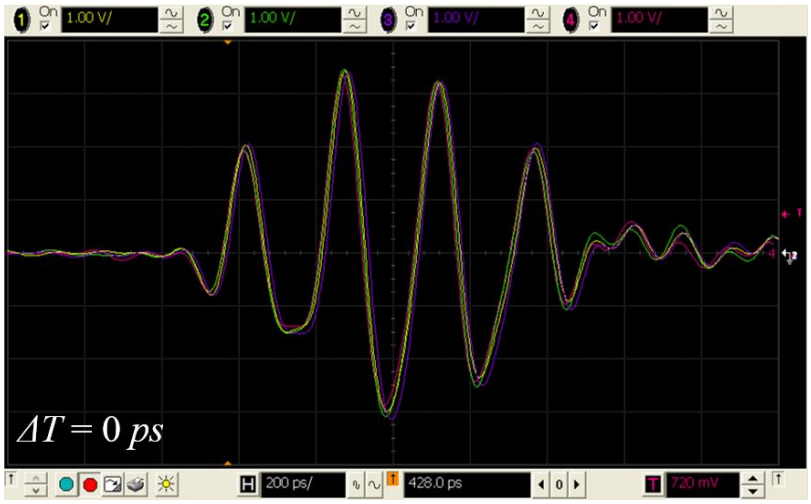

Figure 4.14. Captured IR-UWB pulse after calibration of each delay cell, $\Delta T = 0$ *ps*

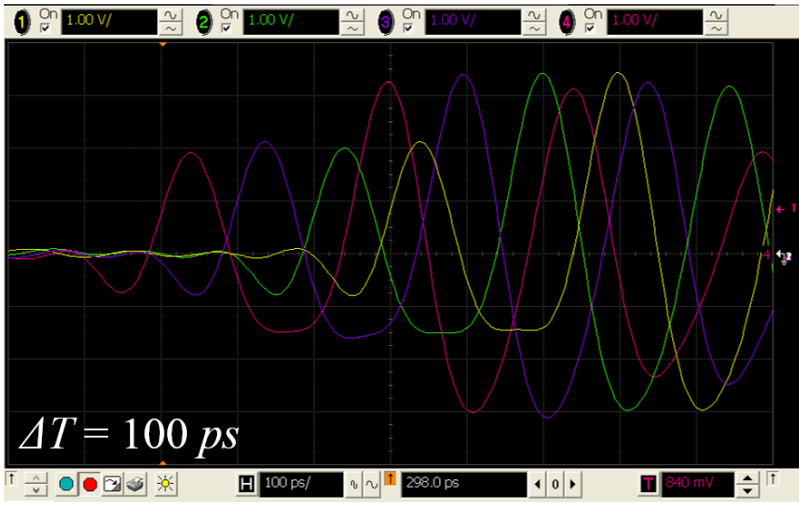

Figure 4.15. Captured IR-UWB pulse with the relative delay, $\Delta T = 100$ *ps*

From Figure 4.14, it can be seen that all the generated pulses coincide with each other. A maximum jitter of value ~20 *ps* is recorded in this case. Similarly, some measurements are also

performed to see the applicability of the proposed method for UWB beamforming and beam steering. The captured results on the oscilloscope are shown in Figure 4.15 to Figure 4.17.

Figure 4.16. Captured IR-UWB pulse with the relative delay, ΔT = 200 *ps*

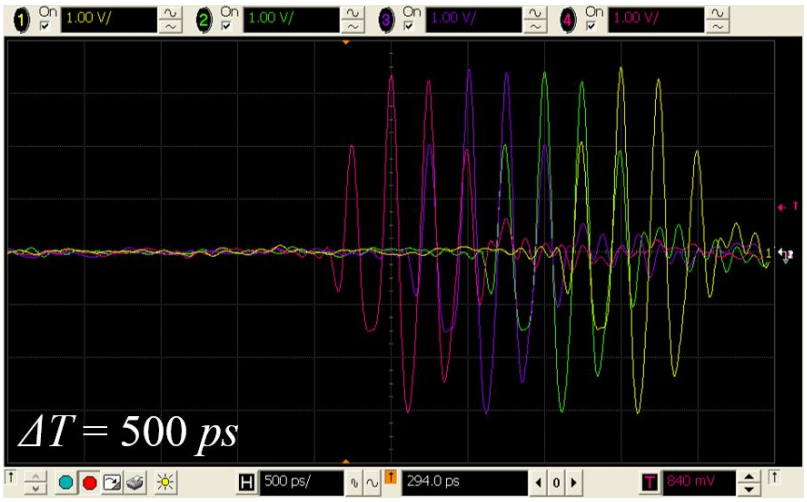

Figure 4.17. Captured IR-UWB pulse with the relative delay, ΔT = 500 *ps*

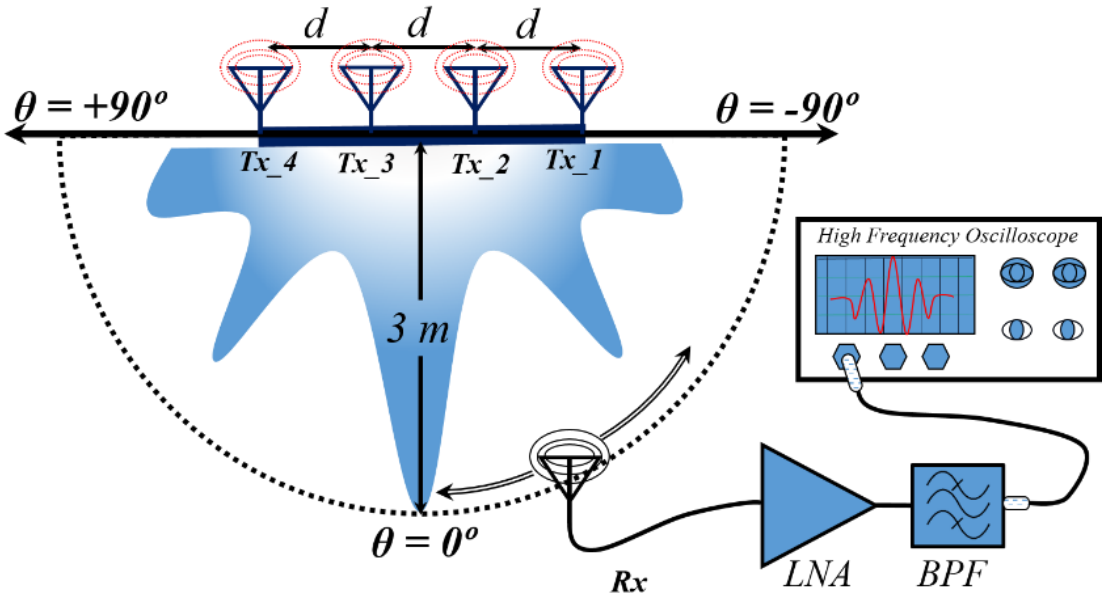

Figure 4.18. Schematic representation of the radiation pattern measurement setup.

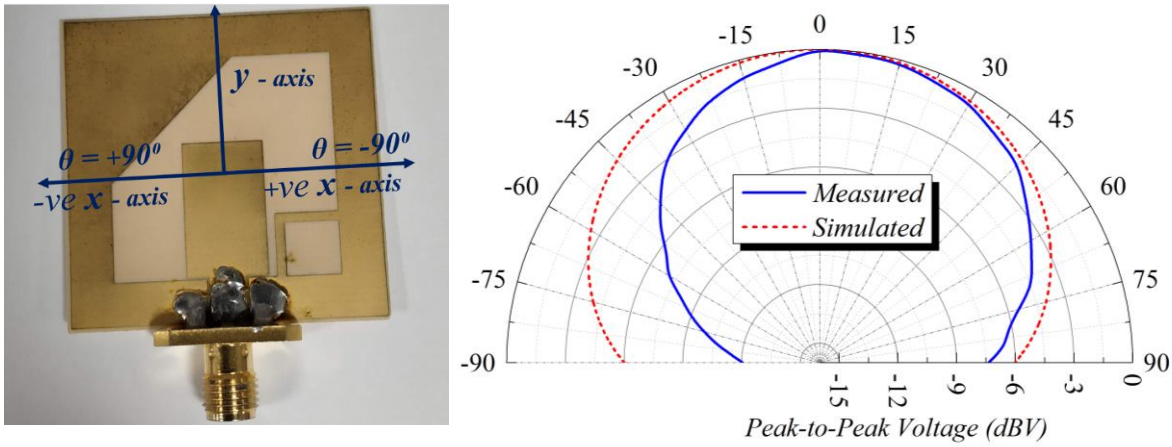

Figure 4.19. Patch antenna and the corresponding measured time-domain radiation pattern (solid blue) with the simulation radiation pattern (dotted red).

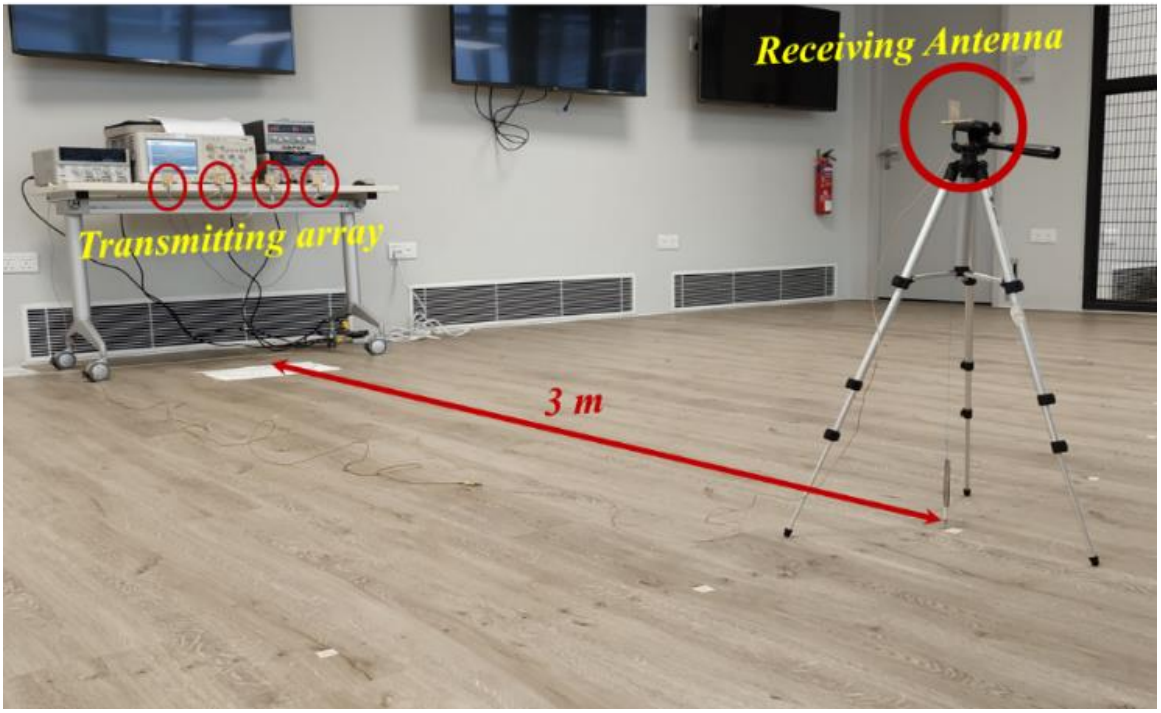

Figure 4.20. Complete measurement setup for the radiation pattern with the transmitting array and the receiving antenna connected to an oscilloscope.

A low-noise amplifier (LNA) and bandpass filter (BPF) are used at the receiving side to amplify the IR-UWB pulse and minimize the noise power level before being measured into a 50Ω oscilloscope. The patch antenna used as the transmitting and receiving nodes is shown in Figure 4.19 along with the measured time-domain radiation pattern. The radiation pattern is plotted by observing the peak-to-peak voltage of the time-domain IR-UWB pulse. A picture of the measurement environment is shown in Figure 4.20. The design parameters and frequency-dependent characteristics of the patch antenna can be found in [150]. The normalized measured beam-patterns with the simulated beam patterns of the proposed transmitter array of 4-elements with a spacing of 18 *cm* are shown in Figure 4.21 and Figure 4.22, and the array with a spacing of 10.2 *cm* is shown in Figure 4.23 to Figure 4.26.

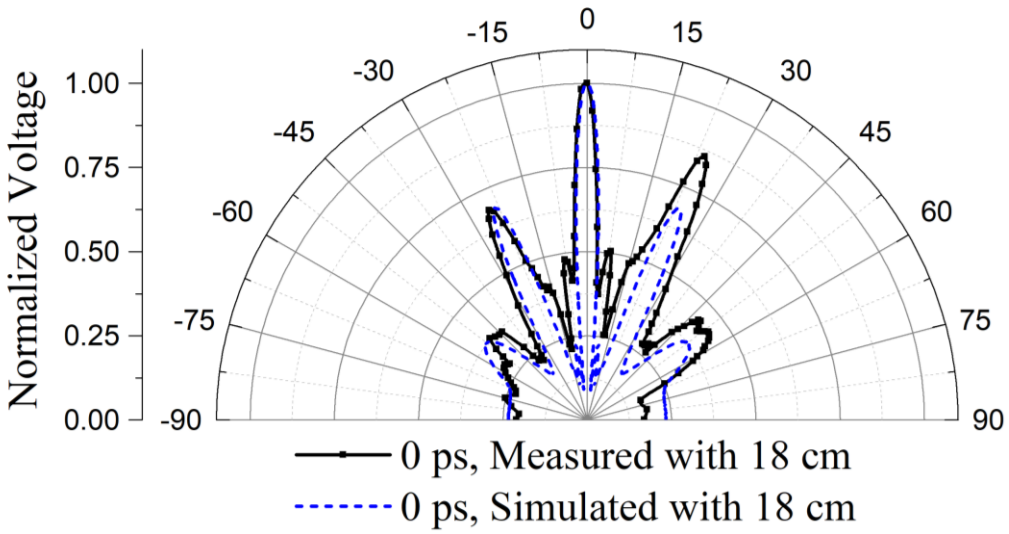

Figure 4.21. Normalized radiation patterns of the proposed transmitter array of 4-elements with spacing 18 cm and no relative steering delay (ΔT = 0)

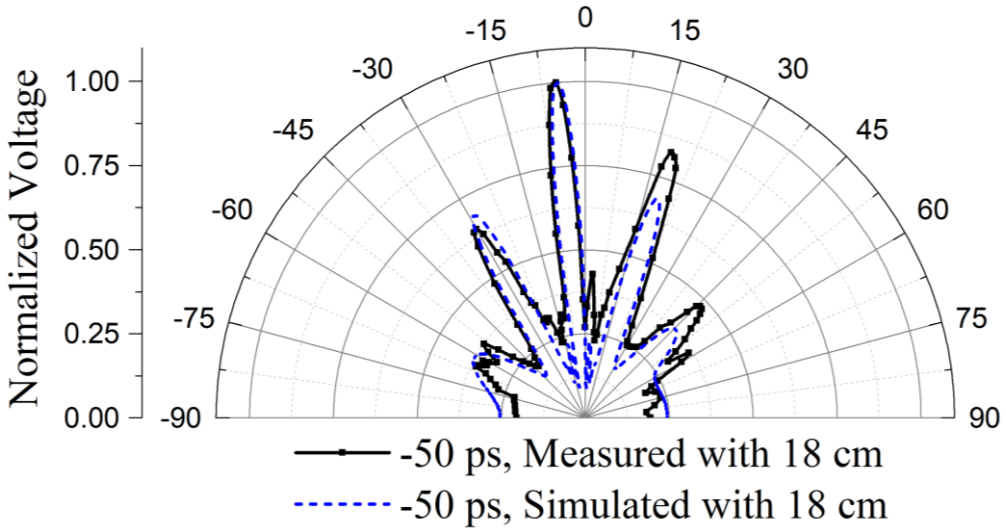

Figure 4.22. Normalized radiation patterns of the proposed transmitter array of 4-elements with spacing 18 cm and ΔT = -50 *ps*

There are three dominant beams in Figure 4.21, which correspond to the array with a spacing of 18 *cm* with no relative steering delay ($\Delta T = 0$). The normalized radiation pattern of the array with 18 *cm* spacing steered by ΔT = *-50 ps* is shown in Figure 4.22. It can be noticed that there are additional beams with significantly less radiation at higher angles as explained in Section

4.3.1, which is undesirable. In comparison, the measured normalized radiation pattern [Figure 4.23] corresponding to the array with d = 10.2 *cm* and $\Delta T = 0$ eradicates the additional beams. In addition, there are two beams focussed at orthogonal directions which will help to get better GDOP. The steered radiation pattern corresponding to the relative steering delay ΔT = *-50 ps*, $\Delta T = +50$ *ps*, and $\Delta T = +250$ *ps* are shown in Figure 4.24, Figure 4.25, and Figure 4.26, respectively. The radiation pattern in Figure 4.26 is similar to Figure 4.2(b), which can be used to determine the orientation of an autonomous robot, as explained in Section 4.2. The observed difference between the measured and simulated radiation patterns [Figure 4.21 to Figure 4.26] is attributed to the antenna element radiation pattern. The radiation pattern of a single antenna element in the simulation compared with the measured time-domain radiation pattern of the opted antenna element is shown in Figure 4.19.

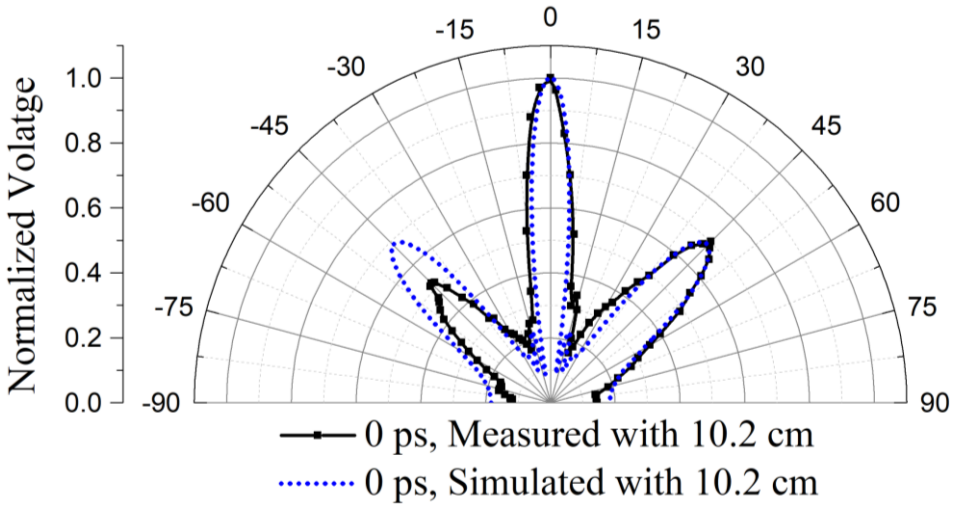

Figure 4.23. Normalized radiation patterns of the proposed transmitter array of 4-elements with spacing of 10.2 *cm* and no relative steering delay (ΔT = 0)

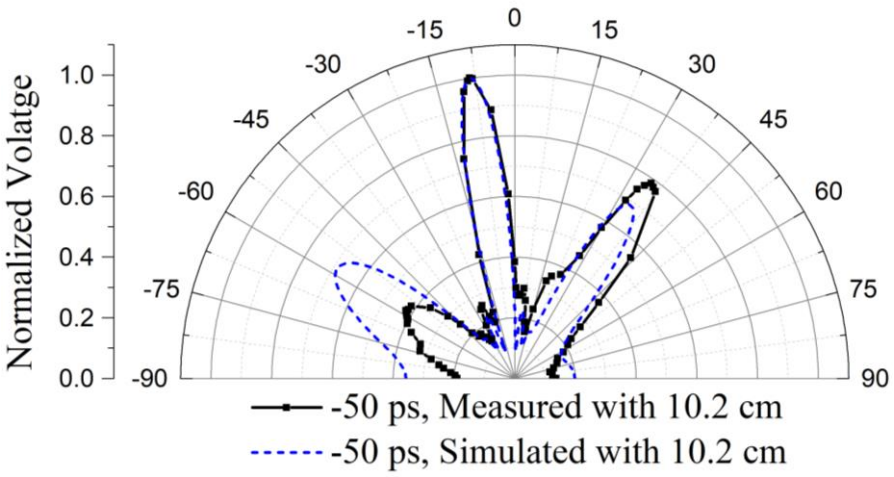

Figure 4.24. Normalized radiation patterns of the proposed transmitter array of 4-elements with spacing of 10.2 *cm* and ΔT =-50 *ps*

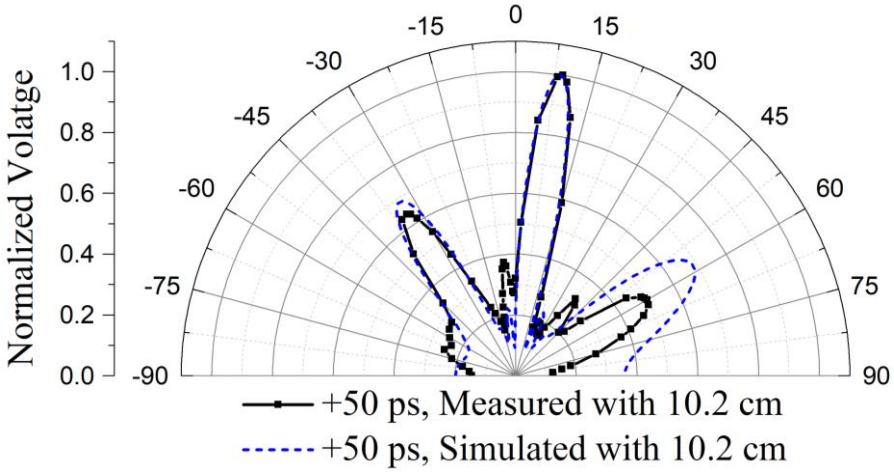

Figure 4.25. Normalized radiation patterns of the proposed transmitter array of 4-elements with spacing of 10.2 *cm* and ΔT = +50 *ps*

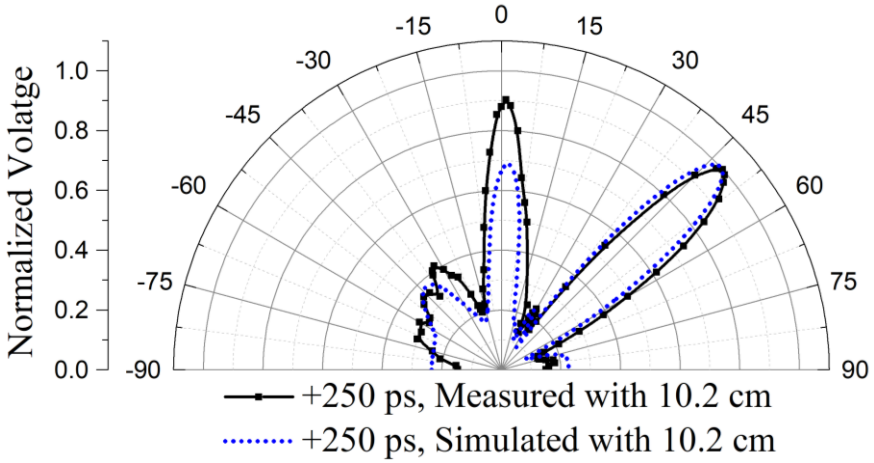

Figure 4.26. Normalized radiation patterns of the proposed transmitter array of 4-elements with spacing of 10.2 *cm* and ΔT = +250 *ps*

Table 4.3. Comparison of IR-UWB Beamforming with Current State-of-the-art Technology

References	[50]	[106]	[104]		[15]	This work	
Operating Frequency (GHz)	3-10	0-6	3-5		3-10.5	3-5	
Number of channels	11	4	4		4	4	
Delay range (ps)	0 to 500	±880	-420 to 700		±64	±250 (±600)	
Scanning Resolution (degree)	9º	10º	0.4º	1º	7º	5º	8º
Antenna Spacing (cm)	18	30	30	18	10	18	10.2
Scanning range (degree)	0º to 59º	-60º to 60º	-25º to 45º	-45º to 90º	-37º to 37º	-60º (-90º) to +60º (+90º)	

A comparison table of the proposed transmitter array with state-of-the-art technology is shown in Table 4.3. It can be seen from Table 4.3 that the proposed design is able to scan the area ranging from -60º to +60º without significant change in beam-width, which only required ±250 *ps*. More significantly, multiple beams are formed which will speed up the localization refresh rate and help to achieve precise indoor positioning of the autonomous robots.

The dimension and power consumption of the array for the aforementioned application is critical, which should be optimized as per the application requirement. In this chapter, the dimension of an array was estimated to 0.5m for practical consideration. Under this consideration, initially a 0.54m long array is proposed. However, after detailed analysis and optimization, an array with an array length of 0.36m is opted, which not only improves mechanical stability but it also provides better GDOP. The power consumption for an IR-UWB pulse generator is calculated 0.12mW in the Chapter-3. Therefore, the power consumption for

an array with four pulse generators will be $0.48mW$. The power consumption in the true time delay cell is not included in the calculation. Since the delay cell used for the implementation is commercially available delay *IC "SY100EP195V"*. The power consumption is higher for the commercially available IC as compared to the IR-UWB pulse generator. However, it is important to note that the power consumption will be considerably low for integrated delay cell.

4.5 Chapter Conclusion

In this chapter, an innovative method of achieving better accuracy in the case of an autonomous robot deployed in the industrial environment is presented. A multi-beam IR-UWB transmitter array is proposed, implemented and related measurement results are provided. The beam steering-angle analysis is presented. The radiation intensity calculation is performed and a novel intensity table is proposed, which helps to determine the intensity of the radiated pulse and quantify the broadening of pulse in terms of the number of carrier cycles present in the pulse. Eventually, two transmitter arrays with separation of 18 *cm* and 10.2 *cm* are optimized and demonstrated. The array with 10.2 *cm* spacing is found better for the use case explained in the chapter. The optimized arrays are tuned to different steering angles and time-domain radiation patterns are plotted. The comparison between the simulated and measured radiation patterns are provided, which show a great match. The true-time digital delay cell is exploited, and the steering range from -60º (-90º) to +60º (+90º) with a scanning resolution of 5ºand 8º is achieved and demonstrated.

Chapter – 5

Grating Lobe Reduction of Collaborative Beamformer

In this chapter, a novel algorithm for the separation between distributed radar sensor nodes of the virtual non-linear array is proposed for collaborative beamforming in a wireless sensor network system. The proposed algorithm can form a collaborative virtual radar array to produce a single beam radiation pattern. The presented radiation pattern is proposed for Gaussian-shaped multi-cycle IR-UWB beamforming, which effectively reduces the grating lobes despite electrically large separation between transmitting nodes. A random error of sensor nodes' position and random jitter for different IR-UWB pulse is incorporated in the analysis and related simulation results are provided. A discussion on the study of random error is provided in detail. A prototype for the time domain beam-pattern measurement is developed for proof of concept. The measurement results show better than 6 dB suppression for side lobes radiation.

5.1 Introduction

The IR-UWB based indoor positioning and tracking system provides precise positioning information. As discussed in Chapter-3 and Chapter-4, the output peak power limits the range of positioning. Hence, in case of long-range positioning environments such as airports, shopping malls, railway stations etc., a single narrow beam radiation-pattern is required. In order to get an arbitrarily narrow beam, the array length should be comparatively larger, which will be mechanically unstable. The advancement of Internet-of-things (IoT) technology, together with a precise indoor positioning system enables Radar Sensor Network (RSN) for various collaborative applications. The applications are through-the-wall collaborative imaging and mobile robot formation control such as drones operating collaboratively to send signals in a certain direction [111], [115], [121], [122].

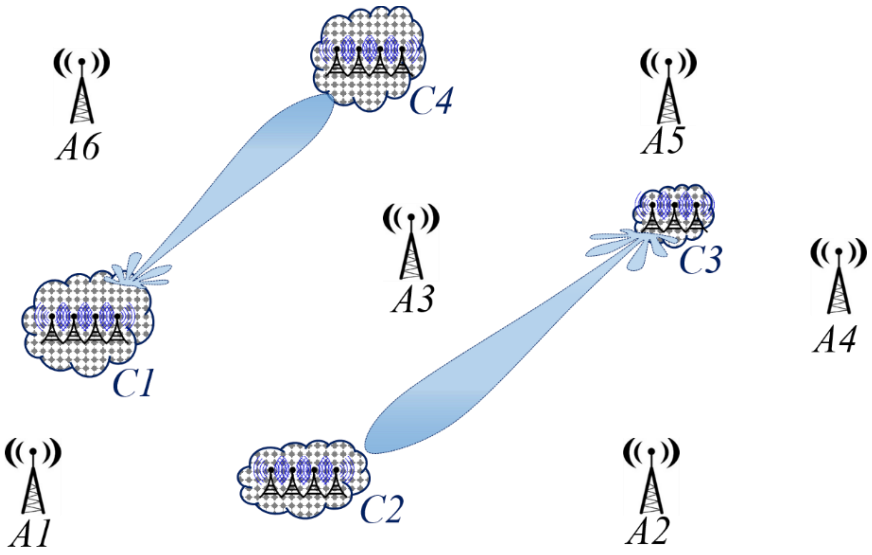

Figure 5.1. Pictorial representation of a typical collaborative array for a cluster to cluster communication in long-range indoor environments such as airports, shopping malls, etc.

In this chapter, collaborative formation is utilized for the long-range cluster-to-cluster communication and high-resolution imaging applications. A typical pictorial representation of

collaborative beamforming for the cluster-to-cluster communication is illustrated in Figure 5.1. The clusters are fairly apart from each other, where a single node is not able to send the signal to another concerned cluster. Additionally, the same configuration could be used in the wireless radar sensor network for a collaborative high-resolution imaging application. It is important to note that the collaborative array could produce an arbitrary narrow beam width but it will also produce multiple grating lobes. The narrow beam is desirable but multiple grating lobes are not desirable for the proposed application. In this chapter, an algorithm for the collaborative sensor node formation is proposed, which can produce a single narrow beam radiation pattern in case of electrically large separation between the sensor nodes.

The state-of-the-art related to IR-UWB beamforming can be found in Section-2.4. It is important to note that collaborative beamforming in WSN has several challenges. Researchers have divided the problem into the following four major categories for independent research. The research categories are a) beam pattern synthesis and analysis, b) power and lifetime optimization, c) sensor nodes synchronization, and d) WSN prototypes for collaborative beamforming [111]. This chapter mainly focuses on the time-domain beam pattern synthesis and analysis in the case of a multi-cycle Gaussian-shaped IR-UWB pulse for collaborative beamforming. In addition to this, a prototype for beam-pattern measurement is developed for the proof of concept.

In this chapter, a novel algorithm for the separation between transmitting nodes of the virtual radar array is discussed for the multi-cycle Gaussian-shaped IR-UWB pulse. The time-domain radiation pattern analysis of non-linear virtual transmitter array is performed for the various case. A prototype is developed for experimental verification of the simulated transmitter array radiation pattern. The prototype exploits tunable true-time delay cells at the excitation clock signal, which enables scanning features for the targeted area. The architecture as shown in

Figure 5.19 eliminates the need for a phase shift network at the IR-UWB signal output frequency, replacing it with the phase shift network at the driving clock frequency. Two transmitter arrays with different array spacing are optimized and implemented. The measured radiation patterns are compared with simulation results, which shows a great match.

5.2 Theory of Time Domain Beamforming

The multi-cycle IR-UWB beamforming can be studied using transient beam-pattern analysis [148], [149]. The principle of time-domain beamforming is simply adding all the spatially delayed time-domain transmitted pulse from the antenna elements in the far-field region, as shown in Figure 5.2. In the case of a mono-cycle pulse, the broadening of received pulse in the time axis will produce one dominant peak in the angular domain. However, in the case of the multi-cycle pulse, the broadening of the received pulse will produce multiple dominant peaks at a different angle of observation, if the inter-element separation is more than a wavelength *"λ"*[117].

The multi-cycle Gaussian-shaped IR-UWB pulse generated in Chapter 3 for a sensor node is approximated by *x(t)*, which is given below in (5.1), where σ^2 is the variance of Gaussian envelop and f_c is the sinusoidal center frequency. As shown in Figure 5.2, the generated IR-UWB pulse is fed through variable steering-delay blocks T_n, ($n = 1, 2 \ldots N$, where N is the number of transmitting nodes) to sensor nodes. Initially, it is assumed that the transmitting sensor nodes are synchronized with each other and the separation between the nodes are equal, such as $d_{12} = d_{23} = \ldots = d$.

$$x(t) = \frac{1}{\sigma\sqrt{2\pi}} e^{-\left(\frac{t^2}{2\sigma^2}\right)} \cdot cos(2\pi f_C t) \tag{5.1}$$

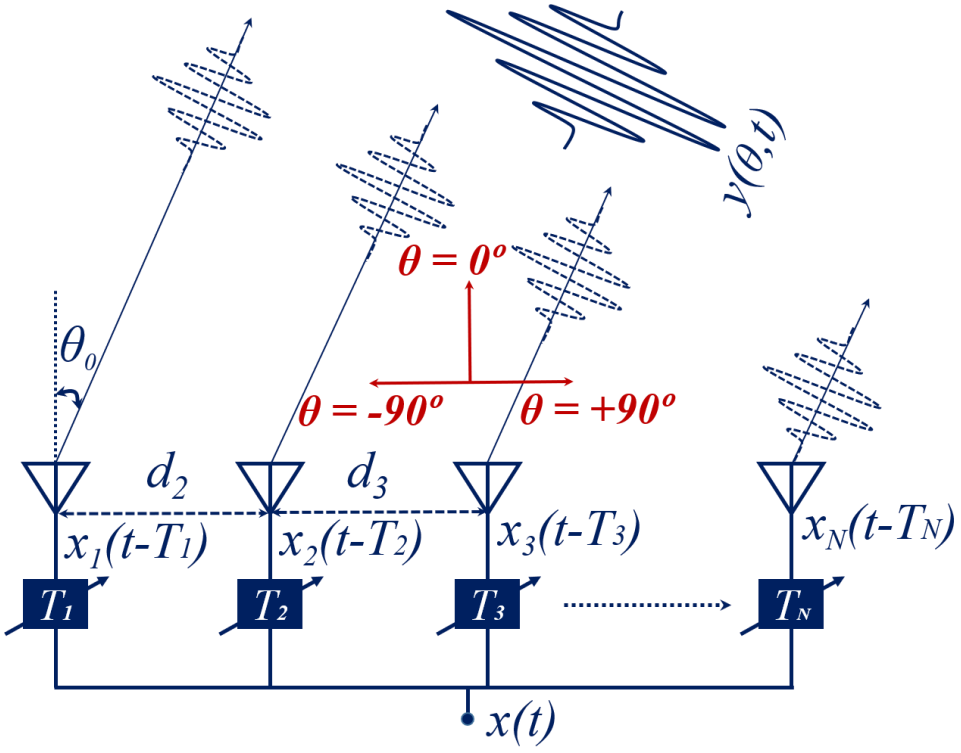

Figure 5.2. Typical block diagram representation of time-domain beamforming of multi-cycle Gaussian envelope IR-UWB pulse for synchronizing sensor nodes

The variable steering-delay block "T_n" in Figure 5.2 controls the steering angle *"θ_0"* for the main lobe of the directional beam pattern. The steering angle measured with respect to the broadside direction of the transmitting antenna array. The values of steering angle *"θ_0"* for transmitting beam ranges from -90^o to $+90^o$ at both end-fire direction of the transmitter array, as illustrated in Figure 5.2. The expression of steering angle *"θ_0"* in terms of time delay *"T_n"* and the separation *"d"* between the transmitting elements is given in (5.2) to (5.4), where *c* is the speed of electromagnetic wave in free space. The expression for relative steering delay "$\Delta T = T_{n-1} - T_n$" is given in (5.3). The required time delay for each transmitting node corresponding to the desired steering angle is derived from (5.2), and shown in (5.4). The term *"T_0"* is the offset delay for each transmitting node, which is the delay associated with the IR-UWB pulse *x(t)*. It is the same for all the transmitting nodes, hence it is neglected and taken as $T_0 = 0$ for further study.

$$\theta_0 = sin^{-1}\left(\frac{\Delta T \cdot c}{d}\right) \tag{5.2}$$

$$\Delta T = T_n - T_{n-1} = \frac{d}{c} sin\theta_0 \tag{5.3}$$

$$T_n = T_0 + (n - 1)\frac{d}{c} sin\theta_0 \tag{5.4}$$

The signal received at the far-field in the azimuthal direction θ ($-90^o < \theta < +90^o$) as illustrated in Figure 5.2., is $y(\theta,t)$ given in (5.5) to (5.7). The term τ_n is the spatial delay in the steered direction, which depends on the separation *"d"* between the transmitting sensor nodes. $G_A(\theta)$ is the azimuthal-angle dependent antenna gain of the transmitting sensor nodes.

$$y(\theta,t) = y_1(\theta,t) + y_2(\theta,t) + ... + y_N(\theta,t) \tag{5.5}$$

$$y(\theta,t) = G_A(\theta)\begin{bmatrix} x_1(t - T_1 - \tau_1) + x_2(t - T_2 - \tau_2) \\ + ... x_N(t - T_N - \tau_N) \end{bmatrix} \tag{5.6}$$

$$y(\theta,t) = G_A(\theta)\sum_{n=1}^{N} x_n(t - T_n - \tau_n) \tag{5.7}$$

A graphical illustration of the steering-time delays and delay due to path difference is shown in Figure 4.5. If the summation of tuned steering-delay *"T_n"* and the spatial-delay *"τ_n"* for each element becomes equal in the steered direction, all the transmitting pulses superimpose each other to form a strong beam in the steered direction, as shown in Figure 4.5. The spatial delay

for the n^{th} transmitting node is given in (5.9), where τ_0 is the constant spatial delay with a frame of reference and independent of θ. For simplicity, the value of $\tau_0 = 0$ is taken for further study.

$$\tau_n = \tau_0 - (n-1)\frac{d}{c}\sin\theta \tag{5.8}$$

$$y(\theta,t) = G_A(\theta)\sum_{n=1}^{N} x_n\left(t - (n-1)\frac{d}{c}(\sin\theta_0 - \sin\theta)\right) \tag{5.9}$$

The received pulse $y(\theta,t)$ in the far-field region is obtained by putting (5.8) and (5.4) into (5.7), which is given in (5.9). Assuming equal inter-antenna element separation *"d"* and transmitter beamforming network with equal relative steering-delay *"ΔT"*. The steering angle can be easily changed by changing the steering delay *"ΔT"* as shown in (5.2).

$$\theta_{Gm} = \sin^{-1}\left(\frac{\Delta T\ c}{d} - m\frac{c}{f_c d}\right); \quad -90° \le \theta_{Gm} \le +90° \tag{5.10}$$

The spatial summation of the multi-cycle IR-UWB pulse may produce multiple grating lobes if the separation *"d"* is larger than a wavelength, which is the case of collaborative beamforming. The number of grating lobes including the main beam will be equal to $(2G+1)$, where G is the integer part of d/λ. The steering angle of the multiple beams can be evaluated using (5.10) for $m = 0, \pm1, \pm2, \ldots \pm G$ [44]. It is important to note [from (5.9) and (5.10)] that the transmitted pulses are in phase in the grating lobes direction and hence interfere constructively. The constructive interference happened due to the linear inter-element spacing between the nodes. However, in case of collaborative virtual array formation the inter-element spacing is flexible to adjustment. This gives a motivation for a non-linear array formation,

which is capable of providing constructive interference in steered direction otherwise destructive interference takes place. In this chapter, the non-linear collaborative arrays are proposed, which can produce one steering transmitting beam despite inter-element spacing greater than a wavelength.

5.2.1 Proposed Array and Simulation

Assume an array with arbitrary separation between the nodes and steering angle $\theta_0 = 0$, i.e. ($\Delta T = 0$). The transmitted IR-UWB pulse *"$x_1(t)$"* from the first transmitter and received at the receiver in far-field *"$y_1(\theta,t)$"* is derived using (5.1) and (5.9), which is given in (5.11). Assuming an omni-directional antenna $G_A(\theta)=1$ and neglecting the range dependent propagation loss and delay. The N^{th} transmitter pulse received at the receiver is given in (5.12). Similarly, in the case of four transmitter nodes, the received pulse corresponding to the second, third and fourth nodes are given in (5.13) to (5.15), respectively.

$$y_1(\theta,t) = Ae^{-K(t+k_1T_s)^2} \cos 2\pi f_C(t+k_1T_s) \tag{5.11}$$

$$y_N(\theta,t) = Ae^{-K(t+[k_1+k_2+.....+k_N]T_s)^2} \cos 2\pi f_C(t+[k_1+k_2+.....+k_N]T_s) \tag{5.12}$$

$$y_2(\theta,t) = Ae^{-K(t+[k_1+k_2]T_s)^2} \cos 2\pi f_C(t+[k_1+k_2]T_s) \tag{5.13}$$

$$y_3(\theta,t) = Ae^{-K(t+[k_1+k_2+k_3]T_s)^2} \cos 2\pi f_C(t+[k_1+k_2+k_3]T_s) \tag{5.14}$$

$$y_4(\theta,t) = Ae^{-K(t+[k_1+k_2+k_3+k_4]T_s)^2} \cos 2\pi f_C(t+[k_1+k_2+k_3+k_4]T_s) \tag{5.15}$$

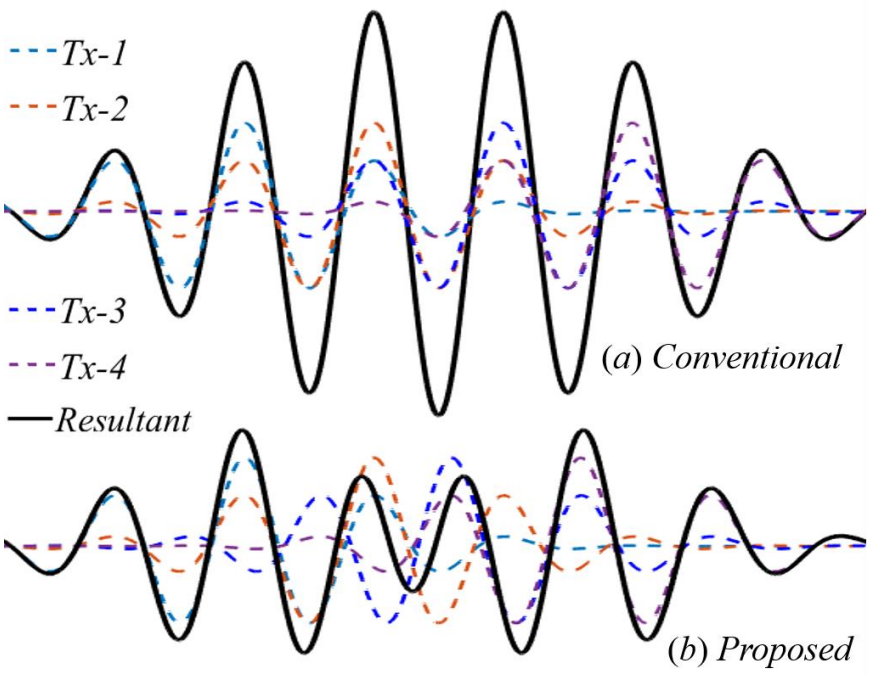

Figure 5.3. Interference of pulses (dashed) and resultant received pulse (solid) at the first grating lobe in case of (*a*) a conventional as well as (*b*) the proposed array with the same scale.

where, $A = 1/\sigma\sqrt{(2\pi)}$, $K = 1/2\sigma^2$, and k_1 to k_N is the spatial-time scaling factor, whose values depend on the separation between the consecutive elements and given by $k_p = d_{opt}/d$, $p = 1, 2, 3, \ldots N$, where d_{opt} is the optimized separation of the proposed array and d is the separation of the conventional linear array. T_s is the relative spatial-time delay given by $T_s = (d \sin\theta)/c$. At the first grating lobe, T_s will be equal to the fundamental time period of sinusoidal frequency, $T = 1/f_c = (d \sin\theta_{G1})/c = T_s|_{\theta=\theta_{G1}}$. There are two terms in (5.11) to (5.15), one is exponentially

decaying, which controls the amplitude and the other is cosine, which tunes the relative spatial-time delay of the transmitted pulse. The spatial-time scaling factor *"k_p"* is used for tuning the relative spatial-time delay of the transmitted pulse for constructive and destructive interferences. In the case of 4-element conventional array, $k_1 = 0$ and $k_2 = k_3 = k_4 = 1$; which provide a spatial-time delay in terms of an integer multiple of *T* at first grating lobe. Hence, the transmitted pulses will add constructively to form a strong grating lobe radiation. The transmitter pulses at the first grating lobe evaluated using (5.11) to (5.15) are shown in Figure 5.3 together with the resultant received pulse.

It is observed that the third and the fourth peaks of the resultant received pulse for the conventional array have dominant amplitudes. The third peak of the resultant received pulse mainly consists of the sum of first, second and third transmitter pulses and the fourth peak mainly the summation of second, third and fourth transmitter pulses. This suggests that the dominant peaks of the resultant received pulse can be reduced if the first and second as well as third and fourth transmitter pulses are in-phase with each other, whereas the second and third transmitter pulses are out of phase. This condition will lead to destructive interfere and minimize the radiation at grating lobes.

This motivates two ways to reduce the array grating lobes intensity. In the first approach, the separation between first and second as well as third and fourth transmitting element is kept fixed ($k_1=0$, $k_2=k_4=1$) as the conventional array. The separation between second and third elements varies to get out of phase ($k_3=0.5$). In the second approach, the separation between the second and third elements is kept the same as the conventional array ($k_3=1$). The separation between first and second as well as third and fourth element varies identically to make the spatial-time delay between second and third elements out of phase ($k_1=0$, $k_2=k_4=1/0.5=2$). The array size for the second approach will be larger as compared to the first approach. Therefore,

in the proposed array, the first approach is chosen for experimental test convenience to fulfil far-field distance condition. The value of time scaling factor *"k_3=0.5"* reduces the intensity at grating lobes, however, it inevitably produces another side lobe (corresponding to an additional spatial delay of approximately ±*0.2T*) as shown in Figure 5.4 (black trace).

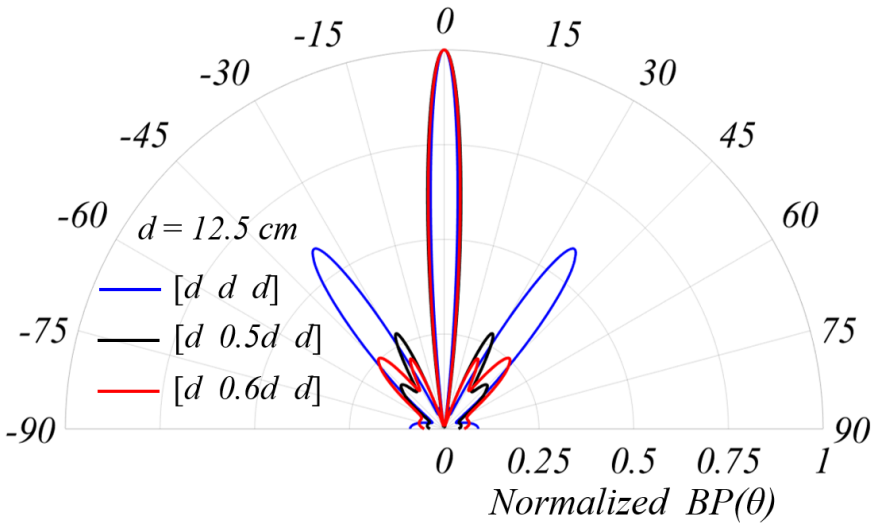

Figure 5.4. Normalized radiation pattern for N = 4, d = 12.5 *cm* of arrays [*d d d*] (blue), [*d 0.5d d*] (black), [*d 0.6d d*] (red).

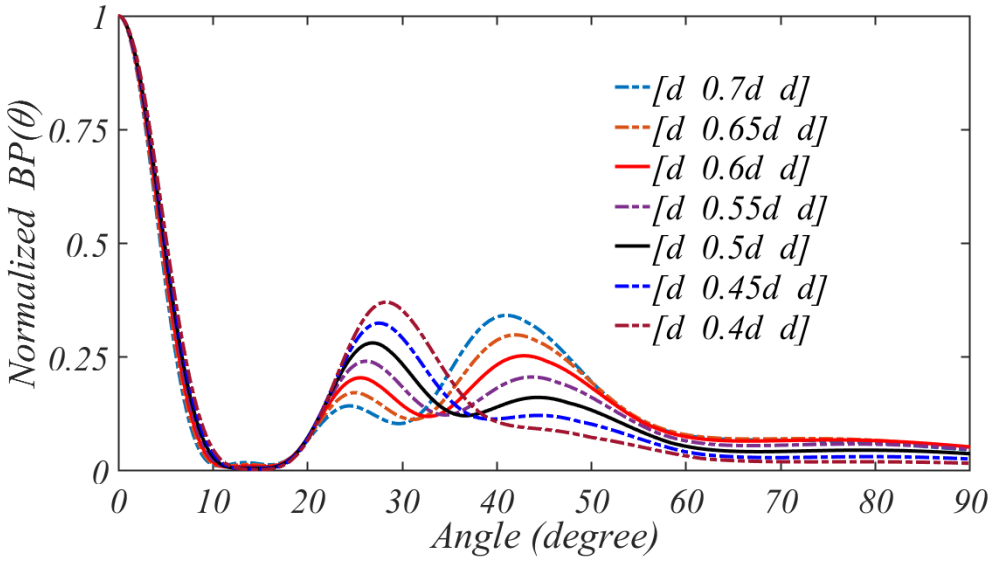

Figure 5.5. Normalized radiation pattern of arrays with N = 4 for different array combinations indicated in legend.

The radiation intensity in the first side lobe (corresponding to *+0.2T*) should be as low as possible for better deployment of radar array. In order to reduce the radiation intensity along the first side lobe, the relative spatial-time delay between the second and third pulse is optimized to [*T/2+(0.2T)/2 = 0.6T*, which corresponds to *"k_3=0.6"*]. The simulated normalized radiation pattern for a different iterative combination of a symmetrical array is shown in Figure 5.5. This optimized array [*d 0.6d d*] significantly minimizes the first side lobes at the expense of the second side lobes as shown in Figure 5.5 (solid red trace). The received time-domain pulses from each of the transmitter nodes (optimized array) at the first grating lobe (corresponding to the conventional array) are shown in Figure 5.4 for comparison with the conventional array.

Table 5.1. Proposed Separation Between Transmitting Nodes of the IR-UWB Transmitter Array

N	***d_2***	***d_3***	***d_4***	***d_5***	***d_6***	***d_7***
4	*d*	*0.6d*	*d*			
5	*d*	*0.6d*	*0.6d*	*d*		
6	*d*	*0.6d*	*0.36d*	*0.6d*	*d*	
7	*d*	*0.6d*	*0.36d*	*0.36d*	*0.6d*	*d*

Note: d = inter-element separation of the conventional linear array
d_1 = 0 = position of the first node, which is assumed to be origin in the analysis.

Table 5.2. Proposed Separation Between Transmitting Nodes of the IR-UWB Transmitter Array

N	***d_2***	***d_3***	***d_4***	***d_5***	***d_6***	***d_7***
4	*1.67d*	*d*	*1.67d*			
5	*1.67d*	*d*	*d*	*1.67d*		
6	*2.77d*	*1.67d*	*d*	*1.67d*	*2.77d*	
7	*2.77d*	*1.67d*	*d*	*d*	*1.67d*	*2.77d*

Note: d = inter-element separation of the conventional linear array
d_1 = 0 = position of the first node, which is assumed to be origin in the analysis.

In general, for *N* number of transmitting nodes, there are two possible algorithms for grating lobes suppression. First, select the middle separation of the array and divide it every time by a factor of *0.6* to get the subsequent separation in both directions. Second, select the corner separation at both ends and multiply by a factor of *0.6* to get the subsequent separation from both corners. It is important to note that the nonlinear distribution of nodes is symmetric about the middle point of the array, which reduces complexity for steering the beam. The proposed inter-element separation between the transmitting nodes for both the approaches is tabulated in Table 5.1 and Table 5.2 for different number of nodes.

The reception technique plays an important role while detecting time-of-arrival and time-of-flight in the IR-UWB system [151]. The beam pattern of the transmitter array can be obtained in several ways, four definitions of beam pattern are given in (5.16) to (5.19).

$$BP(\theta)\big|_{\phi=90^\circ} = \frac{\left|y(\theta,t)\right|_{max}}{\left|x(t)\right|_{max}} \tag{5.16}$$

$$BP(\theta)\big|_{\phi=90^0} = \frac{\left|y(\theta,t)_{p-p}\right|}{\left|y(\theta,t)_{p-p}\right|_{\max}} \tag{5.17}$$

$$BP(\theta)\big|_{\phi=90^\circ} = max\left(\int_{-\infty}^{+\infty}\left|y(\theta,t)\right|^2 dt\right) \tag{5.18}$$

$$BP(\theta)\big|_{\substack{\phi=90^o \\ (x-z\ \ plane)}} = max\left(\int_{t-T_p/2}^{t+T_p/2}\left|y(\theta,t)\right|^2 dt\right) \tag{5.19}$$

The beam pattern based on the maximum received amplitude normalized with the transmitted amplitude is given in (5.16). Since the spatial interference of IR-UWB pulses at some observation angle θ may produce dominant positive peak values and at another angle it may produce dominant negative peak values. Therefore, the beam-pattern based on normalized peak may produce an incorrect radiation pattern. This problem can be solved by observing the peak-to-peak amplitude of the received pulse. The radiation pattern based on the normalized peak-to-peak amplitude is given in (5.17). The system requirement for detecting the peak-to-peak amplitude value with fine time-domain data points increases the overall system complexity and power consumption. The beam-pattern based on normalized energy over infinite time is shown in (5.18). This approach reduces the complexity and power consumption. However, infinite time integration window renders incorrect detection of the direct path time-of-arrival and time-of-flight due to the presence of multipath within an indoor environment. Hence, the detection technique shown in (5.18) is suitable for data communication but not for indoor positioning or radar communication. Therefore, an energy detector with the integration time window same as the transmitted pulse width is chosen in the receiver for the evaluation of beam peak of radiation pattern. The expression for the proposed array azimuth radiation pattern BP is shown in (5.19), where T_p is the time pulse width of the transmitted Gaussian-shape IR-UWB pulse, which is the full width at tenth maxima (FWTM) [117].

The simulation of the transmitter arrays with different spacing and the different number of transmitting nodes is carried out in MATLAB. The simulated radiation pattern of the conventional array for $N = 4$, $d = [12.5, 12.5, 12.5]$ *cm* and the optimized array for $N = 4$, $d = [12.5, 7.5, 12.5]$ *cm* is plotted in Figure 5.4. It can be noticed from Figure 5.4, that the grating lobes radiation of the proposed array is effectively reduced.

In practical situations, the typical spacing between the wireless sensor nodes of the collaborative virtual transmitter array should be in meters. In order to see the applicability of the proposed array, the radiation pattern corresponding to $N = 4$, $d = [167, 100, 167]$ *cm* with the radiation pattern corresponding to $N = 4$, $d = [12.5, 7.5, 12.5]$ *cm* is plotted in Figure 5.6.

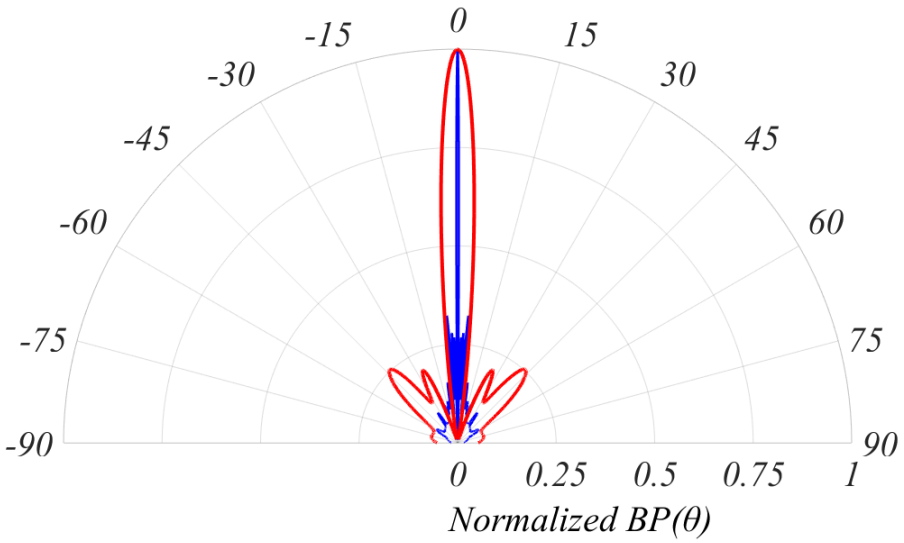

Figure 5.6. Radiation patterns of a proposed array ($N = 4$, $d = 12.5$ *cm*, Red) and practically viable array ($d = 167$ *cm*, $N = 4$ according to Table 5.1, Blue)

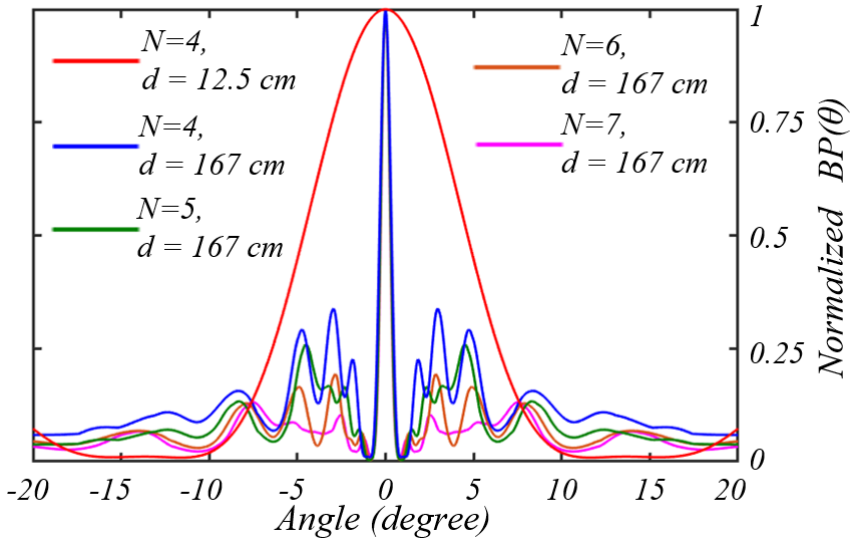

Figure 5.7. Magnified radiation patterns of a proposed array ($N = 4$, $d = 12.5$ cm) and practically viable array ($d = 167$ cm and $N = 4, 5, 6, 7$ according to Table 5.1)

The beam-width is significantly reduced, which is beneficial. However, it is important to note that the grating lobes' radiation intensity is still in the same order as the array with smaller separation shown in Figure 5.5. Hence, the proposed array can produce only one beam with a significantly larger separation between the nodes depending upon the application requirements. In addition to this, the radiation of minor lobes can be effectively suppressed by increasing the number of collaborative nodes in the virtual array. The magnified radiation pattern of the arrays with $d = 167\ cm$ for $N = 4, 5, 6,$ and 7 according to Table 5.1 are plotted in Figure 5.7. The minor lobes reduction of 9 *dB* for $N = 7$ is achieved in simulation. This is best possible for the symmetric array with 7 elements, which is verified by several Monte Carlo simulations.

5.2.2 Error Analysis

In a practical scenario, the position of autonomous sensor nodes will have positioning error during formation of the collaborative array. The positioning error will distort beam-pattern of the proposed collaborative array. Hence, an error analysis is performed to see the effect of change in position of nodes and jitter in steering delay. The mathematical models are derived for different cases. In the first case, the tag position is incorporated with the positioning error "Δx" in *x-axis* as shown in Figure 5.8. The spatial delay τ_n, in this case, is given in (5.20), which is derived from (5.8) with $\tau_0 = 0$. Consequently, the received pulse in the far-field is derived in (5.21) using (5.7) and (5.20). In the second case, a positioning error of "Δz" in the *z-axis* is incorporated as shown in Figure 5.9. The spatial delay τ_n for this case is given in (5.22) and the corresponding received pulse in the field is derived in (5.23) using (5.22) and (5.7). In the third case, an error range circle is assumed, and an arbitrary point is taken, which has *x-axis* error component of "Δx" and *z-axis* error component of "Δz" as shown in Figure 5.10. The spatial delay τ_n for this case will have *x-axis* and *z-axis* error component as shown in (5.24). The

resultant received pulse in far-field for this case is derived in (5.25) using (5.24) and (5.7). Since the height of the sensor nodes for a particular case will be fixed, the variation in *y*-axis is neglected for the error analysis. The other factor which can distort the beam pattern of a virtual array is the jitter "ΔJ_T" in steering delay. The mathematical model incorporated with jitter in steering delay and position error of nodes is given in (5.26).

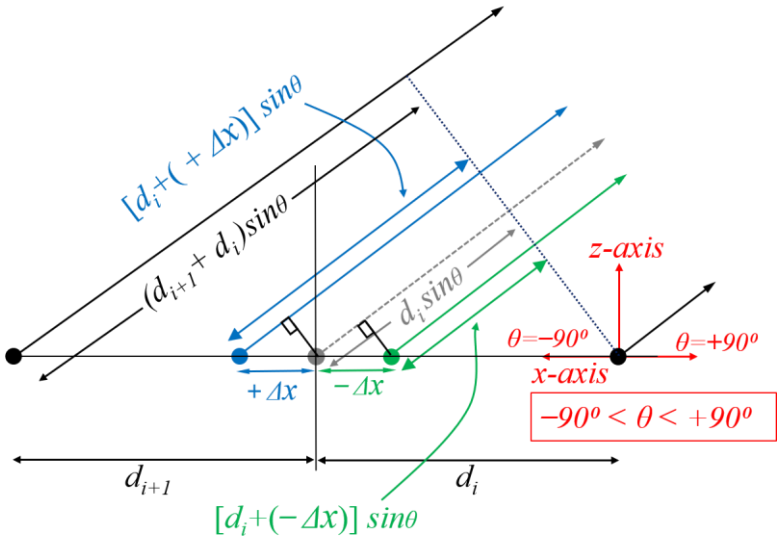

Figure 5.8. Effect on beamforming due to the positioning error in the *x-axis*

$$\tau_n = -\left[\left(\sum_{i=1}^{n} d_i\right) + (\Delta x)\right]\frac{\sin\theta}{c} \tag{5.20}$$

$$y(\theta,t) = G_A(\theta)\sum_{n=1}^{N} x_n\left(t - T_n + \left[\left(\sum_{i=1}^{n} d_i\right) + (\Delta x)\right]\frac{\sin\theta}{c}\right) \tag{5.21}$$

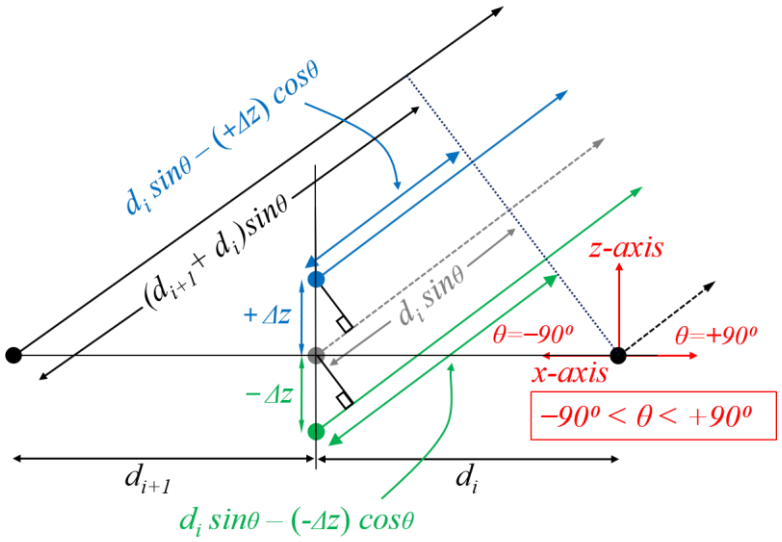

Figure 5.9. Effect on beamforming due to the positioning error in the *z-axis*

$$\tau_n = -\left[\left(\sum_{i=1}^{n} d_i\right)\frac{\sin\theta}{c} - (\Delta z)\frac{\cos\theta}{c}\right] \tag{5.22}$$

$$y(\theta,t) = G_A(\theta)\sum_{n=1}^{N} x_n\left(t - T_n + \left[\left(\sum_{i=1}^{n} d_i\right)\frac{\sin\theta}{c} - (\Delta z)\frac{\cos\theta}{c}\right]\right) \tag{5.23}$$

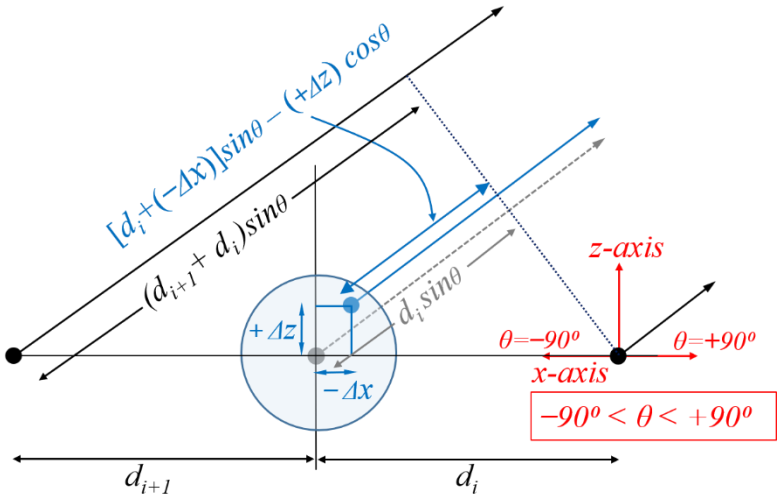

Figure 5.10. Effect on beamforming due to a radial positioning error having *x-axis* and *z-axis* error components

$$\tau_n = -\left[\left(\left(\sum_{i=1}^{n} d_i\right)+(\Delta x)\right)\frac{\sin\theta}{c}-(\Delta z)\frac{\cos\theta}{c}\right] \tag{5.24}$$

$$y(\theta,t) = G_A(\theta)\sum_{n=1}^{N} x_n\left(t-T_n+\left[\left(\left(\sum_{i=1}^{n} d_i\right)+(\Delta x)\right)\frac{\sin\theta}{c}-(\Delta z)\frac{\cos\theta}{c}\right]\right) \tag{5.25}$$

$$y(\theta,t) = G_A(\theta)\sum_{n=1}^{N} x_n\left(\begin{array}{l} t-\left(T_n+\Delta J_T\right)+ \\ \left[\left(\left(\sum_{i=1}^{n} d_i\right)+(\Delta x)\right)\frac{\sin\theta}{c}-(\Delta z)\frac{\cos\theta}{c}\right] \end{array}\right) \tag{5.26}$$

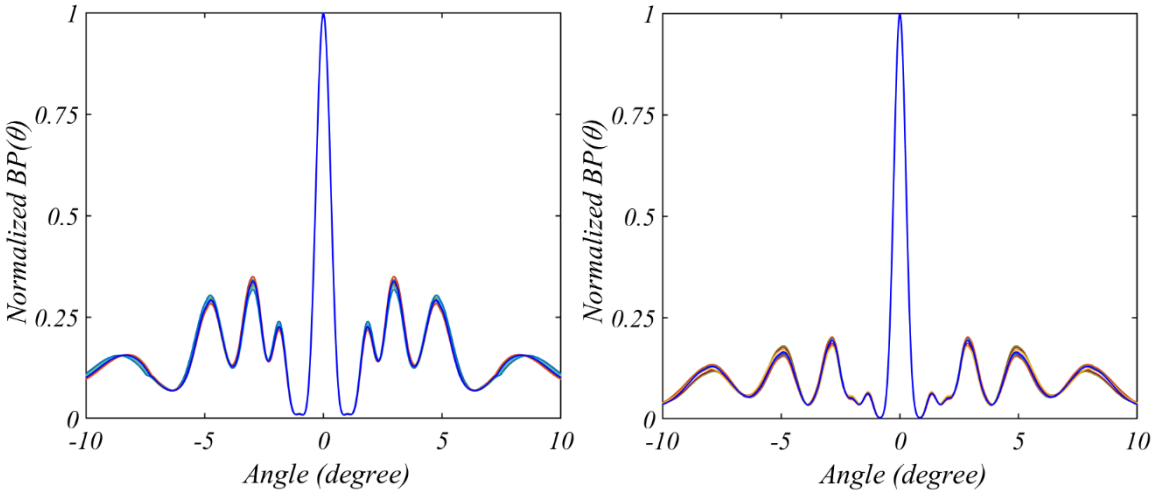

Figure 5.11. The radiation pattern plot of an array with random variation of *"Δx"* for $N = 4$ and $N = 6$.

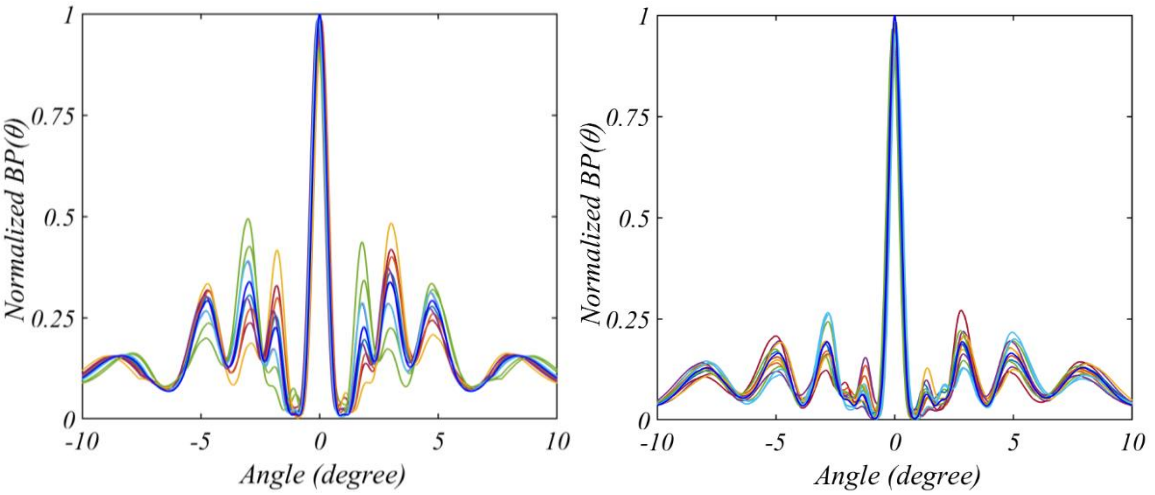

Figure 5.12. The radiation pattern plot of an array with random variation of *"Δz"* for $N = 4$ and $N = 6$.

The peer-to-peer positioning range accuracy is usually 1 *cm* to 2 *cm* for short-range systems. Therefore, the value of *"Δx"* is taken as a random variable with standard deviation of 4 *cm* (greater than λ/2) and incorporated in (5.21). The random variable with standard variable of 4 *cm* is taken to see the maximum effect. The radiation pattern corresponding to (5.21) is plotted in Figure 5.11 using (5.19). It can be observed that variation in *x*-axis has insignificant effect

on the beam pattern of the array. Similarly, the value of *"Δz"* is taken as a random variable with standard deviation of 2 *cm* (greater than λ/4) and incorporated in (5.23). The radiation pattern corresponding to (5.23) is plotted in Figure 5.12 using (5.19). It can be observed that variation in *z*-axis is comparatively more effective than the variation in *x*-axis on the beam pattern of the array. Similarly, a random variable of *"ΔJ_T"* with standard deviation of 20 *ps* is taken in (5.26) with *"Δx=0"* and *"Δz= 0"*. The corresponding radiation pattern is shown in Figure 5.13. The overall effect of variation in *x*-axis, *z*-axis and jitter in synchronization clock are taken together in (5.26) and the radiation pattern is plotted in Figure 5.14 for $N = 4$ and in Figure 5.15 for $N = 6$. It can be observed from all the plotted Figures that the effect of even extreme error conditions is within tolerable range. Moreover, increasing the number of nodes from 4 to 6 in the array significantly enhances the performance.

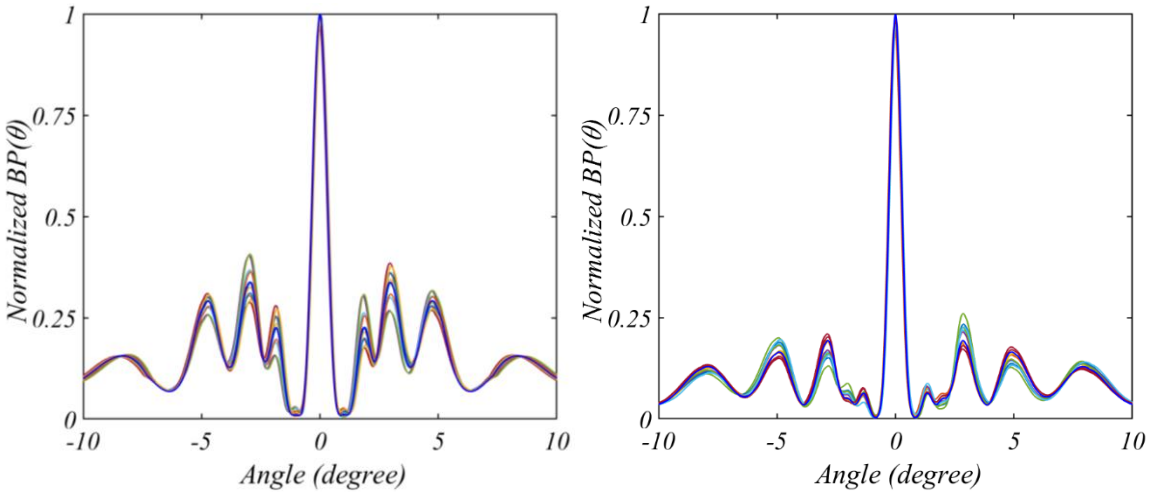

Figure 5.13. Radiation pattern plot of an array with random variation of *"ΔJ_T"* for $N = 4$ and $N = 6$.

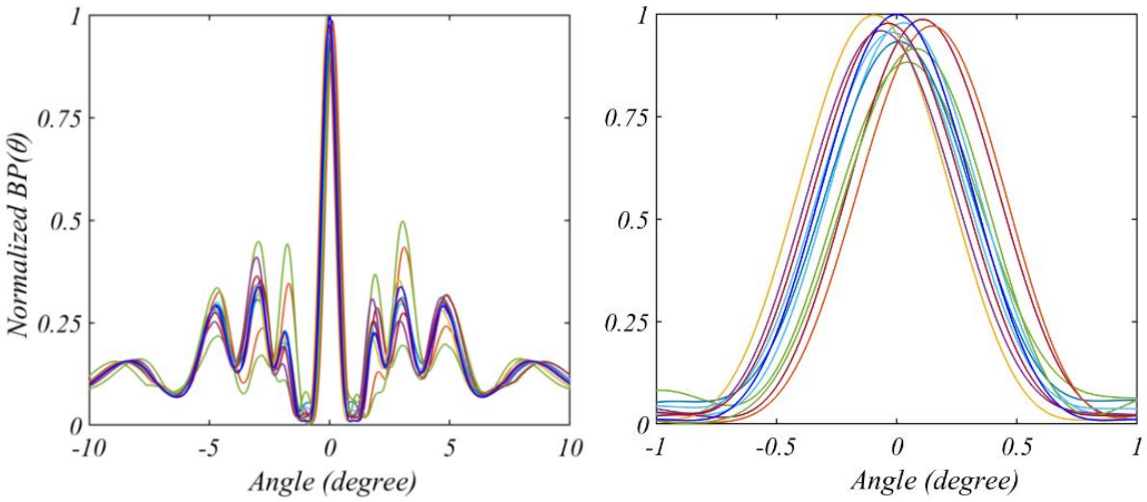

Figure 5.14. Radiation pattern plot of an array with random variation of *"Δx", "Δz", "ΔJ_T"* for $N = 4$.

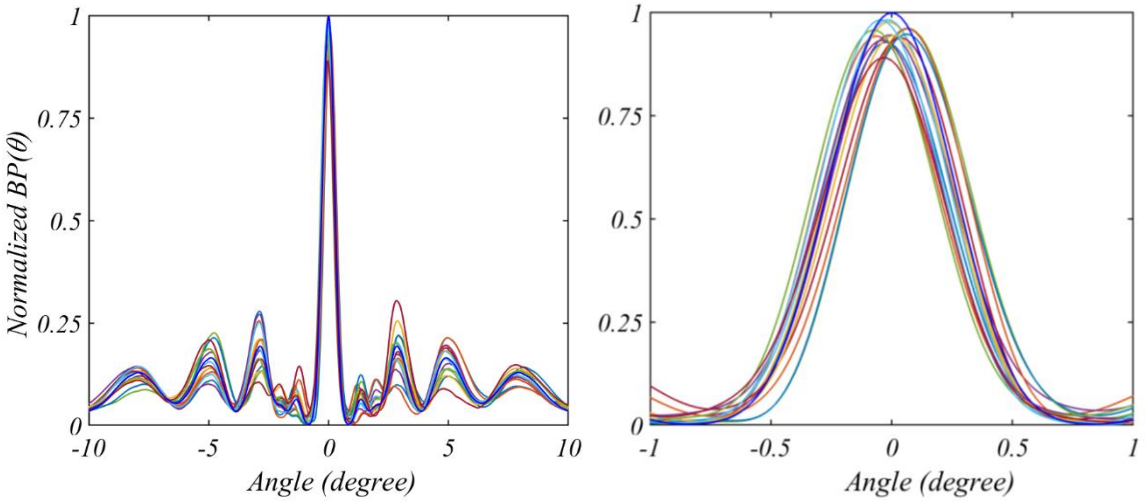

Figure 5.15. Radiation pattern plot of an array with random variation of *"Δx", "Δz", "ΔJ_T"* for $N = 6$.

5.3 Measurement Results and Discussion

The schematic of the measurement setup (*x*-*z* plane) with the transmitter array and the receiving section is shown in Figure 5.16. A low noise amplifier (LNA) and a band-pass filter (BPF) are adopted in the front-end of the receiver section to minimize the noise power level. The mathematical operation after the IR-UWB pulse reception is shown inside the high-frequency oscilloscope (*Agilent Infiniium DSO81204B*) block of Figure 5.16. The Low Pass Filter (LPF) inside the oscilloscope is tuned to 3*dB* bandwidth of 1 *GHz* and a rise-time of 350 *ps* for all the measurements. The measured IR-UWB pulse compared with a pulse in the simulation from (5.1) and IR-UWB pulse generator board (detailed in chapter 3) is shown in Figure 5.17. The UWB patch antenna along with the measured and simulated time-domain radiation pattern in the azimuth plane is shown in Figure 5.18. In order to get the time-domain radiation pattern of the antenna element, the IR-UWB pulse is fed through the antenna and received by another identical antenna placed in the far-field. The received pulse peak-power calculated from (5.19) and Friis equation are used to obtain the gain of the antenna. The gain of the antenna is plotted in *dBi* (decibels relative to an isotropic radiator). The design parameters and frequency-dependent characteristics of the adopted antenna can be found in [150].

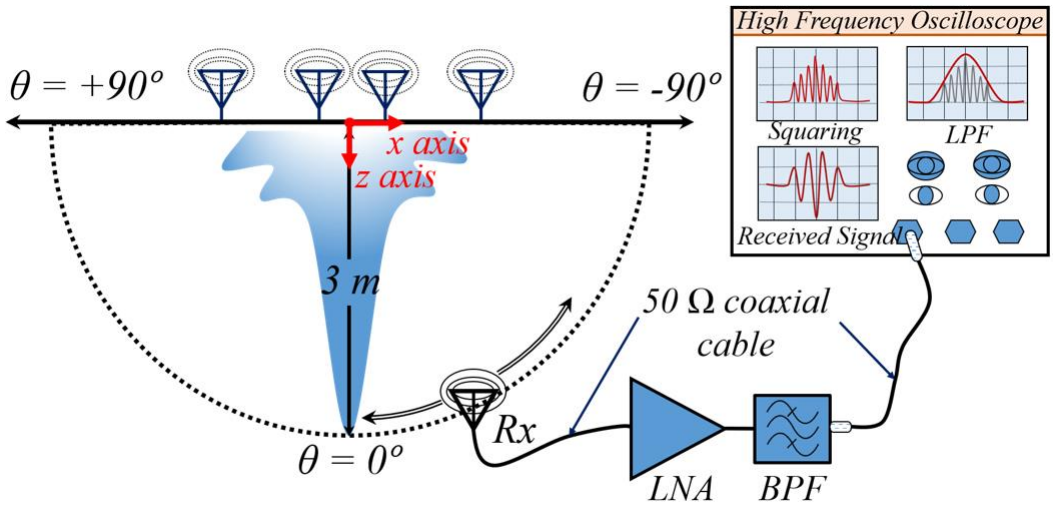

Figure 5.16. Schematic representation of the measurement setup showing the mathematical operations in the high-frequency oscilloscope block.

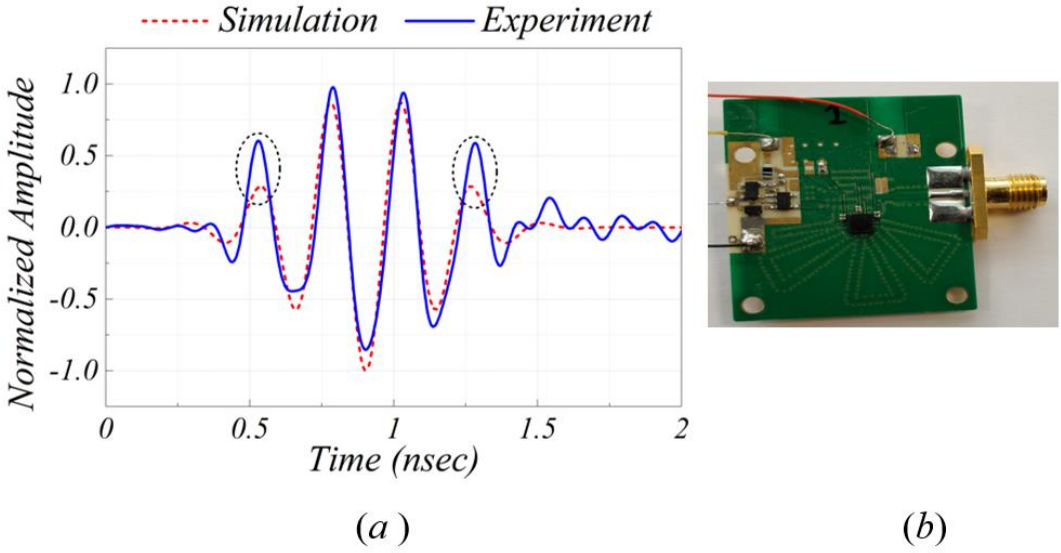

Figure 5.17. (*a*) Comparison between the IR-UWB pulse from simulation and measurement and (*b*) The IR-UWB pulse generator board used in experiments

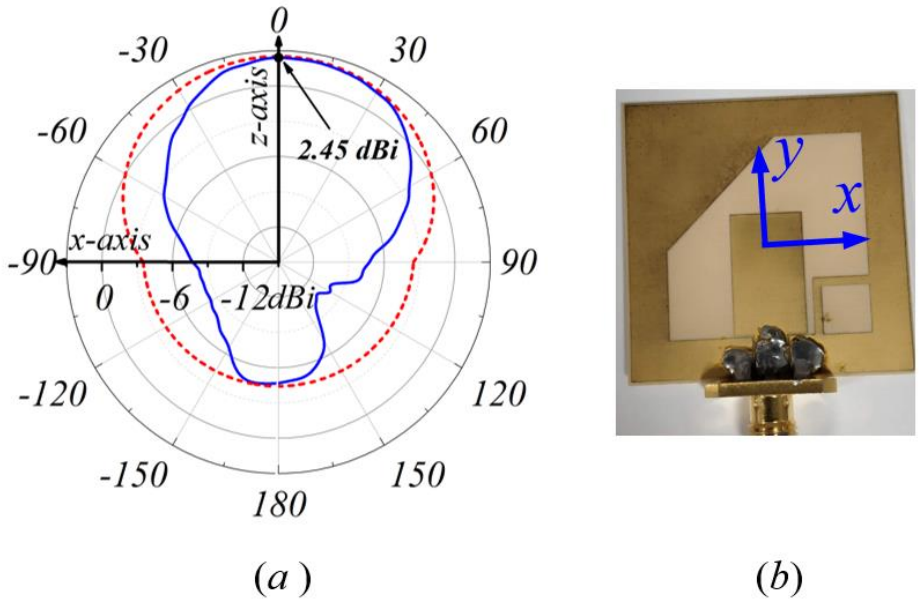

Figure 5.18. (*a*) Comparison between the gain of the antenna in simulation and measurement (*b*) UWB patch antenna used in the experiments.

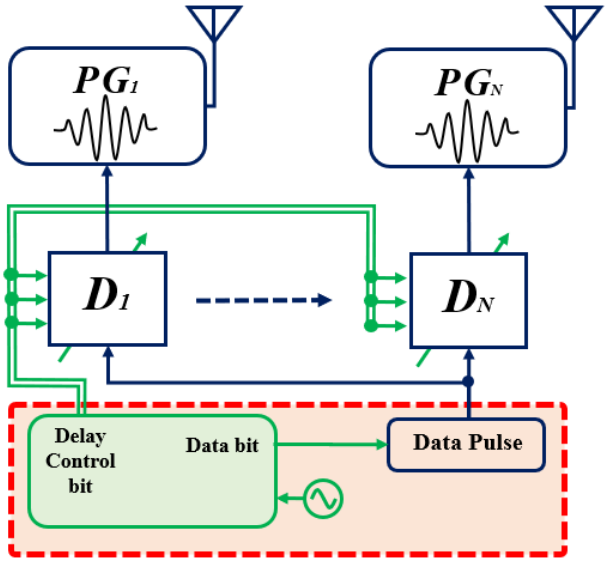

Figure 5.19. Architecture of the beamforming network for radiation pattern measurements

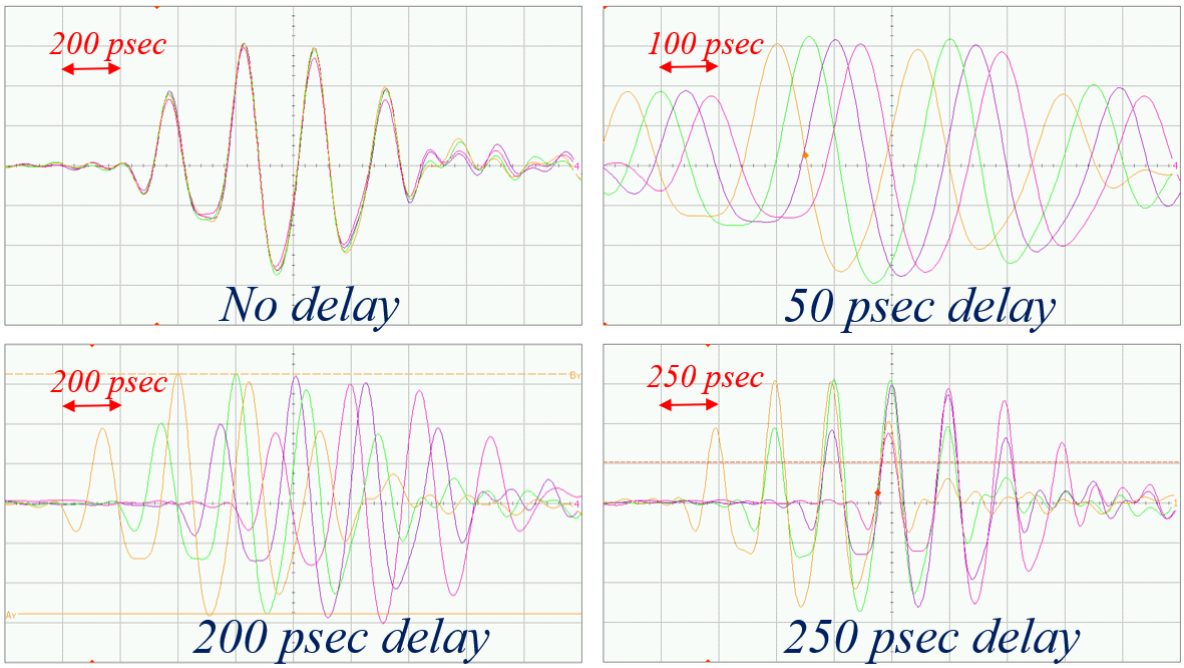

Figure 5.20. Recorded four-channel transmitted signals directly fed from the IR-UWB pulse generator board to an oscilloscope, calibrated with no delay (top), 50 *ps* relative delays (bottom).

The architecture of the beamforming network for radiation pattern measurements is shown in Figure 5.19. Digitally controlled delay cell *"D"* is used to delay the data pulse before entering the IR-UWB pulse generator *"PG"*. The baseband block in the red dashed rectangle is taken from the same board for all transmitting nodes for perfect synchronization assumption. However, for collaborative nodes, this block will be attached to each node separately and synchronized wirelessly to each other, which is not in the scope of this thesis. A commercially available digital delay IC (*SY100EP195V*) is used to implement D_1 to D_N blocks as shown in Figure 5.19, which provides the required steering delay. At first, the delay cells are calibrated to eliminate the delay offset. After offsetting, the transmitter array channels [output of *PG* blocks in Figure 5.19] are directly fed to the oscilloscope through 50Ω coaxial cable. Four-channel transmitter pulses are recorded after offsetting the delay and with 50 *ps*, 200 *ps*, 250 *ps* relative steering delays between the transmitter pulses shown in Figure 5.20. The calibrated IR-UWB pulse is then fed through a UWB antenna array with the proposed separation (as in

Table 5.1) for the radiation pattern measurement as shown in Figure 5.21. The proposed array is scalable for lower as well as larger separation, as explained in Section 5.2. Hence, two arrays are scaled down for the measurement to minimize the far-field distance. All the measurements are done at a receiver distance of 3 meters, which is the maximum possible disctance in the current laboratory conditions.

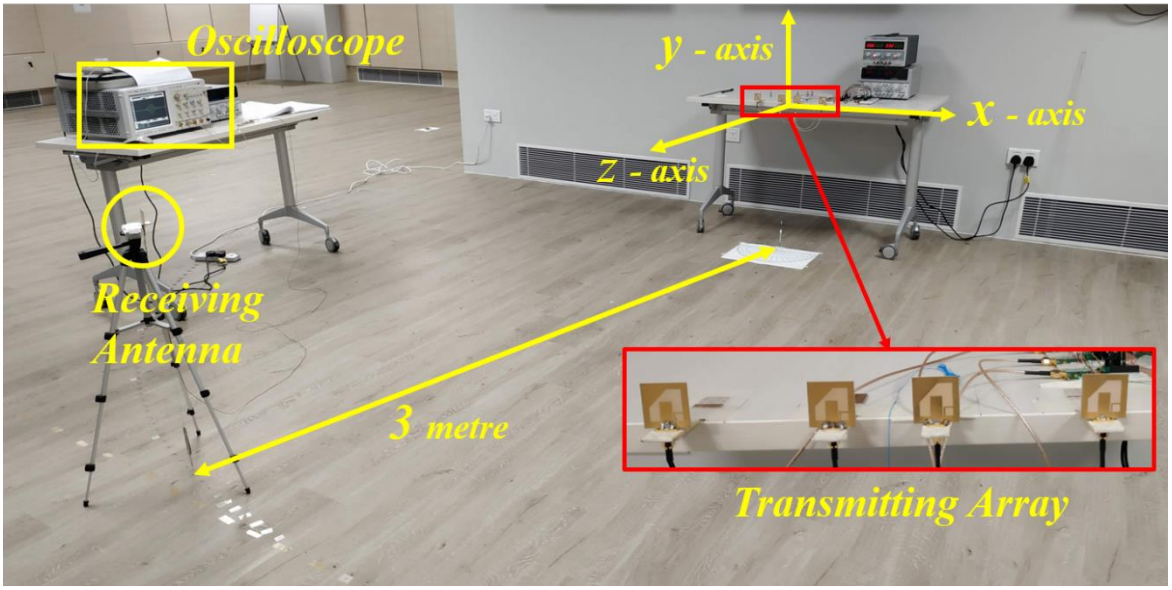

Figure 5.21. Actual measurement setup in the open environment

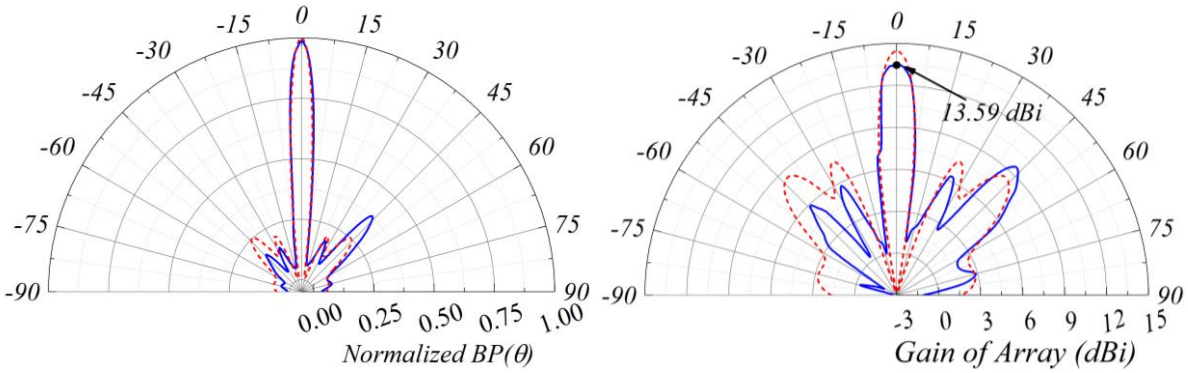

(*a*) (*b*)

Figure 5.22. Measured (solid blue) compared with simulated (dotted red) radiation pattern of the transmitter array N = 4, d = [12.5, 7.5, 12.5] *cm* steered at 0º (a) Normalized *BP(θ)* and (b) Gain of array in *dBi*

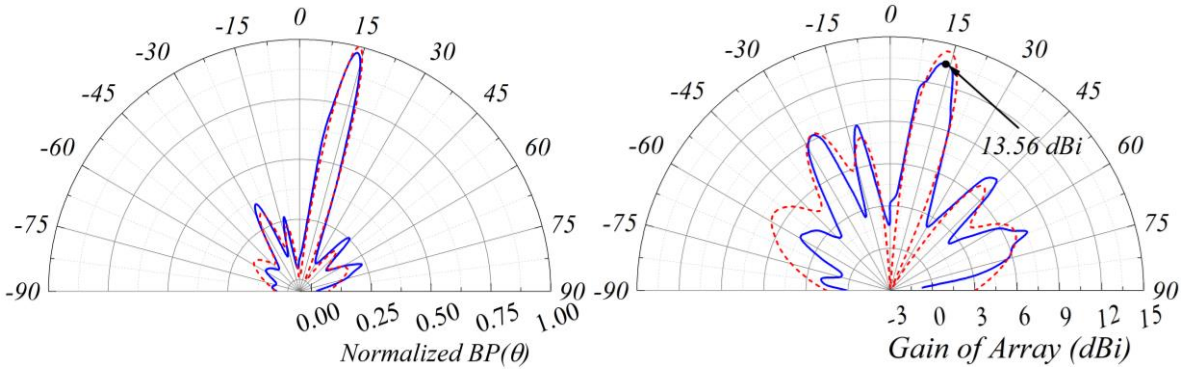

(*a*) (*b*)

Figure 5.23. Measured (solid blue) compared with simulated (dotted red) radiation pattern of the transmitter array N = 4, d = [12.5, 7.5, 12.5] *cm* steered at 14º (a) Normalized *BP(θ)* and (b) Gain of array in *dBi*

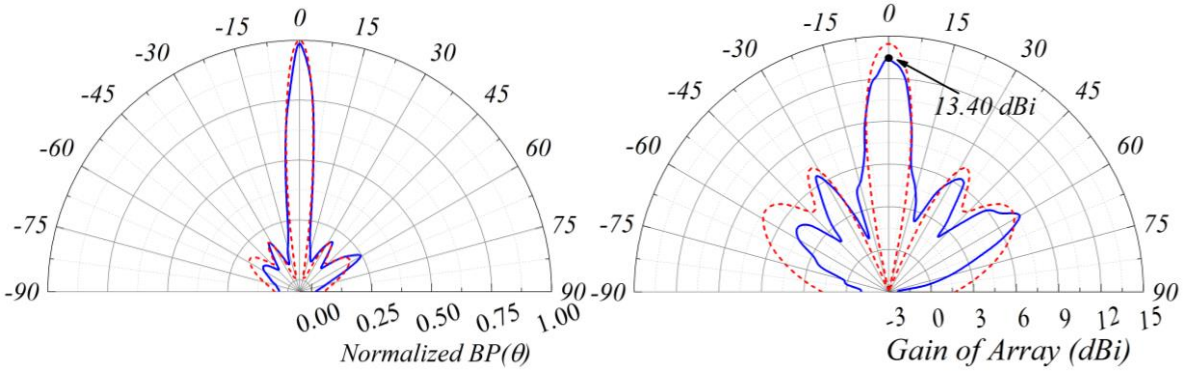

(*a*) (*b*)

Figure 5.24. Measured (solid blue) compared with simulated (dotted red) radiation pattern of the transmitter array N = 4, d = [10, 6, 10] *cm* steered at 0º (a) Normalized *BP(θ)* and (b) Gain of array in *dBi*

The measured radiation pattern compared with the simulated radiation pattern corresponding to the array N = 4, d = [12.5, 7.5, 12.5] *cm* steered at 0º is shown in Figure 5.22 and steered at 14º is shown in Figure 5.23. The radiation pattern for the array N = 4, d = [10, 6,

10] *cm* steered at 0º is shown in Figure 5.24. In Figure 5.22 to Figure 5.24, the radiation at some angles differs from the simulated results. This is mainly due to the difference in simulated and measured antenna gain plots, as shown in Figure 5.18. In addition, the magnitude of the first and fourth positive peak of the actual IR-UWB pulse [Figure 5.17.] is larger than the IR-UWB pulse used in the array simulation. The minor lobes suppression of 6 *dB* is achieved in the measurement results [Figure 5.24]. However, in the worst condition, the suppression of 4.25 *dB* appears in the measurements. The minor lobes suppression can be reduced further by increasing the number of transmitting nodes in the array. The gain of the transmitter array with $N = 4$ is expected to increase by $20log_{10}(N) = +12$ *dB*, which will maximize to 12 + 2.45 = 14.45 *dBi*. The measured array gain is around 13.5 *dBi* demonstrating an efficiency of 80%.

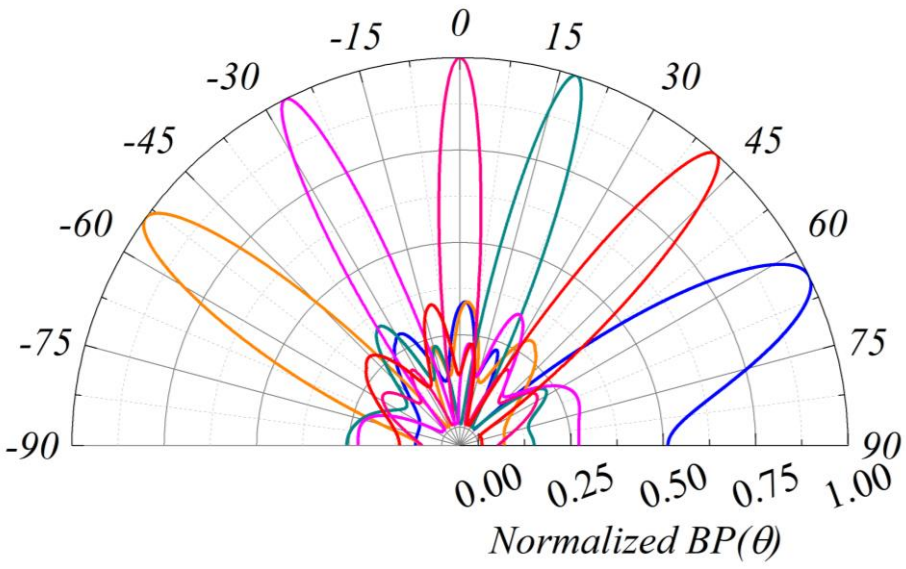

Figure 5.25. The normalized simulated radiation pattern of the transmitter array $N = 4$, $d = [10, 6, 10]$ *cm* steered at different steering angle.

The simulated radiation pattern steered at a different angle is shown in Figure 5.25. The results clearly show that the proposed array can scan up to 60º without significant change in

beamwidth. A brief comparison of specifications and results in the simulations and the experiments are tabulated in Table 2.

Table 5.3. Comparison of specification and results in the simulation and experiments

Parameters	**Simulation**	**Experiment**
Jitter in ΔT	0 *ps*	±20 *ps*
Change in *d*	0 *cm*	± 0.25 *cm*
$BP(\theta)\|_{\phi=90^o}$	--	Compared in Figure 5.18(*b*)
θ_0 deviation	0º	± 2.5º
Array gain	14.5 *dBi*	~13.5 *dBi*
Array efficiency	100%	80%

5.4 Chapter Conclusion

The proposed algorithm for the separation between the transmitting nodes is simulated and demonstrated. The results for the different cases of a collaborative virtual array are analyzed and optimized for better performance. The proposed algorithm is implemented to verify the radiation pattern of the transmitter array. A prototype is developed using true-time delay cells, IR-UWB pulse generator and a UWB antenna. Delay calibration of the true-time delay cell is performed for beam steering. Two different transmitter arrays are scaled-down and optimized for the measurement. The minor lobe suppression of 6 *dB* is achieved for the array $N = 4$, $d =$ [10, 6, 10] *cm* steered at 0º. In the worst condition, a suppression of 4.25 *dB* is achieved for the array $N = 4$, $d =$ [12.5, 7.5, 12.5] *cm* steered at 0º and 14º. The 4-element array achieves 13.5 *dBi* gain and 80% efficiency.

Chapter – 6

Conclusions and Recommendations

In this chapter, the conclusions and recommendations for future work are provided. In this thesis, three main contributions are presented. The first contribution is the design of an IR-UWB pulse generator Monolithic Microwave Integrated Circuit, which can generate the highest possible voltage IR-UWB pulse in the 3-5 GHz frequency band. In the second contribution, a multi-beam IR-UWB array configuration is proposed for accurate indoor positioning and tracking application utilizing the GDOP techniques. In the third contribution, an algorithm for non-linear collaborative array configuration is proposed, which can collaboratively align and point a single beam radiation pattern despite spacing between them being larger than one wavelength. The authors of the thesis also recommending some future work, which can use the outcome of this thesis and further improve the performance of the system.

6.1 Major Conclusions

The major conclusions of the thesis extracted from the literature review, proposed work, conducted measurements, and results are summarized as follows:

- Based on the undertaken study and analysis, it is observed that a high-voltage, high-efficiency IR-UWB transmitter tag is needed for various applications. These applications include long-range indoor positioning and tracking in a cluttered environment and IR-UWB radar systems.
- An energy-efficient high peak power IR-UWB transmitter tag MMIC design and its optimization is presented. The improvement technique (using a cascode pair) to get a significantly higher output voltage swing is demonstrated. An in-depth circuital analysis is performed and explained in detail. The impulse voltage generation process is explained in detail. The analysis of the distributed pulse former circuit is performed to get good impedance match and precise amplitude control of impulse voltage at each stage of the pulse former. The temperature-dependent parasitic effect is studied, and the corresponding mathematical model is derived. The individual transient delay of each stage of the IR-UWB pulse generator is calculated. The effect of transient delay on IR-UWB pulse formation and beamforming are explained.
- The 2 μm GaAs HBT process is used for the fabrication of the proposed MMIC. The measured peak-to-peak voltage of the generated IR-UWB pulse is 10.2 V (24.15 dBm) for a 50 Ω load impedance, which is the highest reported amplitude to the best of the author's knowledge. The generated UWB pulse is centered at 4.45 GHz with a -10dB bandwidth of 2 GHz. The total power consumption is 0.122 mW at a pulse repetition frequency of 100 kHz and the power efficiency of 9.18% (18.4%) is obtained.

- An innovative method of achieving better accuracy in the case of an autonomous robot deployed in the industrial environment is presented. A multi-beam IR-UWB transmitter array is proposed, implemented and related measurement results are provided. The beam steering-angle analysis is presented. The radiation intensity calculation is performed, and an intensity table is proposed, which helps to determine the intensity of the radiated pulse and quantify the broadening of pulse in terms of the number of carrier cycles present in the pulse.
- Eventually, two transmitter arrays with separation of 18 *cm* and 10.2 *cm* are optimized and demonstrated. The array with spacing of 10.2 *cm* is found better for the use case explained in the paper. The optimized arrays are tuned to different steering angles and time-domain radiation patterns are plotted. Comparisons between the simulated and measured radiation patterns are provided, which shows a great match. The true-time digital delay cell is exploited, and the steering range from -60º (-90º) to +60º (+90º) with a scanning resolution of 5º and 8º is achieved and demonstrated.
- An algorithm for the non-linear collaborative virtual array formation is proposed to get a single beam radiation-pattern for an array with electrically larger spacing between the nodes. The proposed algorithm for the separation between the transmitting nodes is simulated and prototyped. The results for the different case of a collaborative virtual array are analyzed and optimized for better performance. The proposed algorithm is implemented to verify the radiation pattern of the transmitter array.
- A prototype is developed using true-time delay cells, IR-UWB pulse generator and UWB antenna. Delay calibration of the true-time delay cell is performed for beam steering. Two different transmitter arrays are scaled-down and optimized for the measurement. Minor lobe suppression of 6 *dB* is achieved for the array $N = 4$, $d = [10, 6, 10]$ *cm* steered at 0º. For the worst-case scenario, the suppression of 4.25 *dB* is

achieved for the array $N = 4$, $d = [12.5, 7.5, 12.5]$ *cm* steered at 0º and 14º. The 4-element array achieves 13.5 *dBi* gain and 80% efficiency.

6.2 Recommendations for Future Work

In this thesis, the author has focused on IR-UWB circuit design and beamforming for indoor positioning and radar applications. The ultimate aim of the research was to increase the output peak power of IR-UWB pulse emitter nodes. The high-voltage pulse eventually increases the positioning range accuracy as well as improves the signal-to-noise ratio while operating as radar. Even though the author has achieved this target and demonstrated the significant improvement in output peak-power, future work could further utilize the outcome of the presented research and developed as a full system. The authors of the thesis would like to recommend some future work as explained below:

I. Energy-Efficient Impulse Radio Radar in mmWave bands

In Chapter-3, an oscillator-free distributed network for IR-UWB pulse formation is proposed and demonstrated for the 3-5 *GHz* UWB band. Since the pulse forming network does not use an oscillator, the power consumption is significantly reduced as compared to a system utilizing local-oscillators. More importantly, the proposed architecture has a controllable delay line, which can be used to generate a pulse position modulated signal. The presented circuital analysis in Chapter-3 could be used for designing an energy-efficient short-length multicycle signal generator in mmWave range for an ultra-high-resolution radar or communication. The amplification and distributed transmission line analysis, together with temperature depended transient behaviour of the circuit provided in Chapter-3 could be useful to optimize the pulse position modulated generator in mmWave bands. The folding techniques could be utilized to reduce the capacitive load of the joint node between the delay lines.

II. Development of an Algorithms for Indoor Positioning and Tracking System utilizing the Multi-Beam System

In Chapter-4, a multi-beam IR-UWB autonomous node for indoor positioning and tracking application is presented. The multi-beam radiation pattern can improve the positioning accuracy of moving nodes and determine the initial orientation of stationary nodes. This is theoretically discussed, and a flow chart diagram of a complete approach is presented. However, the implementation of the overall system for indoor positioning and tracking of an autonomous tag moving in the cluttered environment needs an algorithm. The future work may consider developing an algorithm, which will utilize the beam steering-angle analysis and GDOP technique discussed in the chapter-4 to efficiently identify beams and consequently calculate the high accuracy positions of the tag. An algorithm for range calculation of sensors node's position utilizing the Omni-directional radiation pattern is greatly discussed in the literature. However, range calculation using directional multi-beam is limited available in the literature. The algorithm for range calculation utilizing simultaneous multi-beam radiation pattern will significantly contribute to the state-of-art of the precise indoor positioning and tracking application.

III. Wireless clock synchronization of nodes in a collaborative array

In Chapter-5, the radiation pattern analysis for collaborative array has been proposed and demonstrated. However, a perfect clock synchronization of nodes was assumed during the study and a wired connection between the nodes was utilized to achieve the synchronization. In real-life application conditions, a wireless synchronization scheme is needed. The wireless synchronization of nodes is an independent problem in wireless sensor networks. Researchers

have proposed several methods to achieve wireless synchronization, which can be seen [152]. A reported literature claim 0.29 *ps* rms-jitter in synchronization-clock for wireless sensor nodes in [153], [154]. The author of this thesis would like to draw the attention to a reported paper, which has utilized the pulse injection locking technique to achieve the ~8 *ps* rms-jitter in clock synchronization for 3-5 *GHz* IR-UWB band [155]. The proposed work in [155] could be a starting point for designing and development of the wireless synchronized sensor nodes for a collaborative array, which can generate single narrow beam-width radiation pattern for various imaging applications.

Author's Publications

Journals

1. **M. Arif Hussain Ansari**, and Choi Look Law. "Circuit Analysis and optimization of High-Voltage High-Efficiency IR-UWB Pulse generator for Ranging and Radar Application" *IET Circuit Devices and System,* Vol. 14, No. 4, pp. 562 – 568, July 2020.

2. **M. Arif Hussain Ansari**, and Choi Look Law. "Grating Lobe Suppression of Multi-cycle IR-UWB Collaborative Radar Sensor in Wireless Sensor Network System" *IEEE Sensors Letters,* Vol. 4, No. 1, pp. 1-4, Jan. 2020.

3. **M. Arif Hussain Ansari**, and Choi Look Law. "Beam-Pattern Analysis of Multi-Beam High Peak Power IR-UWB Transmitter Tag for Indoor Positioning and Tracking System" *Progress In Electromagnetics Research B,* Vol. 86, 1-18, 2020.

International Conferences

4. **M. Arif Hussain Ansari**, and Choi Look Law. "Steerable Beamforming UWB-IR Transmitter Array for Directional Indoor Positioning Applications". *Progress In Electromagnetic Research Symposium (PIERs), Toyama, Japan,* 1-4 August 2018.

5. **M. Arif Hussain Ansari**, Choi Look Law, "Beamforming UWB-IR transmitter for NLOS indoor positioning and tracking application", *IEEE MTT-S International Wireless Symposium, Chengdu, China*. 6-10 May 2018. **(*Best Paper Award*)**

6. **M. Arif Hussain Ansari**, Manmohan Sharma, and Choi Look Law. "High Peak Power UWB-RFID Transmitter Tag for Long Range Applications". *Progress In Electromagnetic Research Symposium (PIERs) Singapore,* 19-22 Nov 2017. **(*Best Paper Award*)**

7. **M. Arif Hussain Ansari**, Manmohan Sharma, and Choi Look Law. "High Peak Power IR-UWB Pulse Generator for Long Range Indoor Localization". *Progress In Electromagnetic Research Symposium (PIERs) Singapore,* 19-22 Nov 2017.

8. **M. Arif Hussain Ansari**, and Choi Look Law. “High voltage high-efficiency UWB pulse generator for precision localization wireless sensor network.” *IEEE International Symposium on Integrated Circuits (ISIC) Singapore*, 12-14 Dec 2016.

Bibliography

[1] J. Z. J. Zhang, P. V. Orlik, Z. Sahinoglu, A. F. Molisch, and P. Kinney, "UWB Systems for Wireless Sensor Networks," *Proc. IEEE*, vol. 97, no. 2, pp. 313–331, 2009.

[2] K. Siwiak and D. McKeown, *Ultra-Wideband Radio Technology*. John Wiley & Sons, Ltd, 2004.

[3] T. Prakash and D. Ghosh, "Review of the ultra wideband pulse generation," in *2015 International Conference on Microwave, Optical and Communication Engineering, ICMOCE 2015*, 2016, pp. 310–313.

[4] Y. Shen, "Passive Components Design for UWB-RFID Systems," Ph.D. Thesis @ School of Electrical and Electonic Engineering, Nanyang Technological University Singapore, 2012.

[5] S. Bourdel *et al.*, "A 9-pJ/Pulse 1.42-Vpp OOK CMOS UWB Pulse Generator for the 3.1–10.6-GHz FCC Band," *IEEE Trans. Microw. Theory Tech.*, vol. 58, no. 1, pp. 65–73, 2010.

[6] Z. Xu, M. Luo, Z. Chen, H. Nie, and L. Yu, "Performance Analysis of Pulse Generators for UWB-Based Sensor Networks," in *International Conference on Communications and Mobile Computing*, 2009, pp. 466–470.

[7] A. Eryildirim and M. B. Guldogan, "A Bernoulli Filter for Extended Target Tracking Using Random Matrices in a UWB Sensor Network," *IEEE Sens. J.*, vol. 16, no. 11, pp. 4362–4373, 2016.

[8] T. Norimatsu *et al.*, "A UWB-IR Transmitter With Digitally Controlled Pulse Generator," *IEEE J. Solid-State Circuits*, vol. 42, no. 6, pp. 1300–1309, 2007.

[9] J. Xia, C. L. Law, Y. Zhou, and K. S. Koh, "3-5 GHz UWB Impulse Radio Transmitter and Receiver MMIC Optimized for Long Range Precision Wireless Sensor Networks," *IEEE Trans. Microw. Theory Tech.*, vol. 58, no. 12, pp. 4040–4051, 2010.

[10] F. C. Commission, "Revision of Part 15 of the Commission's Rules Regarding Ultra-Wideband Transmission Systems," Washington, D.C. 20554, 2002.

[11] Z. Farid, R. Nordin, and M. Ismail, "Recent advances in wireless indoor localization techniques and system," *J. Comput. Networks Commun.*, vol. 2013, no. 185138, pp. 1–

12, 2013.

[12] J. J. Xia, C. L. Law, K. S. Koh, Y. Zhou, and C. Fang, “A 3-5 GHz impulse radio UWB transceiver IC optimized for precision localization at longer ranges,” in *IEEE MTT-S International Microwave Symposium Digest*, 2010, pp. 169–172.

[13] A. A. Khan, A. I. E. Yakzan, and M. Ali, “Radio Frequency Identification (RFID) Based Toll Collection System,” in *Third International Conference on Computational Intelligence, Communication Systems and Networks Radio*, 2011, pp. 103–107.

[14] I. Mahbub, S. K. Islam, and A. Fathy, “Impulse Radio Ultra-Wideband (IR-UWB) Transmitter for Low Power Low Data Rate Biomedical Sensor Applications,” in *IEEE Topical Conference on Biomedical Wireless Technologies, Networks, and Sensing Systems*, 2016, pp. 88–90.

[15] C. Lai, K. Tan, Y. Chen, and T.-S. Chu, “A UWB Impulse-Radio Timed-Array Radar With Time-Shifted Direct-Sampling Architecture in 0.18-μm CMOS,” *IEEE Trans. Circuits Syst. I Regul. Pap.*, vol. 61, no. 7, pp. 2074–2087, 2014.

[16] B. Schleicher *et al.*, “IR-UWB Radar Demonstrator for Ultra-Fine Movement Detection and Vital-Sign Monitoring,” *IEEE Trans. Microw. Theory Tech.*, vol. 61, no. 5, pp. 2076–2085, 2013.

[17] H. Nikookar and R. Prasad, *Introduction to Ultra-Wideband for Wireless Communications*. Springer Science Business Media B.V., 2009.

[18] R. Hossain, M. Ahmed, M. Alfasani, and H. U. Zaman, “An Advanced Security System Integrated With RFID Based Automated Toll Collection System,” in *Third Asian Conference on Defence Technology*, 2017, pp. 1–6.

[19] “Ultra-Wideband (UWB) Market by End-User, Application and Geography - Global Forecast to 2022,” *Reaseach and Market*, 2017. [Online]. Available: https://www.researchandmarkets.com/research/z47j6r/ultrawideband.

[20] “Ultra-Wideband (UWB) - Market Analysis, Trends, and Forecasts,” *Research and Market*, 2019. [Online]. Available: https://www.researchandmarkets.com/reports/4845840/ultra-wideband-uwb-market-analysis-trends#pos-0.

[21] “Ultra-Wideband (UWB) Market by End-User (Healthcare, Automotive and

Transportation, Manufacturing, Residential Retail), Application (RTLS/WSN, Imaging), and Geography (North America, Europe, Asia-Pacific, Rest of the World) - Global Forecast to 2022," *Research and Market*, 2017. [Online]. Available: https://www.researchandmarkets.com/research/z47j6r/ultrawideband.

[22] "Global Real Time Location System Market Forecasts and Trends (2016 - 2021)," *Research and Market*, 2016. [Online]. Available: https://www.researchandmarkets.com/research/7wwxs7/global_real_time.

[23] "Global Real Time Location System Market - By Technology , Industry, Geography, Trends, Forecast - 2017 - 2022," *Research and Market*, 2018. [Online]. Available: https://www.researchandmarkets.com/reports/4699509/global-real-time-location-systems-rtls-market#rela0-4389027.

[24] G. Leucci, "Ground Penetrating Radar: The Electromagnetic Signal Attenuation and Maximum Penetration Depth," *Sch. Res. Exch.*, vol. 2008, no. 926091, pp. 1–7, 2008.

[25] A. Eltaher and T. Kaiser, "A Novel Approach based on UWB Beamforming for Indoor Positioning in None-Line-of-Sight Environments," in *RadioTeCc*, 2005, pp. 1–5.

[26] B. Silva and G. P. Hancke, "IR-UWB-Based Non-Line-of-Sight Identification in Harsh Environments: Principles and Challenges," *IEEE Trans. Ind. Informatics*, vol. 12, no. 3, pp. 1188–1195, 2016.

[27] M. A. H. Ansari and C. L. Law, "High voltage high efficiency UWB pulse generator for precision localization wireless sensor network," in *International Symposium on Integrated Circuits (ISIC), Singapore*, 2016, pp. 1–4.

[28] V. Moreno *et al.*, "Integrated 16-ps Pulse Generator Based on a Reflective SOA-EAM for UWB Schemes," *IEEE Photonics Technol. Lett.*, vol. 28, no. 20, pp. 2180–2182, 2016.

[29] D. Anzai *et al.*, "Experimental evaluation of implant UWB-IR transmission with living animal for body area networks," *IEEE Trans. Microw. Theory Tech.*, vol. 62, no. 1, pp. 183–192, 2014.

[30] C. L. Law *et al.*, "An Ultra-Wideband Localization System for Concrete Debris Tracking," in *Asia Pacific Microwave Conference*, 2009, pp. 265–268.

[31] Y. Gu, A. Lo, and I. Niemegeers, "A Survey of Indoor Positioning Systems for Wireless

Personal Networks," *IEEE Commun. Surv. Tutorials*, vol. 11, no. 1, pp. 13–32, 2009.

[32] J. Xia, "Impulse Radio UWB Circuits for Real Time Location Systems," Ph.D. Thesis @ School of Electrical and Electronic Engineering, Nanyang Technological University, 2013.

[33] "Indoor Path Loss," *Apllication note :- Digi International*, 2012. [Online]. Available: http://ftp1.digi.com/support/images/XST-AN005a-IndoorPathLoss.pdf.

[34] E. M. Staderini, "UWB Radar in Medicine," *IEEE AESS Systems Magazine*, pp. 13–18, 2002.

[35] C. Gabriel, "Compilation of the Dielectric Properties of Body Tissues at RF and Microwave Frequencies," *Phys. Dep. King's Coll. London, London WC2R 2LS, UK; Armstrong Lab. (AFMC), Occup. Environ. Heal. Dir. Radiofreq. Radiat. Div. Rep. AOE-TR- 1996-0037*, 1996.

[36] G. Ross, "Transmission and reception system for generating and receiving base-band pulse duration pulse signals without distortion for short base-band communication system," *U.S. Pat. No. 3,728,632*, 1973.

[37] T. Barrett, "History of UltraWideBand (UWB) Radar & Communications: Pioneers and Innovators," in *Progress In Electromagnetics Symposium 2000*, 2000, pp. 1–30.

[38] C. L. Bennett and G. F. Ross, "Time-Domain Electromagnetics and Its Applications," *Proc. IEEE*, vol. 66, no. 3, pp. 299–318, 1978.

[39] P. Pagani, F. T. Talom, P. Pajusco, and B. Uguen, *Ultra-Wideband Radio Propagation Channels*. John Wiley & Sons, Inc, 2008.

[40] J. D. Taylor, *Introduction to ultra-wideband radar systems*. CRC Press, Boca Raton, 1995.

[41] B. Allen, M. Dohler, E. E. Okon, W. Q. Malik, A. K. Brown, and D. J. Edwards, *Ultra Wideband Antennas and Propagation for Communications, Radar and Imaging*. John Wiley & Sons, Inc., 2006.

[42] T. Zwick, W. Wiesbeck, J. Timmermann, and G. Adamiuk, *Ultra-wideband RF system engineering*. Cambridge University Press, 2011.

[43] Y. Zhou, C. L. Law, and J. Xia, "Ultra Low-Power UWB-RFID System for Precise

Location-Aware Applications," in *IEEE Wireless Communications and Networking Conference Workshops (WCNCW)*, 2012, pp. 154–158.

[44] M. Ghavami, L. B. Michael, and R. Kohno, *Ultra Wideband Signals and Systems in Communication Engineering*. John Wiley & Sons Ltd, 2004.

[45] A. Alarifi *et al.*, "Ultra Wideband Indoor Positioning Technologies: Analysis and Recent Advances," *Sensors*, vol. 16, no. 5, pp. 1–36, 2016.

[46] R. J. Fontana and E. A. Richley, "Observations on Low Data Rate, Short Pulse UWB Systems," in *IEEE International Conference on Ultra-Wideband*, 2007, pp. 334–338.

[47] H. Arslan, Z. N. Chen, and M.-G. Di Benedetto, *Ultra Wideband Wireless Communication*. Hoboken, New Jersey: John Wiley & Sons, Inc., 2006.

[48] L. Lampe and K. Witrisal, "Challenges and Recent Advances in IR-UWB System Design," in *IEEE International Symposium on Circuits and Systems (ISCAS)*, 2010, pp. 3288–3291.

[49] Q. Dhal, "High-precision beamforming with UWB impulse radar," Master Thesis @ Department of informatic, University of Oslo, 2009.

[50] M. Y. W. Chia, T. H. Lim, J. K. Yin, P. Y. Chee, S. W. Leong, and C. K. Sim, "Electronic Beam-Steering Design for UWB Phased Array," *IEEE Trans. Microw. Theory Tech.*, vol. 54, no. 6, pp. 2431–2438, 2006.

[51] S. M. A. Motakabber, M. I. Ibrahmy, and A. H. M. Zahirul Alam, "Development of a Position Detection Technique for UWB Chipless RFID Tagged Object," in *ICCEEE*, 2013, pp. 735–738.

[52] A. Yassin *et al.*, "Recent Advances in Indoor Localization: A Survey on Theoretical Approaches and Applications," *IEEE Commun. Surv. Tutorials*, vol. 19, no. 2, pp. 1327–13476, 2017.

[53] H. Nikookar and R. Prasad, *Introduction to Ultra Wideband for Wireless Communications*. Springer Science Business Media B.V., 2009.

[54] Y. Zhu, J. D. Zuegel, J. R. Marciante, and H. Wu, "Distributed Waveform Generator : A New Circuit Technique for Ultra-Wideband Pulse Generation , Shaping and Modulation," *IEEE J. Solid-State Circuits*, vol. 44, no. 3, pp. 808–823, 2009.

[55] J. Lee, Y. J. Park, M. Kim, C. Yoon, J. Kim, and K. H. Kim, "System-on-package ultra-wideband transmitter using CMOS impulse generator," in *IEEE Transactions on Microwave Theory and Techniques*, 2006, vol. 54, no. 4, pp. 1667–1673.

[56] J. Han and C. Nguyen, "On the development of a compact sub-nanosecond tunable monocycle pulse transmitter for UWB applications," *IEEE Trans. Microw. Theory Tech.*, vol. 54, no. 1, pp. 285–293, 2006.

[57] R. Jin, S. Halder, J. C. M. Hwang, and C. L. Law, "Tunable pulse generator for ultra-wideband applications," in *Asia Pacific Microwave Conference*, 2009, pp. 2272–2275.

[58] K. Li, D. Kurita, and T. Matsui, "A novel UWB bandpass filter and its application to UWB pulse generation," in *ICU 2005: 2005 IEEE International Conference on Ultra-Wideband, Conference Proceedings*, 2005.

[59] Y. Zhu and H. Wu, "Integrated distributed transversal filters for pulse shaping and interference suppression in UWB impulse radios," in *ICUWB2006: 2006 IEEE International Conference on Ultra-Wideband - Proceedings*, 2007.

[60] Y. Wu, A. F. Molisch, S. Y. Kung, and J. Zhang, "Impulse radio pulse shaping for Ultra-Wide Bandwidth (UWB) systems," in *IEEE International Symposium on Personal, Indoor and Mobile Radio Communications, PIMRC*, 2003.

[61] Y. Zhu, J. D. Zuegel, J. R. Marciante, and H. Wu, "A 0.18μm CMOS distributed transversal filter for sub-nanosecond pulse synthesis," in *Proceedings - 2006 IEEE Radio and Wireless Symposium*, 2006.

[62] D. D. Wentzloff and A. P. Chandrakasan, "Gaussian Pulse Generators for Subband Ultra- Wideband Transmitters," *IEEE Trans. Microw. Theory Tech.*, vol. 54, no. 4, pp. 1647 – 1655, 2006.

[63] Y. Zheng *et al.*, "A 0.18μm CMOS dual-band UWB transceiver," in *Digest of Technical Papers - IEEE International Solid-State Circuits Conference*, 2007.

[64] S. Iida *et al.*, "A 3.1 to 5 GHz CMOS DSSS UWB transceiver for WPANs," in *IEEE International Solid-State Circuits Conference, ISSCC.*, 2005, pp. 214–594.

[65] A. T. Phan, J. Lee, V. Krizhanovskii, Q. Le, S. K. Han, and S. G. Lee, "Energy-efficient low-complexity CMOS pulse generator for multiband UWB impulse radio," *IEEE Trans. Circuits Syst. I Regul. Pap.*, vol. 55, no. 11, pp. 3552–3563, 2008.

[66] S. Diao and Y. Zheng, “An ultra low power and high efficiency UWB transmitter for WPAN applications,” *ESSCIRC 2008 - Proc. 34th Eur. Solid-State Circuits Conf.*, pp. 334–337, 2008.

[67] S. Sim, D. W. Kim, and S. Hong, “A CMOS UWB pulse generator for 610 GHz applications,” *IEEE Microw. Wirel. Components Lett.*, vol. 19, no. 2, pp. 83–85, 2009.

[68] A. M. El-Gabaly and C. E. Saavedra, “A 3 – 10-GHz 13-pJ / Pulse Dual BPSK / QPSK Pulse Modulator Based on Harmonic Injection Locking,” *IEEE Trans. Microw. Theory Tech.*, vol. 62, no. 12, pp. 3476–3484, 2014.

[69] T. A. Phan, J. Lee, V. Krizhanovskii, S. K. Han, and S. G. Lee, “A 18-pJ/pulse OOK CMOS transmitter for multiband UWB impulse radio,” *IEEE Microw. Wirel. Components Lett.*, 2007.

[70] H. Kim, D. Park, and Y. Joo, “All-digital low-power CMOS pulse generator for UWB system,” *Electron. Lett.*, vol. 40, no. 24, pp. 1534–1535, 2004.

[71] L. Zhou, Z. Chen, C.-C. Wang, F. Tzeng, V. Jain, and P. Heydari, “A 2-Gb/s 130-nm CMOS RF-Correlation-Based IR-UWB Transceiver Front-End,” *IEEE Trans. Microw. Theory Tech.*, vol. 59, no. 4, pp. 1117–1130, 2011.

[72] H. Cho, H. Lee, J. Bae, and H. J. Yoo, “A 5.2 mW IEEE 802.15.6 HBC Standard Compatible Transceiver with Power Efficient Delay-Locked-Loop Based BPSK Demodulator,” *IEEE J. Solid-State Circuits*, vol. 50, no. 11, pp. 2549–2559, 2015.

[73] B. T. Reyes, R. M. Sanchez, A. L. Pola, and M. R. Hueda, “Design and Experimental Evaluation of a Time- Interleaved ADC Calibration Algorithm for Application in High-Speed Communication Systems,” *IEEE Trans. Circuits Syst. I Regul. Pap.*, vol. 64, no. 5, pp. 1019–1030, 2016.

[74] J. Li, S. Jung, M. Lu, P. Gui, and Y. Joo, “A Current-Steering DAC-Based CMOS Ultra-Wideband Impulse Generator,” in *IEEE International Symposium on Communications and Information Technology*, 2009, pp. 971–975.

[75] A. Popa, N. D. Alexandru, and R. G. Bozomitu, “A 2-PPM CMOS Modulator for IR-UWB Signals,” in *IEEE International Conference on Communications (COMM)*, 2016, pp. 353–356.

[76] B. J. Silva and G. P. Hancke, “Practical Challenges of IR-UWB based Ranging in Harsh

Industrial Environments," in *IEEE International Conference on Industrial Informatics*, 2015, pp. 618–623.

[77] M. A. H. Ansari, M. Sharma, and C. L. Law, "High Peak Power UWB-RFID Transmitter Tag for Long Range Applications," in *Progress in Electromagnetics Research Symposium*, 2017, pp. 2045–2050.

[78] V. V. Kulkarni, M. Muqsith, K. Niitsu, H. Ishikuro, and T. Kuroda, "A 750 Mb/s, 12 pJ/b, 6-to-10 GHz CMOS IR-UWB transmitter with embedded on-chip antenna," *IEEE J. Solid-State Circuits*, vol. 44, no. 2, pp. 394–403, 2009.

[79] J. Li, S. Jung, M. Lu, P. Gui, and Y. Joo, "A Current-Steering DAC-Based CMOS Ultra-Wideband Impulse Generator," in *IEEE International Symposium on Communications and Information Technology, ISCIT*, 2009, pp. 971–975.

[80] Y. Zhu, J. D. Zuegel, J. R. Marciante, and H. Wu, "A 10.9 GS/s, 64 taps distributed waveform generator with DAC-assisted current-steering pulse generators in 0.18μm Digital CMOS," in *2008 IEEE Topical Meeting on Silicon Monolithic Integrated Circuits in RF Systms - Digest of Papers, SiRF*, 2008, pp. 13–16.

[81] D. Baranauskas and D. Zelenin, "A 0.36W 6b up to 20GS/s DAC for UWB wave formation," in *Digest of Technical Papers - IEEE International Solid-State Circuits Conference*, 2006.

[82] Y. Ayasli, L. D. Reynolds, R. L. Mozzi, and L. K. Hanes, "2-20-GHz GaAs Traveling-Wave Power Amplifier," *IEEE Transactions on Microwave Theory and Techniques*. 1984.

[83] J. B. Beyer, S. N. Prasad, R. C. Becker, J. E. Nordman, and G. K. Hohenwarter, "MESFET Distributed Amplifier Design Guidelines," *IEEE Transactions on Microwave Theory and Techniques*. 1984.

[84] B. Y. Banyamin and M. Berwick, "Analysis of the performance of four-cascaded single-stage distributed amplifiers," *IEEE Trans. Microw. Theory Tech.*, 2000.

[85] K. L. Deng, T. W. Huang, and H. Wang, "Design and analysis of novel high-gain and broad-band GaAs pHEMT MMIC distributed amplifiers with traveling-wave gain stages," *IEEE Trans. Microw. Theory Tech.*, 2003.

[86] C. Fang, C. L. Law, and J. Hwang, "High-voltage high-efficiency ultrawideband pulse

synthesizer," *IEEE Microw. Wirel. Components Lett.*, vol. 20, no. 1, pp. 49–51, 2010.

[87] C. Fang and C. L. Law, "Design and Analysis of High-Voltage High- Efficiency Ultra-Wideband Pulse Synthesizer," *Prog. Electromagn. Res. C*, vol. 20, pp. 187–201, 2011.

[88] Z. Wang, X. Chen, Y. Shen, W. Rhee, and Z. Wang, "A 3.1-4.8-GHz Delay-Line-Based Frequency-Hopping IR-UWB Transmitter in 65-nm CMOS Technology," in *12th IEEE International Conference on Solid-State and Integrated Circuit Technology*, 2014, pp. 1–3.

[89] J. Kang, S. Rao, P. Chiang, and A. Natarajan, "Design and Optimization of Area-Constrained Wirelessly Powered CMOS UWB SoC for Localization Applications," *IEEE Trans. Microw. Theory Tech.*, vol. 64, no. 4, pp. 1042–1054, 2016.

[90] C. Lai *et al.*, "A UWB IR Timed-Array Radar Using Time-Shifted Direct-Sampling Architecture," in *Symposium on VLSI Circuits Digest of Technical Papers*, 2012, pp. 54–55.

[91] C. Patel and B. Mishra, "All Digital Delay-line based Ultra Wide Band Transmitter Architecture in 0.18 μm CMOS Chirag Patel and Biswajit Mishra," in *9th International Conference on Industrial and Information Systems (ICIIS)*, 2015, pp. 1–6.

[92] L. Smaïni *et al.*, "Single-Chip CMOS Pulse Generator for UWB Systems," *IEEE J. Solid-State Circuits*, vol. 41, no. 7, 2006.

[93] M. Shen, Y. Z. Yin, H. Jiang, T. Tian, and J. H. Mikkelsen, "A 3-10 GHz IR-UWB CMOS pulse generator with 6 mW peak power dissipation using a slow-charge fast-discharge technique," *IEEE Microw. Wirel. Components Lett.*, vol. 24, no. 9, pp. 634–636, 2014.

[94] Y. Kawano *et al.*, "RF chipset for impulse UWB radar using 0.13-μm InP-HEMT technology," *IEEE Trans. Microw. Theory Tech.*, vol. 54, no. 12, pp. 4489–4496, 2006.

[95] Y. Kawano *et al.*, "An Rf Chipset for Impulse Radio UWB using 0.13 InP - HEMT Technology," in *IEEE MTT-S International Microwave Symposium Digest*, 2006, pp. 316–319.

[96] K. Wang, B. Li, M. J. Zhao, and Z. H. Wu, "Low-power implantable CMOS bipolar Gaussian monocycle pulse generator," *Electron. Lett.*, vol. 53, no. 3, pp. 201–203, 2017.

[97] S. Diao, Y. Zheng, and C. H. Heng, "A CMOS ultra low-power and highly efficient

UWB-IR transmitter for WPAN applications," *IEEE Trans. Circuits Syst. II Express Briefs*, vol. 56, no. 3, pp. 200–204, 2009.

[98] D. Martynenko, G. Fischer, and O. Klymenko, "A High Band Impulse Radio UWB Transmitter for Communication and Localization," in *ICUWB 2009*, 2009, vol. 2009, pp. 359–363.

[99] D. Martynenko, G. Fischer, and O. Klymenko, "An Impulse Radio UWB Transmitter for Communication and Precise Localization," in *IEEE 13th Topical Meeting on Silicon Monolithic Integrated Circuits in RF Systems*, 2013, pp. 69–71.

[100] D. Martynenko, G. Fischer, and O. Klymenko, "UWB Transmitter for Communication and Localization for IEEE 802.15.4a Standard," in *IEEE International Conference on Circuits and Systems*, 2012, pp. 32–37.

[101] O. Klymenko, D. Martynenko, and G. Fischer, "A highly integrated IR-UWB Transceiver for Communication and Localization," in *ISOCC 2012*, 2012, pp. 57–60.

[102] D. Lin, B. Schleicher, A. Trasser, and H. Schumacher, "Si/SiGe HBT UWB impulse generator tunable to FCC, ECC and Japanese spectral masks," in *IEEE Radio and Wireless Symposium, RWS*, 2011, pp. 66–69.

[103] A. Rahimian and A. Rahimian, "Enhanced RF steerable beamforming networks based on Butler Matrix and Rotman Lens for ITS applications," *Proc. - 2010 IEEE Reg. 8 Int. Conf. Comput. Technol. Electr. Electron. Eng. Sib.*, pp. 567–572, 2010.

[104] Y. L. LeiWang and C. H. Heng, "3 – 5 GHz 4-Channel UWB Beamforming Transmitter With 1° Scanning Resolution Through Calibrated Vernier Delay Line in 0.13-μm CMOS," *IEEE J. Solid-State Circuits*, vol. 47, no. 12, pp. 3145–3159, 2012.

[105] L. Wang, Y. X. Guo, Y. Lian, and C. H. Heng, "3-to-5 GHz 4-Channel UWB Beamforming Transmitter with 1° Phase Resolution Through Calibrated Vernier Delay Line in 0.13 μm CMOS," in *IEEE International Solid-State Circuits Conference*, 2012, pp. 2011–2013.

[106] Z. Safarian, T. S. Chu, and H. Hashemi, "A 0.13μm CMOS 4-Channel UWB Timed Array Transmitter Chipset with sub-200ps Switches and All-Digital Timing Circuitry," in *IEEE Radio Frequency Integrated Circuits Symposium*, 2008, pp. 601–604.

[107] A. Natarajan, A. Komijani, and A. Hajimiri, "A fully integrated 24-GHz phased-array

transmitter in CMOS," *IEEE J. Solid-State Circuits*, vol. 40, no. 12, pp. 2502–2513, 2005.

[108] J. Roderick, H. Krishnaswamy, K. Newton, and H. Hashemi, "Silicon-Based Ultra-Wideband Beam-Forming," *IEEE J. Solid-State Circuits*, vol. 41, no. 8, pp. 1726–1739, 2006.

[109] D. Dupleich *et al.*, "Directional Characterization of the 60 GHz Indoor-Office Channel," in *31th URSI General Assembly and Scientific Symposium, URSI GASS*, 2014, pp. 14–17.

[110] J. M. Janky, K. A. I. Sharp, M. V. McCusker, and M. Ulman, "Indoor Navigation via Multi-Beam Laser Projection," United States Patent(US 20140285631A1), 2014.

[111] S. Jayaprakasam, S. K. A. Rahim, and C. Y. Leow, "Distributed and Collaborative Beamforming in Wireless Sensor Networks: Classifications, Trends, and Research Directions," *IEEE Commun. Surv. Tutorials*, vol. 19, no. 4, pp. 2092–2116, 2017.

[112] M. F. A. Ahmed, "Collaborative Beamforming for Wireless Sensor Networks," vol. 8, no. 2, pp. 638–643, 2011.

[113] Q. Liang, "Collaborative Signal Processing Using Radar Sensor Networks," in *IEEE Military Communications conference*, 2006, pp. 1–6.

[114] G. Sun, Y. Liu, J. Zhang, A. Wang, and X. Zhou, "Node selection optimization for collaborative beamforming in wireless sensor networks," *Ad Hoc Networks*, vol. 37, pp. 389–403, 2016.

[115] Y. Noh, H. Yamaguchi, U. Lee, P. Vij, J. Joy, and M. Gerla, "CLIPS: Infrastructure-free collaborative indoor positioning scheme for time-critical team operations," *IEEE Trans. Syst. Man, Cybern. Syst.*, vol. 48, no. 3, pp. 172–178, 2018.

[116] M. A. H. Ansari and C. L. Law, "Beamforming UWB-IR Transmitter for NLOS Indoor Positioning and Tracking Application," in *IEEE MTT-S International Wireless Symposium (IWS)*, 2018, pp. 1–4.

[117] S. Ries and T. Kaiser, "Ultra wideband impulse beamforming: It is a different world," *Signal Processing*, vol. 86, no. 9, pp. 2198–2207, 2006.

[118] M. G. M. Hussain, "Performance Analysis of Space-Time Array Processing Using Ultrawideband-Throb Signals for High-Resolution Imaging," *IEEE Trans. Geosci.*

Remote Sens., vol. 56, no. 9, pp. 5064–5082, 2018.

[119] N. J. Reilly, G. Wang, and T. Xia, "CMOS programmable time control circuit design for phased array UWB ground penetrating radar antenna beamforming," in *IEEE international Midwest Symposium on Circuits and Systems*, 2017, pp. 922–925.

[120] L. Wang, K. H. Teng, Y. Lian, and C. H. Heng, "A 4 × 4 IR UWB Timed-Array Radar Based on 16-Channel Transmitter and Sampling Capacitor Reused Receiver," *IEEE Trans. Circuits Syst. II Express Briefs*, vol. 65, no. 7, pp. 878–882, 2018.

[121] L. Qiang, W. Heng, L. Huican, Q. Shuqi, D. Nanxun, and L. Bing, "Formation control of multi robot based on UWB distance measurement," in *Proc. 30th Chinese Control and Decision Conference*, 2018, pp. 2404–2408.

[122] X. Liang, H. Zhang, G. Fang, S. Ye, and T. A. Gulliver, "An Improved Algorithm for Through-Wall Target Detection Using Ultra-Wideband Impulse Radar," *IEEE Access*, vol. 5, no. 1, pp. 22101–22118, 2017.

[123] M. Y. W. Chia, S. W. Leong, C. K. Sim, and K. M. Chan, "Through-wall UWB radar operating within FCC's mask for sensing heart beat and breathing rate," in *2nd European Radar Conference (EURAD)*, 2005, pp. 283–286.

[124] S. Haykin and M. Moher, *Communication Systems*. 2010.

[125] D. D. Wentzloff, "Pulse-Based Ultra-Wideband Transmitters for by Digital Communication," Massachusetts Institute of Technology, 2007.

[126] J. Xia and C. L. Law, "Cascoded HBT pair: A New Method of Generating Subnanosecond High-Voltage Impulses," *IEEE Microw. Opt. Technol. Lett.*, vol. 52, no. 8, pp. 1683–1685, 2010.

[127] J. Xia, C. L. Law, and T. T. Thein, "Generation of sub-nanosecond 7V Gaussian pulse using GaAs HBT with 3V battery supply," *APMC 2009 - Asia Pacific Microw. Conf. 2009*, pp. 1605–1608, 2009.

[128] M. Gerding, T. Musch, and B. Schiek, "Generation of short electrical pulses based on bipolar transistors," *Adv. Radio Sci.*, vol. 2, pp. 7–12, 2004.

[129] F. Terman, *Radio Engineers' Handbook*. McGraw-Hill Book Company, Inc., 1943.

[130] H. Miranda and T. H. Meng, "A programmable pulse UWB transmitter with 34% energy

efficiency for multichannel neuro-recording systems," in *IEEE Custom Integrated Circuits Conference*, 2010, pp. 1–4.

[131] J. Sewter and A. C. Carusone, "A 40 Gb / s Transversal Filter in 0 . 18 μ m CMOS Using Distributed Amplifiers," *IEEE J. Solid-State Circuits*, vol. 46, no. 7, pp. 1636–1647, 2011.

[132] T. I. Krebesz, G. Kolumban, C. K. Tse, F. C. M. Lau, and H. Dong, "Use of UWB Impulse Radio Technology in In-Car Communications: Power Limits and Optimization," *IEEE Trans. Veh. Technol.*, vol. 66, no. 7, pp. 6037–6049, 2017.

[133] A. Lazaro, D. Girbau, and R. Villarino, "Analysis of Vital Sings Monitoring using an IR-UWB Radar," *Prog. Electromagn. Res. PIER*, vol. 100, pp. 265–284, 2010.

[134] D. Neirynck, M. O. Duinn, and C. Mcelroy, "Characterisation of the NLOS Performance of an IEEE 802.15.4a Receiver," in *12th Workshop on Navigation, Positioning and Communications*, 2015, pp. 1–4.

[135] G. Fedele, E. Pittella, S. Pisa, M. Cavagnaro, R. Canali, and M. Biagi, "Sleep-Apnea Detection with UWB Active Sensors," in *IEEE International Conference on Ubiquitous Wireless Broadband (ICUWB)*, 2015, pp. 1–5.

[136] J. Pan, "Medical Applications of Ultra-WideBand (UWB)," *Surv. Pap.*, pp. 1–12, 2007.

[137] M. A. Hein, "Ultra-Wideband Radar Sensors for Biomedical Diagnostics and Imaging," in *IEEE International Conference on Ultra-Wideband*, 2012, pp. 486–490.

[138] A. P. Chandrakasan *et al.*, "Low-Power Impulse UWB Architectures and Circuits," *Proc. IEEE*, vol. 97, no. 2, pp. 332–352, 2009.

[139] I. Sharp, K. Yu, and Y. J. Guo, "GDOP analysis for positioning system design," *IEEE Trans. Veh. Technol.*, vol. 58, no. 7, pp. 3371–3382, 2009.

[140] G. Feng, C. Shen, C. Long, and F. Dong, "GDOP Index in UWB Indoor Location System Experiment," in *IEEE SENSORS*, 2015, pp. 1–4.

[141] R. Niu and P. K. Varshney, "Joint detection and localization in sensor networks based on local decisions," *Conf. Rec. - Asilomar Conf. Signals, Syst. Comput.*, no. 2, pp. 525–529, 2006.

[142] D. Ciuonzo and P. Salvo Rossi, "Distributed detection of a non-cooperative target via

generalized locally-optimum approaches," *Inf. Fusion*, vol. 36, pp. 261–274, 2017.

[143] D. Ciuonzo and P. Salvo Rossi, "Quantizer Design for Generalized Locally Optimum Detectors in Wireless Sensor Networks," *IEEE Wirel. Commun. Lett.*, vol. 7, no. 2, pp. 162–165, 2018.

[144] Y. Gu, A. Lo, S. Member, and I. Niemegeers, "Wireless Personal Networks," *Communications*, vol. 11, no. 1, pp. 13–32, 2009.

[145] D. Ciuonzo, "On time-reversal imaging by statistical testing," *IEEE Signal Process. Lett.*, vol. 24, no. 7, pp. 1024–1028, 2017.

[146] O. Oshiga, X. Chu, Y. Leung, and J. Ng, "Anchor Selection for Localization in Large Indoor Venues," 2018, pp. 1–6.

[147] R. B. Langley, "Dilution of Precision," *GPS World*, vol. 5, no. 10, pp. 52–68, 1999.

[148] C. Liao, P. Hsu, and D. Chang, "Energy Patterns of UWB Antenna Arrays With scan capability," *IEEE Trans. Antennas Propag.*, vol. 59, no. 4, pp. 1140–1147, 2011.

[149] M. G. M. Hussain, "Principles of space-time array processing for ultrawide-band impulse radar and radio communications," *IEEE Trans. Veh. Technol.*, vol. 51, no. 3, pp. 393–403, 2002.

[150] Y. Shen, C. L. Law, and Z. Shen, "A CPW-fed Circularly Polarixed Antenna for Lower Ultra-Wideband Applications," *Microw. Opt. Technol. Lett.*, vol. 51, no. 10, pp. 2365–2369, 2009.

[151] J. S. McLean, H. Foltz, and R. Sutton, "Pattern descriptors for UWB antennas," *IEEE Trans. Antennas Propag.*, vol. 53, no. 1, pp. 553–559, 2005.

[152] H. Aggrawal, P. Chen, M. M. Assefzadeh, B. Jamali, and A. Babakhani, "Gone in a Picosecond: Techniques for the Generation and Detection of Picosecond Pulses and Their Applications," *IEEE Microw. Mag.*, 2016.

[153] B. Jamali and A. Babakhani, "A fully integrated injection-locked picosecond pulse receiver for 0.29pSrms-jitter wireless clock synchronization in 65nm CMOS," in *IEEE MTT-S International Microwave Symposium Digest*, 2017.

[154] B. Jamali and A. Babakhani, "Wireless Time Transfer With Subpicosecond Accuracy Based on a Fully Integrated Injection-Locked Picosecond Pulse Detector," *IEEE Trans.*

Microw. Theory Tech., 2019.

[155] C. Hu, R. Khanna, J. Nejedlo, K. Hu, H. Liu, and P. Y. Chiang, “A 90 nm-CMOS, 500 Mbps, 35 GHz fully-integrated IR-UWB transceiver with multipath equalization using pulse injection-locking for receiver phase synchronization,” in *IEEE Journal of Solid-State Circuits*, 2011.